Journal of Alloys and Compounds 953 (2023) 170133

Contents lists available at ScienceDirect

Journal of Alloys and Compounds

journal homepage: www.elsevier.com/locate/jalcom

In situ diffraction studies of phase-structural transformations in hydrogen and energy storage materials: An overview

Volodymyr A. Yartys [a,*], Colin J. Webb [b], Fermin Cuevas [c]

[a] Institute for Energy Technology, P.O. Box 40, Kjeller NO 2027, Norway
[b] Queensland Micro and Nanotechnology Centre, Griffith University, Nathan 4111, QLD, Australia
[c] Univ Paris-East Creteil, CNRS, ICMPE (UMR 7182), 2 rue Henri Dunant, Thiais F-94320, France

ARTICLE INFO

Article history:
Received 7 March 2023
Received in revised form 30 March 2023
Accepted 13 April 2023
Available online 13 April 2023

Keywords:
Neutron powder diffraction
In situ studies
Hydrogen storage
Metal hydrides
Metal hydrides batteries

ABSTRACT

The paper presents an overview of advanced *in situ* diffraction studies as a highly valuable tool to probe the structure and reacting mechanisms of hydrogen and energy storage materials. These studies offer benefits from the use of a high flux diffraction beam in combination with high resolution measurements, and allow, even when using very small samples, establishing the mechanism of the phase-structural transformations and their kinetics based on a rapid data collection for the various charge-discharge states at variable test conditions. The applied conditions include a broad range of hydrogen/deuterium pressures, from vacuum to high pressures reaching 1000 bar H_2/D_2, and temperatures, from cryocooling (2 K) to as high as 1273 K (1000 °C). Simultaneously, various state-of-charge and discharge are probed when studying metal-H/D systems for hydrogen/deuterium gas storage and as anode electrodes of metal hydride batteries. The range of the studied systems includes but is not limited to the AB_5, AB_2 Laves type, AB, equiatomic ternary ABC intermetallics and Mg-containing layered AB_3 structures and composites. Prospects on Li-ion full cells are considered as well. Interrelations between the structure and hydrogen storage performance, including maximum and reversible H storage capacity, hysteresis of hydrogen absorption and desorption, H_2 absorption and desorption in dynamic equilibrium conditions, are considered and related to the ultimate goal of optimisation of the H storage behaviours of the advanced H storage materials. Numerous contributions of Dr. Michel Latroche to the field are highlighted, particularly in *in situ* studies during electrochemical transformations. The paper summarises a long-standing collaboration of the co-authors in the field, which also included 29 joint topical publications with Dr. Michel Latroche, and references 163 original publications.

1. Introduction

Hydrogen is an energy vector that has a huge impact on a carbon-free energy economy, reducing greenhouse gas emissions as well as dependence on fossil fuel production. Hydrogen can be readily obtained from water using electricity from renewable sources. The energy is regained using a fuel cell to generate electricity (and water), or by the combustion of hydrogen. While further efficiencies may be reached in the production and use of hydrogen, the main stumbling block to large-scale use of hydrogen is storage and transport.

Although commercial hydrogen fuel cell electric vehicles (HFCEV) currently use high pressure (300–700 bar) pressurized gas tanks to store hydrogen on-board, the low density of gaseous hydrogen at ambient conditions and the requirement to compress the gas resulting in a need for complex and expensive infrastructure remain a challenge. There is a need for alternative hydrogen storage systems that can reach high hydrogen densities at an affordable cost. An avenue that has been extensively studied is the use of various types of solid-state materials that are capable of reversibly storing hydrogen and providing it as a fuel to the fuel cell [1].

From a practical point of view, the time and ease of loading the material with hydrogen, the amount of hydrogen that can be usefully stored, the rate at which it can be retrieved, and the temperature and pressure conditions involved are critical requirements for determining the potential of a material. These practical use requirements are defined by the kinetics of hydrogen absorption and desorption, the thermodynamics of metal-hydrogen interactions (enthalpy of sorption/desorption), the diffusion of hydrogen through the material, the chemical bonding of hydrogen related to its location in the material's structure, chemical environment, and metal-

* Corresponding author.
E-mail address: volodymyr.yartys@ife.no (V.A. Yartys).

https://doi.org/10.1016/j.jallcom.2023.170133

hydrogen distances in the material as well as by material properties affecting its H storage performance.

In order to study these material properties and the features of the metal-hydrogen interactions, various techniques can be utilized [2], including gas absorption and desorption measurements to determine the H storage capacity, thermodynamics and kinetics, scanning and tunnelling electron microscopy to assess the particle sizes and elemental composition, Raman and infrared spectroscopy to investigate the chemical bonds, vibration modes and gas-solid interfaces, and neutron and X-ray scattering techniques that enable exploration of the material structure and the location and movement of hydrogen within that structure. For detailed examination of the physics and chemistry of the absorbed hydrogen interaction with the solid, neutron scattering is particularly well-suited as the neutrons penetrate the material and the hydrogen atoms when used as deuterium isotope have a large coherent neutron scattering length enabling their location in the crystal structures together with metal atoms [3].

Three main methods of neutron scattering are exploited to investigate the hydrogen-solid interactions and interface: neutron powder diffraction (NPD), inelastic neutron scattering (INS) and quasielastic neutron scattering (QENS) [4,5].

In NPD techniques, the neutrons are elastically scattered off the nuclei of the hydrogen and material atoms. For crystalline materials, the pattern of coherently scattered neutrons displays Bragg peaks which intensities depend on the types and positions of atoms in the crystal lattice, while incoherently scattered neutrons form a background in the powder diffraction pattern. Hydrogen has a large incoherent cross section, but in contrast its isotope deuterium has a large coherent cross section and a much smaller incoherent cross section. For this reason, most NPD studies are performed with deuterium wholly or partially substituted for hydrogen.

INS involves detecting the neutrons inelastically scattered while passing through the material, either by time-of-flight measurements or by filtering specific energies. INS measurements determine lattice vibrations and rotational transitions in amorphous and crystalline materials. This technique uses the incoherently scattered neutrons and can be employed for both hydrogen and deuterium.

QENS also uses the incoherent neutron scattering cross section but monitors energy changes in the inelastically scattered neutrons enabling the study of the hydrogen diffusion dynamics in the material.

While neutron scattering experiments are routinely performed successfully on ex situ samples, *in situ* studies have the advantages of examining the sample at variable testing conditions, when the temperature, gas pressure and hydrogen capacity are changed [6,7]. This enables the material to be studied while undergoing hydrogen ab- or desorption to investigate structural and chemical changes in the hydrogen-material composite to determine intermediate reaction products, phase transformations and reaction rates.

X-ray diffraction (XRD) can also be employed to study material structure [8,9], however, as the intensity of elastically scattered photons is proportional to the electron density, hydrogen is difficult to directly observe. XRD synchrotron facilities have the advantage of high photon flux compared to neutron sources, which enables the use of small sample sizes, for example milligrams, and rapid data collection times of a few seconds, depending on the sample and the instrument's beam energy and flux. In comparison, NPD requires sample of the order of grams, and collections times that are normally longer.

Previous reviews of the use of neutron diffraction for characterisation of potential hydrogen storage materials have covered the techniques as well as applications of neutron scattering. Klein et al. [4] discuss in detail the theory and practice of the different neutron scattering techniques introduced above. In addition, a number of types of solid-state hydrogen storage materials are described, including metal hydrides, complex hydrides and porous materials, and the application of the scattering techniques to these categories.

The use of inelastic neutron scattering applied to high-pressure hydrides was also reviewed [10], focussing on INS studies of high-pressure monohydrides of d-metals of the VI–VIII groups and concluding that INS was effective at determining the H-H distances and therefore which materials do not obey the Switendick criterion, which postulates a minimum H-H distance of hydrogen atoms in the metal lattice of 2 Å.

Other neutron techniques have also been reviewed, including the use of SANS to investigate polymers, hydrogel, and bio-materials [11], neutron radiography and tomography to study the distribution of hydrogen in a storage bed [12], a comparison of neutron radiography to carrier gas hot extraction for the study of hydrogen mass transport in iron [13], neutron reflectivity to examine hydrogen concentration in multi-layer Fe-Nb thin films and a combination of *in situ* neutron radiography and IR-thermography to determine the driving forces for hydrogenation of sodium alanate [14].

An overview of the early works on the structural chemistry of intermetallic hydrides was presented in [15]. In a recent comprehensive review of AB_2 Laves type intermetallic compounds for use as storage materials, Yartys et al. [16], detailed many classes of Laves phase intermetallics and their structures as determined by neutron diffraction. Bououdina et al. [17] have also discussed Zr-based AB_2 Laves phase materials as part of a review of hydrogen storage materials. A review of the achievements of the European Cooperation in Science and Technology (COST) Action MP1103 [18] included use of *in situ* neutron diffraction for characterisation of nanostructured materials for solid-state hydrogen storage as well as neutron radiography to quantify hydrogen absorption by metal storage tanks. Reviews of more specific materials and the use of *in situ* neutron diffraction include those of lithium borohydride [19], magnesium borohydride [20], light metals [21] and porous materials [22].

In this article, the available neutron facilities are described and compared and the types of sample cells and sample environments necessary for *in situ* neutron studies are explored. In addition, a range of *in situ* neutron experiments yielding important results for hydrogen gas and electrochemical loading in a variety of potential materials for hydrogen storage applications is described. Among them, this manuscript contains 45 citations of the research articles by Dr. Michel Latroche, highlighting a great impact of his contribution to the field of hydrogen and energy storage materials, in particular when applying operando electrochemical studies related to the rechargeable batteries R&D.

2. Available neutron sources and their comparison

There is a large number of neutron facilities around the world. These can be divided into spallation sources and reactor sources, based on how the neutrons are generated. In a spallation source, a proton beam is accelerated into a heavy metal target, such as tantalum, tungsten, lead or mercury. Neutrons are ejected from the target metal atoms and slowed by moderators to provide a variety of energies to the instruments. In contrast to those produced in a nuclear fission reactor, the spallation source neutron beams can be pulsed by modulating the incident proton beam. While spallation sources have higher flux than reactor sources and use less energy, they are more expensive, and the targets require regular replacement. The main large neutron facilities currently in operation are listed below.

ISIS-Rutherford-Appleton Laboratories, United Kingdom has two spallation sources and generates a pulsed 800 MeV proton beam which passes through a carbon target (to produce muons) and then strikes a tantalum neutron target. Water, liquid methane and liquid hydrogen are used as moderators to slow the neutrons. Over 30 instruments use the neutrons generated, providing facilities for high

resolution powder diffraction, inelastic and quasielastic neutron spectroscopy as well as other techniques.

Institut Laue-Langevin, Grenoble, France uses a high-flux 58.3 MW nuclear reactor to provide a continuous total neutron flux of 1.5×10^{15} neutrons per second per cm^2. The neutrons are moderated by the heavy water used to cool the reactor as well as liquid deuterium. There are a total of 47 instruments, including 6 for powder diffraction, 6 for single crystal diffraction and another 6 for 3-axis spectrometry. The most suitable for the *in situ* NPD studies is a medium/high resolution two-axis diffractometer D20, which is capable of producing a neutron flux of 10^8 s^{-1} cm^{-2}. D20 shows the fastest counting rate of any reactor-based neutron diffractometer and offers $\Delta d/d \sim 2 \times 10^{-3}$. Advanced electronics together with a variety of sample environments allows *in situ* time-resolved experiments at the timescale of a few tens of milliseconds [23]. Furthermore, at ILL, the D1B diffraction line has been widely used for real-time diffraction experiments as will be recognized several times in this review. Although the neutron flux at D1B ($7 *10^6$ n $cm^{-2}s^{-1}$) is lower than that for the D20 instrument, high-quality diffraction patterns can be collected every 10 min thanks to a position-sensitive detector (PSD).

The NIST Center for Neutron Research (NCNR) reactor in Maryland, USA produces cold neutrons servicing 22 instruments for neutron scattering research. These instruments include small angle scattering (SANS) instruments, ultra-small (USANS) and very small angle scattering (VSANS), a high-resolution powder diffractometer and residual stress diffractometer as well as triple and multi-axis spectrometers.

Oak Ridge Neutron Facilities (SNS/HFIR) in Tennessee, USA, encompasses both reactor and spallation sources. The High Flux Isotope Reactor (HFIR) produces cold and thermal neutrons for research as well as isotope production and studies on gamma irradiation. The reactor supports 13 instruments for research including a neutron powder diffractometer, small angle, wide angle, magnetic and stress diffractometers as well as neutron imaging and spectrometers.

Housed in the same facility is the spallation neutron source (SNS). Negatively charged hydrogen ions are initially linearly accelerated before the electrons are stripped off and the resulting proton beam impacts a mercury spallation target. Pulsed at 60 Hz, the resulting neutrons are slowed by a moderator before use at 20 instruments, including powder and single crystal diffractometers, USANS and spectrometers.

Three powder diffractometers, General-Purpose Powder Diffractometer (POWGEN; SNS, ORNL), High-Resolution Powder Diffractometer (BT-1; NIST), and Neutron Powder Diffractometer (POWDER, HB-2A; HFIR, ORNL) are generally characterized by a narrow instrumental resolution over a large *Q*-range. These instruments are flux-limited, leading to data collection times of hours. However, when a fast data collection is targeted, instruments have been designed in a way that either the *Q*-range can be reduced, or the instrument resolution can be coarsened, increasing the flux on the sample by several orders of magnitude. When coupled with a large 2-dimensional detector, it is possible to record diffraction patterns in the sub-second regime, allowing for kinetic processes to be monitored. This provides alternatives to D20 in fast collection of the diffraction data.

The Los Alamos Neutron Science Center (LANSCE) is another spallation facility in New Mexico, USA. The Lujan center provides for scientific research producing cold and ultra-cold neutrons by cooling the neutrons produced in a tungsten target with water or solid deuterium moderators [24]. Instruments include diffractometers for stress and strain of polycrystalline materials and time-resolved studies, as well as neutron imaging/tomography and SANS.

The Swiss Spallation Neutron Source (SINQ) is a continuous spallation facility in the Paul Scherrer Institut (PSI), Switzerland. Neutrons emitted from the interaction of a proton beam with a lead spallation target are cooled using a liquid deuterium moderator. 5 diffraction instruments use either thermal or cold neutrons for diffraction studies, with another two SANS instruments as well as reflectometers and spectrometers. The High Resolution Powder Diffractometer HRPT allows a data set collection which can be successfully processed by Rietveld refinements in just 3 min, and this has been utilised during the studies of several metal hydride materials described in this review.

FRM-II is a research reactor-based neutron facility in Munich, Germany. 25 scientific instruments as well as irradiation facilities use neutrons from the reactor and cooled through a liquid deuterium moderator. There are 11 instruments for structure and stress studies as well as SANS instruments and imaging and spectroscopy instruments.

The Institute for Solid State Physics, Tokyo University, Japan (ISSP) Neutron Scattering Laboratory in Tokai, is a reactor driven neutron facility with high resolution powder diffraction, single crystal diffraction, SANS, VSANS and USANS instruments. Imaging and spectrometry capabilities are also available.

J-PARC (Japan Proton Accelerator Research Complex) is a proton accelerator facility in Tōkai, Japan. Three accelerators support facilities dedicated to materials and life sciences as well as particle physics and nuclear transmutation. A 3 GeV Rapid Cycling Synchrotron provides a pulsed proton beam to a mercury spallation target with liquid hydrogen moderators to provide neutrons and muons for the Materials and Life Science Experimental Facility (MLF). Instruments using elastic neutron scattering in MLF include single crystal diffraction, powder diffraction, small-angle and total scattering, and reflectivity instruments, while for inelastic scattering there are instruments for time-of-flight and spin echo spectrometry, as well as imaging and elemental analysis. The Super High Resolution Powder Diffractometer accommodated at the Materials and Life Science Experimental Facility has achieved a high resolution of $\Delta d/d = 0.0365\%$ and allows access to an expanded *Q*-range during the data collection [25,26].

The Australian Centre for Neutron Scattering in Lucas Heights, Australia uses the OPAL (Open Pool Australian Lightwater) reactor to generate neutrons for use in 15 instruments, including two powder diffraction instruments (high resolution and high intensity) as well as strain, SANS, USANS, reflectometry and spectrometry instruments.

3. Experimental cells

In situ neutron scattering experiments investigating the interaction of hydrogen with a material demand a sample cell capable of maintaining the experiment conditions, such as pressure and temperature as well as interfering as little as possible with the passage of the neutron beam. In addition, the cell must be constructed of suitable material as hydrogen diffuses through many metals at higher temperatures and embrittles some metals, making the cell susceptible to catastrophic failure [27,28]. Hydrogen embrittlement is apparent in iron and most iron-based alloys such as martensitic steels [29], due to hydrogen diffusion along grain boundaries and concentration in crack tips [30]. Hydrogen also reacts to form hydrides with metals such as zirconium, tantalum, vanadium and palladium, which have much lower yield strengths and therefore are unable to withstand higher pressures of hydrogen gas. Thus, the walls of the sample cells aiming for a decreased contribution of the cell to the diffraction pattern should eliminate a direct contact with hydrogen gas if the mentioned metals are utilized. As many stainless steels such as 316 L allow only a negligible hydrogen diffusion at moderate temperatures (< 350 °C) and pressures (< 100 bar), such type of steel is most frequently used as a material of choice to build the samples cells.

Because the diffusion of hydrogen through a SS 316 L metal cell wall becomes significant over 470 °C, it is possible to hydrogenate/dehydrogenate sample material enclosed in a crimped iron envelope without exposing the sample to oxygen [31]. However, generally diffision invalidates the experiment because the quantity of hydrogen in the cell becomes no longer known, particularly with increasing H_2 pressures, and thus a special H-impermeable material selection should be made to eliminate this problem. Furthermore, hydrogen embrittlement should be properly addressed when making the material selection to safely build the sample cells and to eliminate any possibility of a catastrophic failure of the equipment during the H_2 loading tests.

The material of the cell wall is also exposed to the neutron radiation, which can add an unwanted signal to the scattered neutron data. While this can sometimes be filtered out of the data, it often complicates the data analysis or obscures sample data. Metals with very low coherent scattering cross sections, such as vanadium, contribute very little to the signal from the sample container (this metal however reacts with hydrogen and therefore should not be exposed to it). Null-matrix alloys made from two metals with coherent scattering lengths of opposite sign, such as titanium (−3.438 fm) and zirconium (7.16 fm), also contribute negligibly to the signal. In addition, many materials become radioactive after exposure to the neutron beam, for example, in stainless steel after several days of thermal neutron bombardment, isotopes of cobalt require long on-shelf storage for the radioactivity to reduce to a safe level.

The pressure and temperature conditions of the experimental work, as well as possible reactions with the sample, place limitations on the materials available for cell construction. For example, while aluminium does not embrittle or allows hydrogen to diffuse through, it is only suitable for low pressure experiments due to the moderate yield strength. Stainless steels are only slightly permeable to hydrogen at 200 °C, so they be used at up to 350 °C depending on the wall thickness, but H_2 diffusion is quite strong at the temperatures exceeding 500 °C. Vanadium cans, which are extensively used as sample holders at neutron facilities due to transparency to neutrons across a wide temperature range, cannot be used together with hydrogen due to their embrittlement. $Ti_{68}Zr_{32}$ is a strong null-matrix alloy but also embrittles after exposure to hydrogen. Techniques such as plating the inside of the sample cell with a material impervious to hydrogen, or using a sleeve of appropriate material, may be used to overcome these problems. The following cells have been developed for specific sets of experimental conditions for *in situ* experiments with hydrogen.

3.1. Stainless steel cell to 100 bar

A stainless steel cell has been used successfully to 100 bar of hydrogen at moderate temperatures for *in situ* studies on potential hydrogen storage materials at ISIS and SINQ [32,33]. Manufactured from 316 L stainless steel, with an internal diameter of 10 mm, and a wall thickness of 0.75 mm, this cell was used at ISIS for studies on palladium as well as $LaNi_5$ [6], with and without a collimator. Fig. 1 shows the geometries required to use a collimator of a neutron absorbing material such as BN in order to restrict both the input beam and the detected neutrons to the centre of the sample, excluding as much as possible of the sample cell.

A similar cell (outer diameter 9.5 mm, inner diameter 7.8 mm) made of stainless steel was designed J.-M. Joubert [34] and used at ILL for deuterium pressures up to 100 bar and 300 °C [35–37].

IFE has been using SS 316 L cylindrical autoclaves (limiting H_2/D_2 pressure to 50 bar) with external diameter 6 mm and ¼" with decreased thickness of the wall at the sample location, allowing them to fit into the standard fitting to the cryostat and the heating resistance furnace at HRTP, SINQ, PSI.

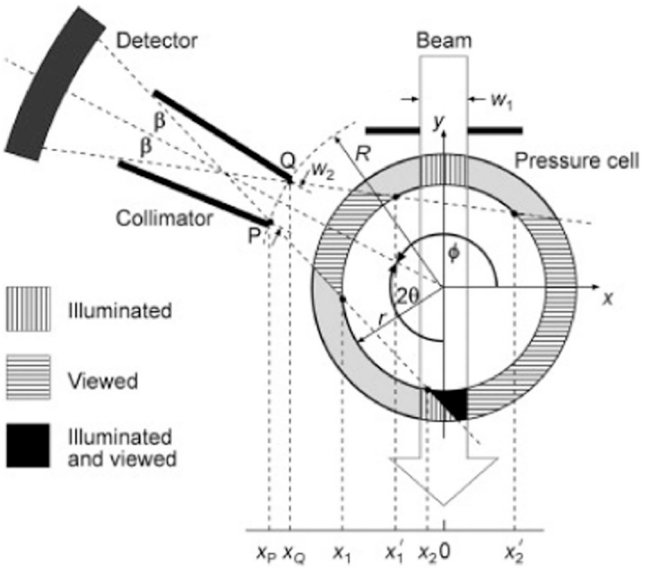

Fig. 1. Schematic of a collimated steel sample cell.
(Reprinted with permission from [6]. Copyright (2012) Elsevier).

3.2. Zero matrix HP cell

A high pressure sample cell manufactured from $Ti_{68}Zr_{32}$ has been used for *in situ* experiments at SINQ [38] and ILL [39,40]. The zero matrix alloy does not scatter neutrons coherently and does not contribute significantly to the diffraction data pattern. Because TiZr embrittles, a thin (0.1 mm) stainless steel sleeve was fitted inside the TiZr to prevent hydrogen from interacting with the cell body. Although the steel contributes to a signal, this has a small effect because of the low thickness, with the sufficient tensile strength of the TiZr allowing to contain the hydrogen pressure. Up to 1000 bar D_2 has been applied at SINQ [38] and ILL [39,40].(Fig. 2).

It is worth remarking that a zero matrix TiZr cell has been successfully implemented for the study of electrochemical reactions in Li-ion batteries [41].

3.3. Aluminium cell used on Engine-X

An aluminium cell with an ID of 18 mm and a wall thickness of 1 mm (Fig. 3) was constructed to perform a spatial analysis of the hydrogen adsorption by $LaNi_5$. For this experiment, use of Al cell allowed a good thermal management as the heat of reaction was rapidly distributed through the water-cooled copper plates at each end of the cell. Engine-X, a stress/strain instrument at ISIS, was used to investigate spatial inhomogeneities in the uptake of deuterium following a rapid absorption step [42].

3.4. Sapphire cell

As a single crystal, sapphire has a high yield strength making it suitable for high pressure work. Sapphire is frequently used in X-ray diffraction *in situ* studies [8,43] as it is relatively easy to mask the peaks in the scattering patterns caused by the sapphire, when its single crystal is used. Ikeda, Ohshita, Otomo, Sakaki, Kim, Nakamura, Machida and Von Dreele [44] have used a commercial single crystal sapphire container (Fig. 4a) with a 5.8 mm ID, 2.5 mm wall thickness and a 5.0 mm base thickness for *in situ* neutron diffraction measurements on $LaNi_{4.5}Al_{0.5}$ with the total scattering instrument, NOVA at JPARC in Japan.

Results were compared with an *ex situ* sample in a vanadium can, shown in Fig. 4b.

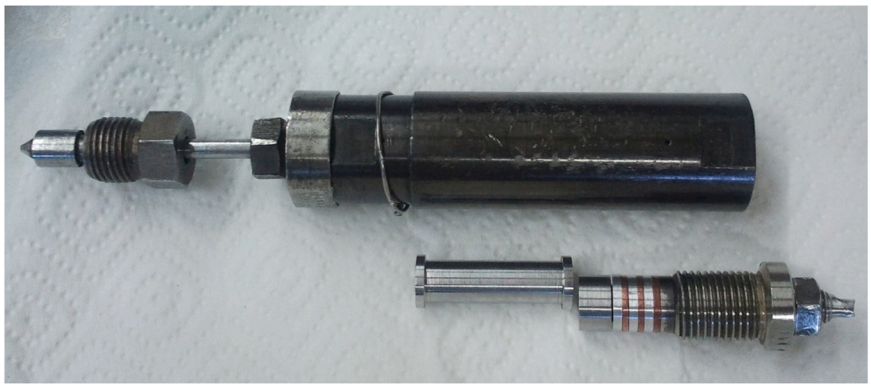

Fig. 2. Zero matrix high pressure TiZr cell with thin stainless steel liner.

3.5. Electrochemical cell

The electrochemical three-electrode cell developed at CNRS, France, for the study of electrode materials in Ni-MH batteries is shown in Fig. 5 [45]. It is based on an the developed earlier by Chabre et al. cell for the study at ILL of proton insertion in γ-MnO_2 [46,47]. The body of the cell is made of amorphous silica leading to a wavy diffraction background. For the study of metal hydride materials, the working electrode is a composite electrode made from intermetallic powder (< 100 μm) as active material mixed with carbon black and PTFE. The mixture is mechanically compressed over a nickel grid and rolled up on itself to form a cylinder of about 5 cm height and 10 mm diameter (Ø). This working electrode is then sandwiched between inner (Ø 8 mm) and outer (Ø 12 mm) counter-

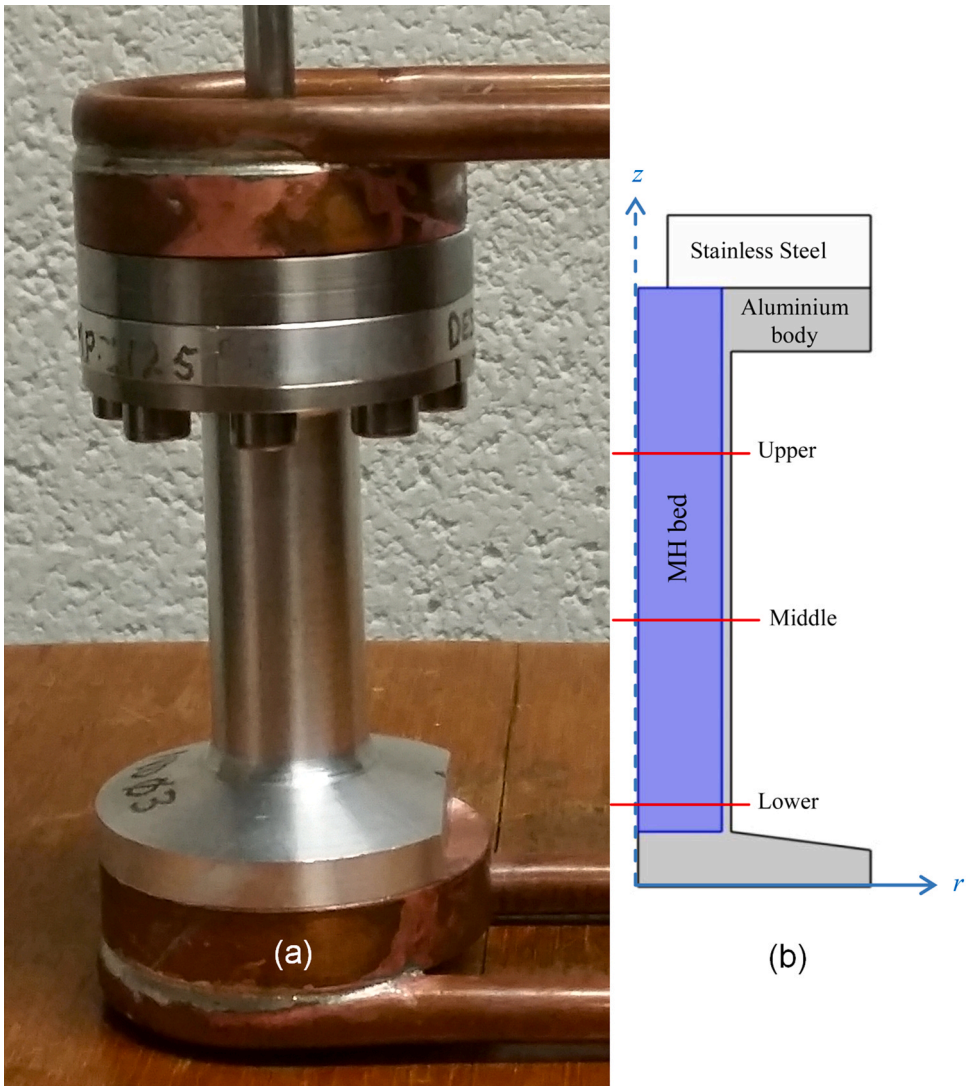

Fig. 3. Aluminium *in situ* cell employed at HRPD, ISIS for analysis of spatial inhomogeneities in deuterium absorption. (a) Layout; (b) Scheme. (b) reprinted with permission from [42]. (Copyright (2016) Elsevier).

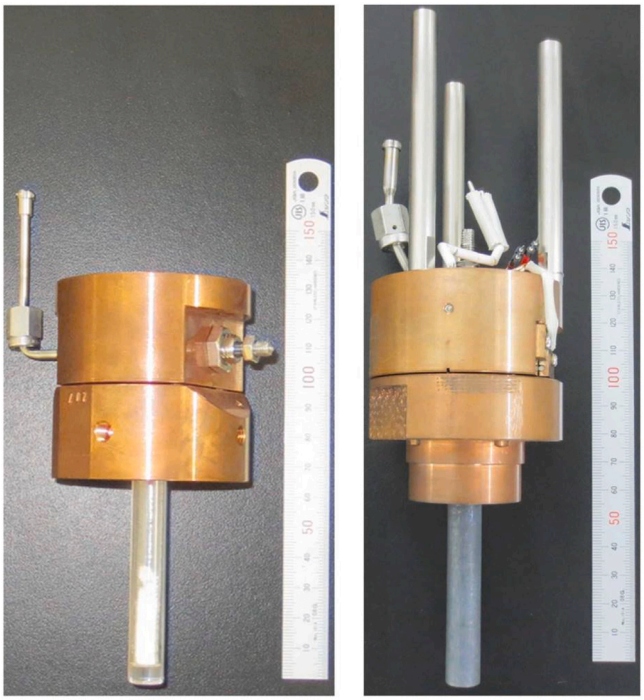

Fig. 4. Sapphire (a) and vanadium (b) *in situ* cells [44].

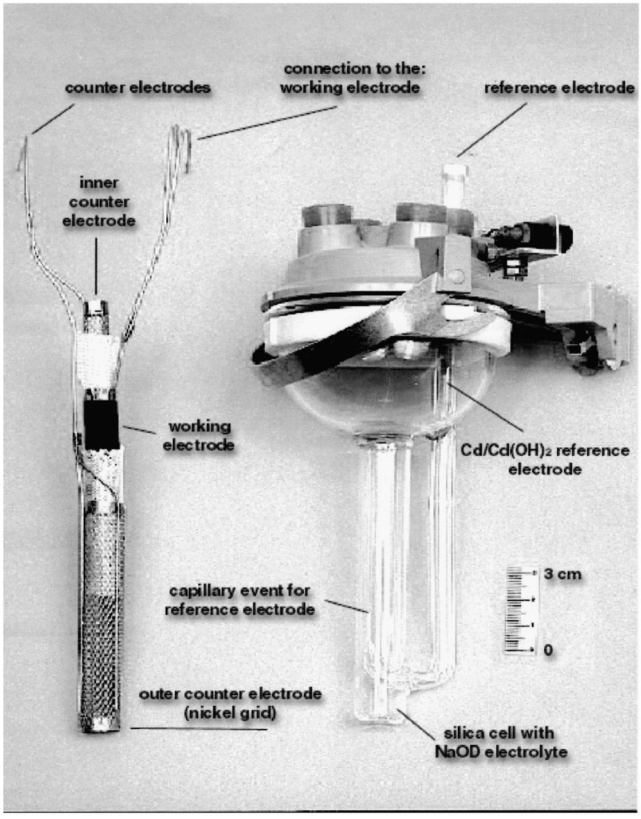

Fig. 5. View of the various parts of the *in situ* neutron diffraction electrochemical cell assembly.
Reprinted with permission from [45]. (Copyright (2002) Elsevier).

electrode cylinders made of nickel grid, with silica sheaths as separators on each side of the working electrode. The electrochemical couple $Cd/Cd(OH)_2$ is used as reference electrode. It is located in a side tube entering the main tube with a capillary going against the bottom side of the working electrode. The three electrodes are immersed in deuterated alkaline electrolyte (KOD [45,48] or NaOD [49] in D_2O) to take advantage of the high coherent scattering section of deuterium. This cell has been widely used for *in situ* structural studies of both negative [45, 50–52] and positive [53] electrode materials for Ni-MH batteries. Its geometry is very close to that of commercial-type batteries and well-adapted to the Debye-Scherrer powder neutron diffraction beamlines. Recently, a coin-type cell has also been developed at the ISIS facility [54].

3.6. Coupling to ancillary equipment

During *in situ* neutron diffraction studies, the diffraction data is monitored as a function of different variables such as deuterium pressure, temperature or electrochemical potential. Changes in these variables modify the deuterium content and phase composition in the alloy. The refinement by the Rietveld method of deuterium site occupancies and phase amounts allows to determine the overall deuterium content in the sample during the experiment. However, these results require confirmation by complementary techniques to check and reinforce the validity of structural models. Thus, to control and measure the overall deuterium content in the alloys, the neutron diffraction cells are connected to different ancillary equipment such as Sieverts' apparatuses, pressure gauges or galvanostats. Moreover, most of these devices not only monitor changes on deuterium content but also control the time-evolution of variables during the experiments. Most popular devices are now described.

a) Manometric Sieverts' apparatus for Pressure-Composition-Temperature (PCT) measurements

Manometric Sieverts' apparatuses consist of calibrated cell volumes equipped with pressure transducers and valves for connection to different lines: deuterium inlet, deuterium venting and vacuum line. Fig. 6 shows a manual custom Sieverts' apparatus developed at CNRS and used in many experimental *in situ* diffraction studies [35–37,55,56]. It works at room temperature and deuterium

Fig. 6. Manual homemade Sieverts' apparatus developed at CNRS for *in situ* neutron diffraction studies. At the top: inlets for $H_2(D_2)$, vacuum ("Vide") and venting ("atm"). They are connected through copper capillaries and yellow, green and green valves, respectively, to the main body of the apparatus. Two pressure gauges (1 and 100 bar) are located at the top-right. The three black valves connect the sample colder (PE outlet) to two large reservoirs (R1 and R2).

pressure between 100 Pa and 10 MPa. A long thin copper capillary tube connects the sample holder, placed in the beam, to the Sieverts' apparatus, where the user is located several meters away from the beam to avoid radioactive exposure. Using this system, deuterium uptake by the sample is measured by first determining by manometry the number of moles of deuterium in a closed calibrating volume, allowing the gas to expand towards the sample and, after completion of the solid-gas reaction, measuring again by manometry the amount of residual gas in the whole system. The difference between initial and final amount of deuterium corresponds to the sample deuterium uptake. The measurement is done by stepwise increasing (absorption) and decreasing (desorption) the pressure to register Pressure-Composition-Isotherms at constant temperature. Accurate measurements can be made when the appropriate care and methods are employed [57] and the real gas equations are used at higher pressures (> 1 MPa) [58].

a) Vacuum system and pressure gauges for Thermal Desorption (TD) measurements

Simultaneous measurement of neutron diffraction and thermal desorption data has been widely reported [36,56,59,60]. Both signals are synchronized in time and temperature which are corelated through a linear heating ramp. With a typical heating rate of 0.5 K/min and acquisition time of 5 min per diffractogram, the temperature resolution of diffraction patterns is 2.5 K [60]. Stainless steel or silica sample holders have been used. The choice is mainly based on the preference for diffraction patterns to present either additional Fe-lines [36] (Fig. 7) or a wavy background [61], respectively.

To monitor deuterium desorption, the sample holder is connected to a vacuum line equipped with a pump and a pressure sensor. A rotatory pump is often used (residual pressure, $P_{res} \sim 1$ Pa) since it easily evacuates the high amount of deuterium stored in large neutron samples (mass from 5 to 10 g) and ensures a constant pumping speed in the operational pressure range (typically between 1 and 1000 Pa). Assuming fast pumping rates and small sample-holder volume, the deuterium desorption rate (dx/dt) from the sample is proportional to the released deuterium pressure [62]:

$$-\frac{dx(t)}{dt} = \frac{S}{RT}P(t)_{H_2} \sim AP(t)_{H_2} \quad (1)$$

where x is the number of deuterium atoms per alloy formula unit, S is the pumping speed, R the gas constant, T the temperature of the vacuum line and P_{H2} the gas pressure. In absence of a quadrupole mass spectrometer, the released gas is assumed to only consist of deuterium. The deuterium pressure is measured by a Pirani [60] or a capacitance manometer [36]. If the pumping speed S is constant during the whole desorption process, the monitored pressure scales to the deuterium desorption rate by the proportionality factor A:

$$A = \frac{x_{t=0}}{\int P dt} \quad (2)$$

where $x_{t=0}$ is the initial deuterium content in the sample, *i.e.* before starting the thermal desorption. In the end, as shown in Fig. 7, the deuterium desorption is synchronized with the neutron diffraction patterns (a) and the phase amounts, determined from Rietveld refinements, are correlated to the deuterium desorption signal (b).

a) Galvanostat device for electrochemical cycling

Coupling between electrochemical data and neutron acquisition is facilitated by the fact that both methods can be computer-monitored and their base time can be easily synchronized. Often, the electrochemical process is in galvanostatic mode and driven with a microprocessor-controlled galvanostat [45,49,51,63]. Typically, an applied charge current is imposed for a time exceeding the expected electrode capacity to take into account the competing Hydrogen Evolution Reaction (HER) through Heyrovsky or Tafel mechanisms [64]. On discharge, a constant current is applied until a given threshold potential is reached, typically 0.5 V against $Cd/Cd(OH)_2$ reference electrode. Then, to avoid electrode oxidation, the current is automatically switched-off and the electrode enters relaxation. Since one electron is provided by each hydrogen atom released from the electrode to the solution, the coulombic discharge, Q_{dis}, relates to the released hydrogen amount as:

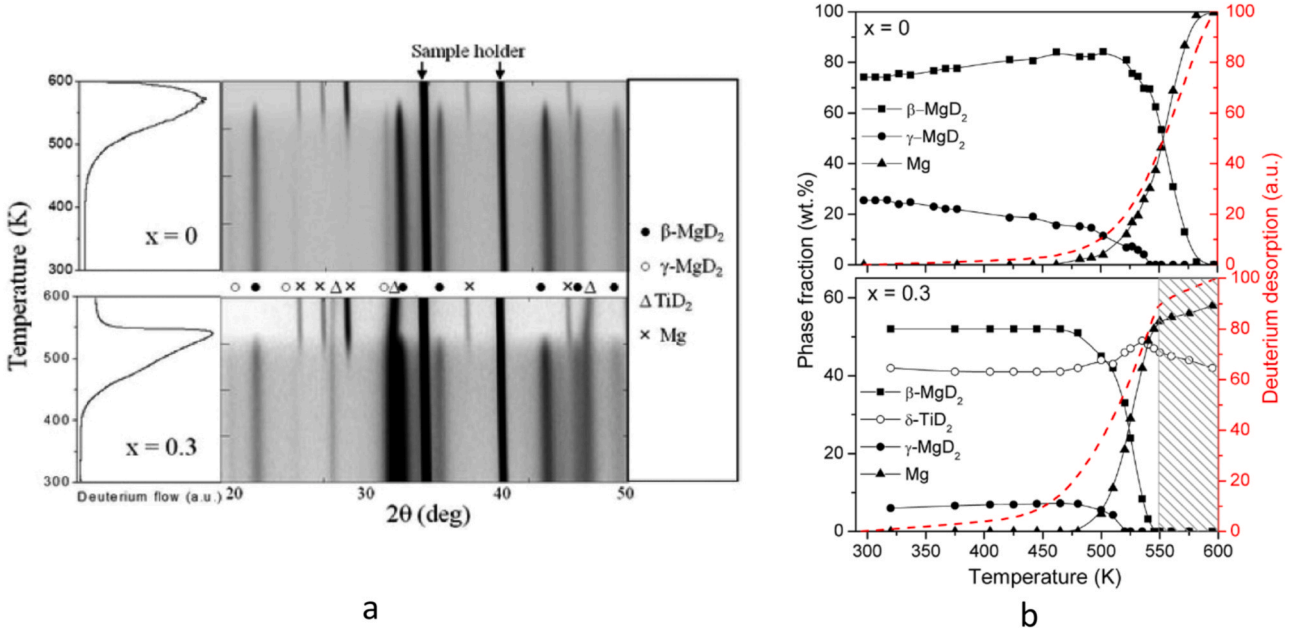

Fig. 7. (a) Simultaneous acquisition of neutron-diffraction (ND) patterns and thermal desorption (TD) spectra of $(1-x)MgD_2 - xTiD_2$ nanocomposites for $x = 0$ and 0.3 samples. Heating rate 0.5 K/min. (b) TD spectra and 2D evolution of ND patterns as a function of temperature. Evolution of the refined phase amounts with temperature. Reprinted with permission from [36]. (Copyright (2013) American Chemical Society).

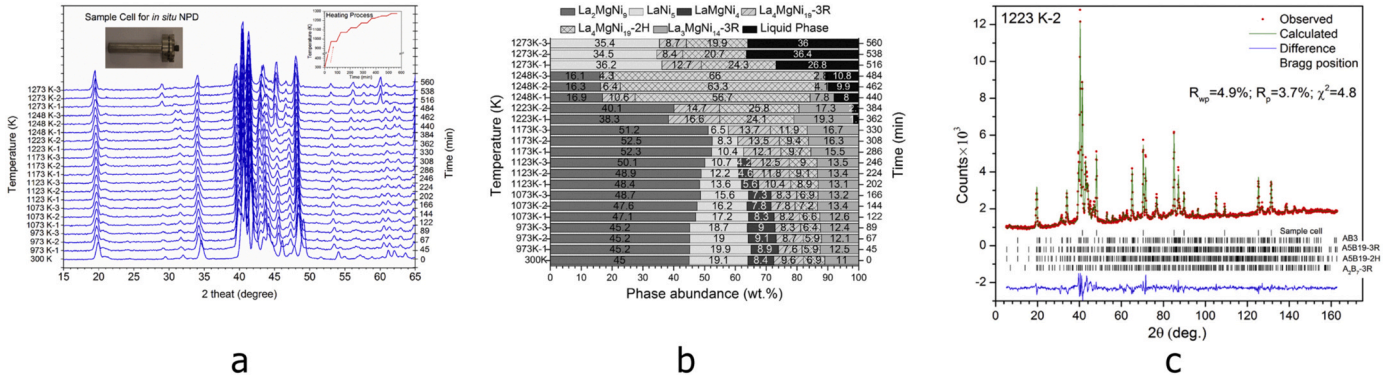

Fig. 8. (a) Evolution of the *in situ* NPD pattern of La_2MgNi_9 compounds during heating (K-1, K-2 and K-3 represent sequence of hold times; 0–22 min; 22–44 min; and 44–66 min, respectively). Inset: SS sample cell used to accommodate the alloy. Inset: temperature profile during the annealing.(b) Phase abundances as a function of temperature and heating time during the annealing of the as-cast La_2MgNi_9 alloy from Rietveld refinements of the NPD data.(c) *In situ* powder neutron diffraction pattern of as-cast sample collected at 1223 K. Vertical bars show positions of the Bragg peaks for the phase constituents (from top to bottom): Fe (sample cell), AB_3, A_5B_{19}-3R, A_5B_{19}-2 H and A_2B_7-3R phases. (Reprinted with permission from [65]. Copyright (2016) Elsevier).

$$\Delta x = Q_{dis}/nF \quad (3)$$

where Δx is the number of hydrogen atoms released by alloy formula unit, F is the faraday constant (26.8 Ah mol^{-1}) and n the number of alloy mols. Thus, the amount of electrochemical released deuterium can be compared with the evolution of deuterium content in the electrode as determined by refinement of neutron diffraction data.

4. Temperature dependent transformations

4.1. Phase-structural transformations in the metal hydride anode

4.1.1. La-Mg-Ni alloys on their annealing between 300 K and 1273 K [65]

Studies of the temperature-induced phase-structural transformations in the as-cast La_2MgNi_9 metal hydride battery electrode alloy were performed by *in situ* neutron powder diffraction at HRPT, SINQ/PSI at temperatures ranging from 300 K to 1273 K. Initial alloy is multi-phase structured, containing six different intermetallics with five stoichiometric compositions. These include the targeted rhombohedral La_2MgNi_9 as the main phase constituent, together with three electrochemically active intermetallics, La_3MgNi_{14} (3 R), La_4MgNi_{19} (2 H) and La_4MgNi_{19} (3 R). Furthermore, the alloy contained two "ballast" intermetallics, $LaNi_5$ and $LaMgNi_4$. Various transformations take place on heating, leading to the significant changes in the contents of the constituent intermetallics, first to the disappearance of $LaNi_5$ and $LaMgNi_4$. Thermal volume expansions of the studied intermetallics were well-fitted by the linear dependences and resulted in similar values of 4.3–5.5 vol% at 1223 K as compared to 300 K. The data presenting results of the studies are given in Fig. 8, a, b and c. The temperature-dependent mechanism of transformations is closely related to the content of magnesium in $La_{3-x}Mg_xNi_9$ (x = 1.0, 1.1 and 1.2) alloys [66].

4.2. HDDR process in $MgCo_2$-D_2 system resulting in recombination of $MgCo_2$ and a different mechanism of interaction for MgCoNi alloy [67]

$MgCo_2$ and MgNiCo crystallize with hexagonal Laves type intermetallic structures of the C14 type and do not form hydrides at ambient hydrogen pressures. However, applying high hydrogen pressures in the GPa range forces the hydrogen absorption and leads to the formation of multi-phase compositions, which contain 2.5 at. H/f.u. of $MgCo_2$ or MgNiCo and remain thermally stable under normal conditions. The hydrogenation of $MgCo_2$ resulted in its decomposition to a ternary Mg_2CoD_5 deuteride and metallic cobalt. The interaction of MgNiCo with deuterium under the synthesis conditions of 2.8 GPa and 200 °C proceeded in a more complex way. A very stable ternary deuteride $MgNi_2D_3$ was leached away while Co was separated in the form of Mg_2CoD_5 and the remaining nickel formed a solid solution with Co with the approximate composition $Ni_{0.7}Co_{0.3}$.

The studied transformations can be described by the following equations:

$$MgCo_2 + D_2 \rightarrow \beta\text{-}Mg_2CoD_5\ (38\ wt\%) + \varepsilon\text{-}CoD\ (62\ wt\%) \quad (4)$$

$$MgNiCo + D_2 \rightarrow Mg_2CoD_5\ (40\ wt\%) + MgNi_2D_3\ (6\ wt\%) + Ni_{0.7}Co_{0.3}\ (50\ wt\%) + \varepsilon\text{-}Co\ (4\ wt\%) \quad (5)$$

Time-resolved *in situ* neutron diffraction and Thermal Desorption Spectroscopy were employed to probe temperature-dependent phase-structural transformations in the $MgCo_2$-D system. Some experimental data of the studied of transformations in the $MgCo_2$-D_2 system are shown in Fig. 9, *a, b* and *c*. The following mechanisms of decomposition of the Mg_2CoD_5 deuteride and the formation of Mg-Co compounds in the Co-rich part of the Mg-Co system were proposed and it was concluded that:

(a) The Mg_2CoD_5 deuteride decomposes into elementary Mg and Co at approximately 300 °C.

(b) A polymorphic transformation from the LT tetragonal to the HT cubic modification of Mg_2CoD_5 takes place at around 250 °C.

(c) MgCo and $MgCo_2$ compounds are formed in the Mg-Co matrix by solid-state reactions at 400 and 500 °C, respectively.

(d) A formation of $MgCo_2$ after completion of the deuterium desorption shows that this Mg-Co intermetallic is a new example of the hydrogen storage alloy, for which a complete HDDR cycle was successfully accomplished.

The mechanism of interaction of the alloys with hydrogen becomes significantly affected by the transition metals, Co and Ni. *In situ* neutron powder diffraction of phase-structural transformations accompanying the vacuum desorption of deuterium in the temperature range of 27–500 °C showed a complete recovery of the initial $MgCo_2$ intermetallic *via* a Hydrogenation-Disproportionation-Desorption-Recombination process. $MgCo_2$ is an example of the hydrogen storage alloy, in which a successful HDDR processing results in the reversible formation of the initial intermetallic at much lower temperatures than in the equilibrium phase diagram of the Mg-Co system.

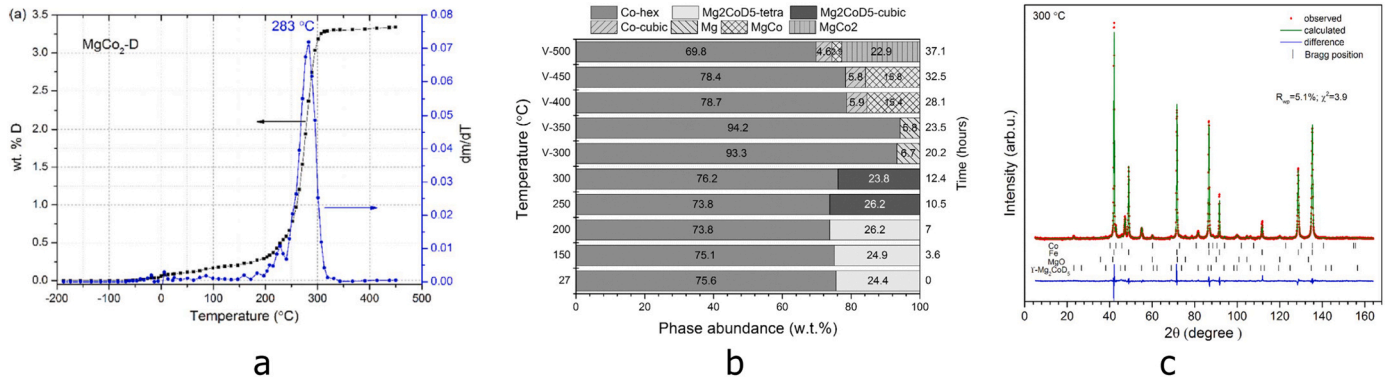

Fig. 9. (a) Thermal Desorption Spectroscopy data showing one event of deuterium vacuum desorption peaking at 283 °C;(b) Temperature-driven evolution of the phase-structural composition of the disproportionated $MgCo_2D_{2.5}$ resulting in a recombination of $MgCo_2$ intermetallic compound;(c) Neutron powder diffraction pattern collected at 300 C and showing a formation of the HT cubic modification of Mg_2CoD_5 deuteride and cobalt. Mg_2CoD_5 decomposes to the metallic Mg and Co in the cause of the desorption process before forming MgCo and, eventually, $MgCo_2$.
Reprinted from an open access article [67] distributed under the Creative Commons Attribution license (http://creativecommons.org/licenses/by/4.0/).

4.3. Low temperature transformations at subzero temperatures

4.3.1. Order-disorder transitions in Laves type $ErMn_2D_2$ hydride

$ErMn_2$ intermetallic compound crystallizes with hexagonal C14 $MgZn_2$ type of crystal structure and orders magnetically with magnetic moments beard by both Er and Mn. $ErMn_2$ forms several individual hydrides with a maximum H storage capacity reaching 4.3 at.H/f.u. and temperature-dependent magnetic properties being sensitive to the hydrogen content, lattice expansion and symmetry and Mn-Mn distances which when exceeding a critical value of 2.7 Å (See Fig. 10 (a)) cause a change of the sign of magnetic interaction between the Er and Mn magnetic moments and a ferromagnetic or antiferromagnetic coupling [68].

$ErMn_2D_2$ deuteride has been studied by high-resolution synchrotron X-ray powder diffraction at temperatures between 150 and 298 K. Below 210 K a transformation from the hexagonal C14 Laves phase type structure (space group $P6_3/mmc$; a = 5.55357(3); c = 9.05368(7) Å; T = 298 K) into the monoclinic one crystallising in the space group $C2/m$ (a = 9.61247(9); b = 5.57558(4); c = 9.07102(8) Å; β = 90.5451(5)∘; T = 150 K) takes place (see Fig. 10(b)) [69].

A rather large two-phase region of coexistence of both structural modifications was observed between 185 and 205 K (Fig. 11, (a) and (b)). Interestingly, formation of the LT monoclinic structure on cooling down is accompanied by a volume expansion.

4.3.2. Equiatomic ternary $ABCH_{1-2}$ hydrides

RTX intermetallic compounds with *R*=Rare Earth Metal; *T* = Transition Metal, Fe, Co, Ni; *X* = Non transition element, Al, Si, Ge, Ga, Sn, In, crystallize with a variety of closely related structure types which can be obtained from the hexagonal AlB_2 type through the ordering of B and C components and *via* internal and external deformation of the structures (see Fig. 12A). When the atoms of transition metal T are substituted by atoms X in an ordered way, this results in the structures of ZrBeSi, LiGaGe and TiNiSi types (see Fig. 12B).

Analysis of the crystal structure of the *RTX* hydride with TiNiSi type structure shows that it contains 4 types of interstitial sites shown in the Fig. 13a, which are suitable for the accommodation of hydrogen atoms. Neutron diffraction study of the dihydride $TbNiSiD_{1.78}$ showed that D atoms completely fill the available Tb_3Ni/R_3T tetrahedra which form a spatial network *via* connecting to each other by vertexes and edges of the tetrahedra (see. Fig. 13b).

Table 1 gives an overview of the crystallographic and magnetic properties of several ternary metal hydrides.

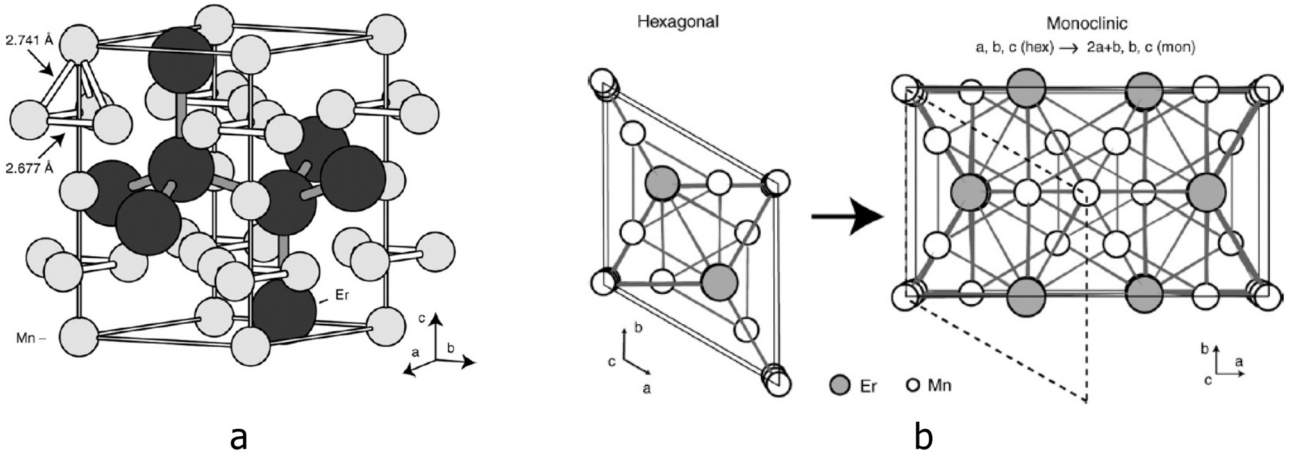

Fig. 10. (a) The metal sublattice in the hexagonal crystal structure of $ErMn_2D_2$ at room temperature. The Mn_4 tetrahedra are slightly elongated along the *c*-axis (Mn–Mn interatomic distances in the (*a*, *b*) plane are 2.677 Å; distances out of the plane, along [001] are 2.741 Å).(b) Scheme of the transformation of the unit cell of the hexagonal phase of $ErMn_2D_2$ existing at room temperature (left) into the monoclinic low temperature structure (right; the original hexagonal cell is shown with the dashed lines). During this transformation, the Er position splits into two positions (Er→Er1 and Er2), and the two Mn positions both split into two (Mn1→Mn1 and Mn2; Mn2→Mn3 and Mn4).
(Reprinted with permission from [69]. Copyright (2006) Elsevier).

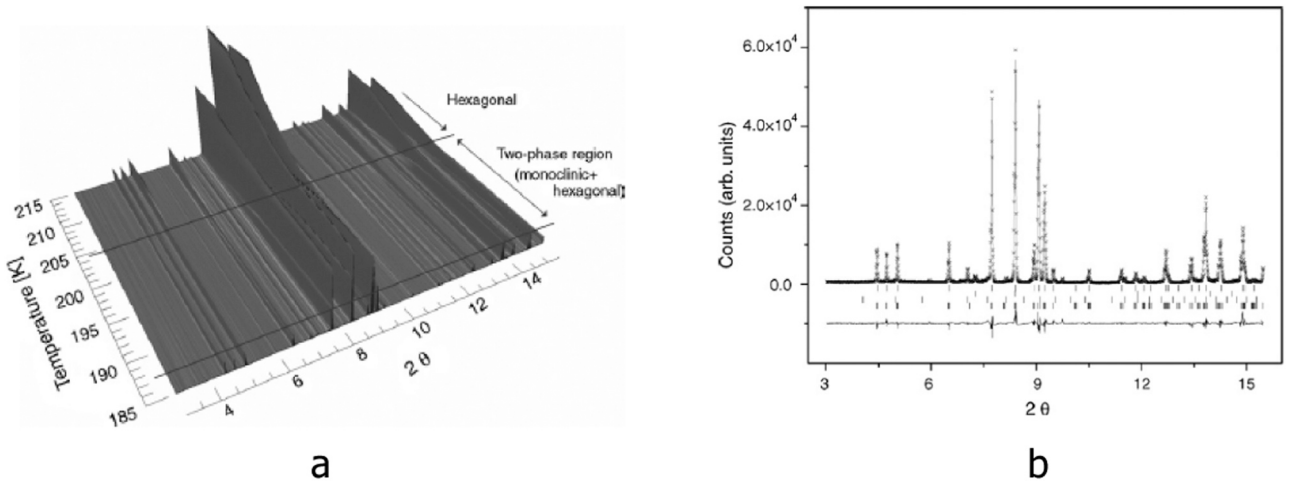

Fig. 11. (a) Evolution of the *in situ* SR-XRD patterns of the $ErMn_2D_2$ as a function of temperature (T = 185–215 K in steps of ΔT = 5 K; λ = 0.3750 Å). (b) Example of the refinements of the diffraction pattern of $ErMn_2D_2$ collected in the two-phase region. This plot shows the data obtained at T = 200 K showing observed (crosses), calculated (upper line) and difference (bottom line) plots. The positions of the Bragg peaks are shown as ticks (from top to bottom: hexagonal $ErMn_2D_2$, $ErD_{2\pm x}$, Er_2O_3, monoclinic $ErMn_2D_2$).
(Reprinted with permission from [69]. Copyright (2006) Elsevier).

The following conclusions can be made concerning influence of hydrogen on the crystallographic and magnetic properties of the intermetallics.

The crystal structures of the intermetallic alloys of the orthorhombic TiNiSi undergo various transformations on the hydrogenation, including a) formation of internally deformed orthorhombic CeNiSnD and TbNiSnD; b) TiNiSi→ZrBeSi type rebuilding of the orthorhombic structure into a hexagonal one; c) TiNiSi→ZrNiAl type rebuilding accompanied by a contraction of the unit cell volume. For the monohydrides CeNiSnD and TbNiSnD volume expansion is small, just 1.5% and 2.8%, which corresponds to a rather small value of 1.0–1.3 $Å^3$/at.D. For TbNiSiD1.78 lattice expansion is much higher, 9.9%, while specific expansion reaches a typic for the metal hydride value 2.8 $Å^3$/at.H close to 3 $Å^3$/at.H.

Magnetic ordering changes on the hydrogenation (see Table 1 for the details). Most frequently magnetic moment carried by the rare earth decreases while the temperature of magnetic ordering decreases as well. For the Kondo semimetal CeNiSn the hydrogenation induces antiferromagetism in CeNiSnD.

4.3.2.1. Magnetic ordering in TbNiSnD [71]. The neutron powder diffraction study of the crystal and magnetic structure of TbNiSnD shows that the deuteride crystallizes with the filled TiNiSi type structure (S.G. *Pnma*; a = 7.0354(1); b = 4.20662(9); c = 8.1808(2) Å at 293 K; a = 7.008(1); b = 4.1954(6); c = 8.153(1) Å at 2 K) and is canted ferromagnetic below 10 K. The deuterium atoms occupy the tetrahedral Tb_3Ni sites. The Tb atoms carry a magnetic moment of 6.6(1) μ_B /Tb. They order antiferromagnetically along the a-axis and ferromagnetically along the c-axis. No significant magnetic moment on the Ni atoms has been observed by neutron diffraction. Insertion of deuterium in TbNiSn causes dramatic changes of the original magnetic structure of TbNiSn and a reduction of the magnitude of the Tb magnetic moment.(Fig. 14, Fig. 15 and Fig. 16).

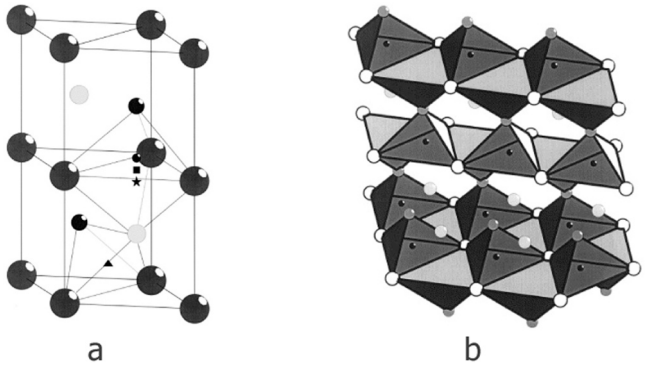

Fig. 13. (a) Selected possible hydrogen sites in *RTX* hydride with TiNiSi type structure. *R*: large atoms. *T*: dark medium atoms. *X*: light medium atoms. Interstitial sites: R_3T site (•), R_3TX(■), R_3X (*) and R_2TX (▲). The coordinations polyhedra are outlined. (b) Structure of $TbNiSiD_{1.78}$ illustrated as D (Tb_3Ni) tetrahedra sharing Tb–Tb edges and Ni corners [70]. Si (shaded isolated atoms) does not form bonds with hydrogen. Tb atoms are white and Ni atoms shaded.
(Reprinted with permission from [70]. Copyright (2001) Elsevier).

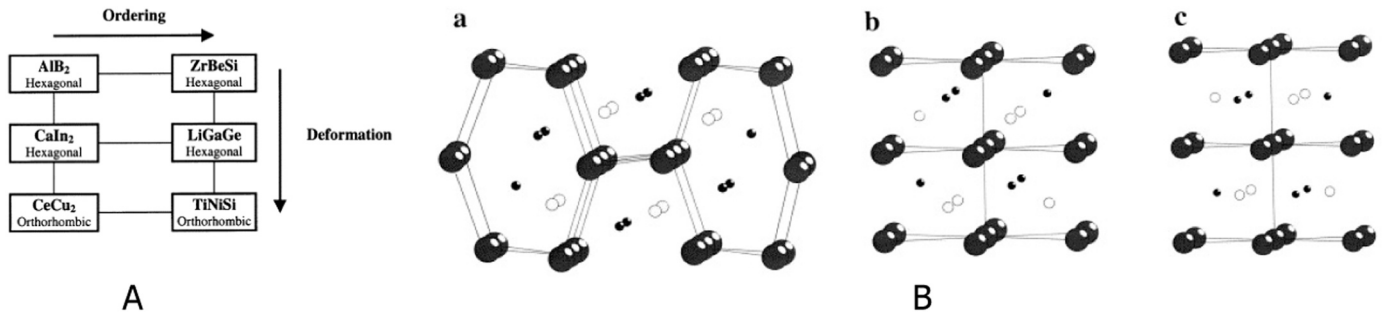

Fig. 12. (A) An overview of the related structure types which for the ABC stoichiometries include ZrBeSi, LiGaGe and TiNiSi types. (B) Comparison of the different structure types (a) TiNiSi, (b) LiGaGe and (c) ZrBeSi. The latter two have AA stacking of close-packed layers of R and differ by displacement of the smaller T and X (light) atoms, whereas the former is more distorted.
(Reprinted with permission from [70]. Copyright (2001) Elsevier).

Table 1
Crystallographic and magnetic properties of the ternary intermetallic compounds and their hydrides.

	Structure type and symmetry	Unit cell dimensions, Å	V, Å^3	Type of magnetic ordering	Ordering Tempe-rature, K	Size of magnetic moment on R atoms, μ
$ErMn_2$	$MgZn_2$, hexagonal, $P6_3/mmc$	5.29416 8.64435 (350 K)		Ferromagnetic	15	7.72
$ErMn_2D_2$	$MgZn_2$, hexagonal, $P6_3/mmc$ (350 K)	5.56787 9.07088		Ferrimagnetic	205	9.6
	Derivative from $MgZn_2$, monoclinic, $C2/m$ (150 K)	9.61247(9) 5.57558(4) 9.07102(8) β = 90.5451(5)	486.140(7)			
CeNiSn	TiNiSi, orthorhombic, *Pnma*	7.54(1) 4.599(6) 7.639(9)	264.89	-	-	-
CeNiSnD	Deformed TiNiSi, orthorhombic, $Pna2_1$	7.238(4) 8.446(4) 4.398(2)	268.86	AF, with ferromagnetic sheets ordering + -+ -	5.1	1.37
TbNiSn	TiNiSi orthorhombic, *Pnma*	7.02204(8) 4.42515(5) 7.62601(9)	236.97	AF sine-modulated	18.5	8.9
TbNiSnD	TiNiSi orthorhombic, *Pnma*	7.0354(1) 4.20662(9) 8.1808(2)	242.112(9)	Canted ferromagnetic ordering	10	6.6
HoNiSn	TiNiSi orthorhombic, *Pnma*	7.0682(9) 4.4396(6) 7.6433(9)	239.85	AF sine-modulated	3	8.27
$HoNiSnD_{0.67}$	ZrNiAl Hexagonal, $P\bar{6}2m$	7.24197(10) 3.93514(7)	238.31	AF sine-modulated	2.6	5.36
TbNiSi	TiNiSi, orthorhombic, *Pnma*	6.8715(23) 4.1439(17) 7.1508(35)	203.62(25)	AF sine-modulated	16	8.28
$TbNiSiD_{1.78}$	ZrBeSi hexagonal, $P6_3/mmc$	4.02895(7) 7.9585(2) (100 K)	223.76	AF	8	8.71

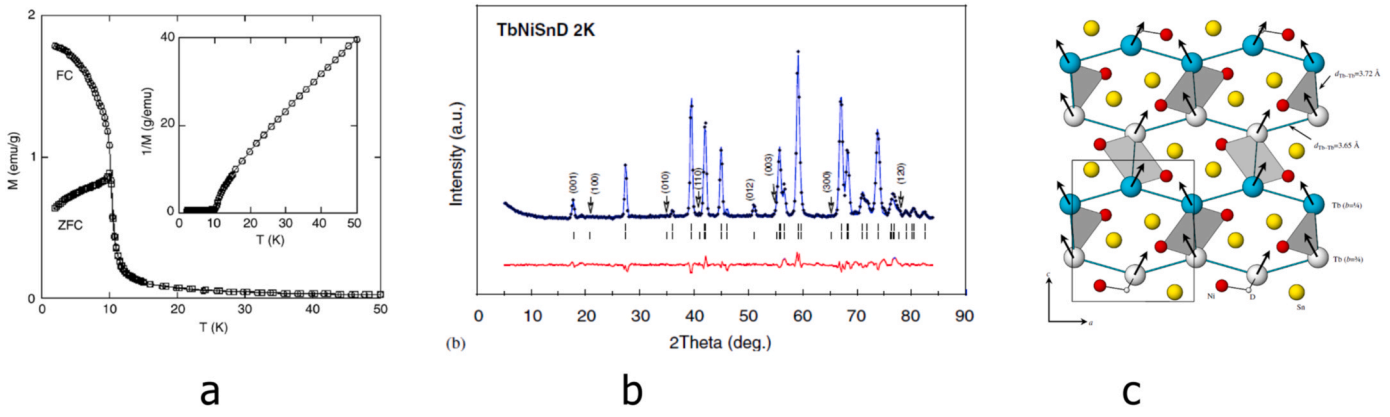

Fig. 14. (a) The zero-field-cooled (ZFC) and field-cooled (FC) magnetization curves show ordering of the magnetic structure proceeding below 10 K; (b) Neutron powder diffraction pattern measured below the ordering temperature at 2 K have a contribution from the nuclear and magnetic (shown by arrows) structures; (c) TbNiSnD has a canted ferromagnetic structure with a ferromagnetic component parallel to the *c*-axis and an antiferromagnetic component parallel to the *a*-axis.
(Reprinted with permission from [71]. Copyright (2006) Elsevier).

4.3.2.2. Magnetic ordering in $TbNiSiD_{2-x}$ [70,72]. The intermetallic compound TbNiSi adopts the orthorhombic TiNiSi-type structure (S.G. *Pnma*) [70]. Deuteration/hydrogenation) leads to increased symmetry from the orthorhombic to the hexagonal ZrBeSi-type structure ($P6_3/mmc$) for $TbNiSiD_{1.78}$ [70]. By powder neutron diffraction, the magnetic ordering of TbNiSi was determined to be sinusoidal wave modulated below the Néel temperature at 16 K, and square-modulated below 9 K [72]. The magnetic moment of Tb (8.28 μ) is aligned along **b**.

Below the magnetic ordering temperature of 10 K, at 2 K $TbNiSiD_{1.78}$ a small orthorhombic distortion of the lattice takes place. The refined unit-cell dimensions at 2 K (S.G. *Pnma*) are a= 7.9505(2), b= 4.02502(14), c= 6.9823(2) Å. The magnetic moments of Tb are 8.71(6) μ, and are ordered antiferromagnetically along **a**.

4.3.2.3. Magnetic ordering in CeNiSnD [73]. Neutron diffraction and magnetic measurements were used to investigate the changes in magnetic properties of the Kondo semimetal compound CeNiSn after charging with deuterium gas under moderate conditions. Charging with deuterium led to the formation of the monodeuteride CeNiSnD with filled TiNiSi structure. This compound gives rise to long-range antiferromagnetic ordering below T_N = 5.1 K. The ordered magnetic

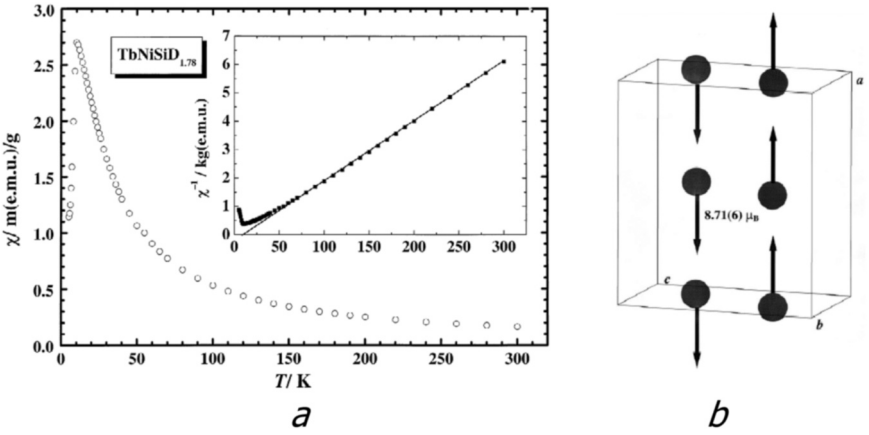

Fig. 15. (a) Magnetic susceptibility of $TbNiSiD_{1.78}$ in the applied field 1000 Oe as a function of temperature showing a magnetic ordering below 4 K. (Inset) Inverse magnetic susceptibility revealing a Curie–Weiss behaviour above 70 K. (b) The magnetic structure of TbNiSiD1.78 with the magnetic moments of Tb atoms aligned along *b*.
(Reprinted with permission from [72]. Copyright (2002) Elsevier).

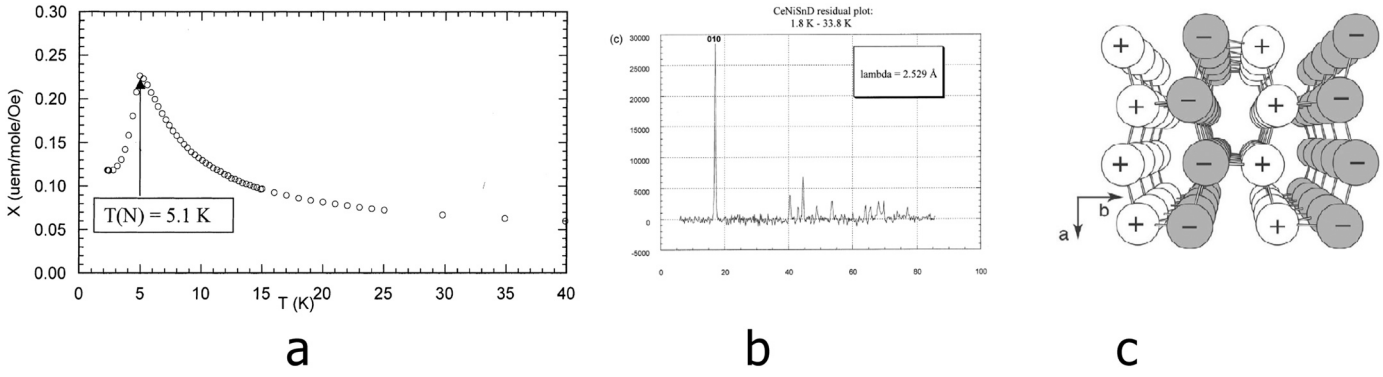

Fig. 16. (a) Temperature dependence of the magnetic susceptibility for CeNiSnD peaking at T_N = 5.1 K. (b) Difference plot of the neutron diffraction diagrams of the compound CeNiSnD at 33.8 K and at 2 K showing peaks of magnetic diffraction. (c) Stacking of the ferromagnetic layers along [010] in the magnetic structure of CeNiSnD. Ce moments are aligned along [001]. Opposite spins are indicated as + and -.
(Reprinted with permission from [73]. Copyright (2006) Elsevier).

moment value equals 1.37(3) μ per Ce atom, the moments pointing along the [001] direction. No significant ordered magnetic moments on the Ni atoms have been observed by powder neutron diffraction.

4.3.2.4. Magnetic ordering in $HoNiSnD_{0.67}$ [74,75]. The deuteration of HoNiSn intermetallic compound causes a change of the crystal structure from orthorhombic TiNiSi-type to the hexagonal ZrNiAl-type and a small volume contraction, − 0.64%. The atomic structure of $HoNiSnD_{0.67}$ is isostructural with chemically similar lower deuterides $RNiInD_{0.5-0.6}$ formed by La and Nd [76]. D atoms are partially filling the available Ho_3Ni tetrahedra.

The magnetic ordering of $HoNiSnD_{0.67}$ is antiferromagnetic with the Néel temperature 2.6(3) K. Initial intermetallic compound HoNiSn is antiferromagnet as well, and its ordering temperature, 3.0 K, remains practically unchanged on the hydrogenation.

However, inserted hydrogen atoms cause change of the type of magnetic ordering. The reflections of magnetic origin, observed on the neutron diffraction pattern at 2 K (see Fig. 17a) are indexed by the propagation vector k_1(= 0.34, 0.34, 0.117) for $HoNiSnD_{0.67}$ and k_2(= 0.395, 0.330, 0) for HoNiSn. The Ho magnetic moment associated with k_1 equal to 5.36(5)μ_B, lies in the basal plane (0 0 1) and forms a sine modulated structure (see Fig. 17b). The three moments in the crystal unit cell form noncollinear order. The magnetic moment on Ho atoms decreases as compared to the intermetallic HoNiSn (8.5 μ_B).

Other studied RENiSn based hydrides include $LaNiSnH_2$, PrNiSnH, NdNiSnH and $SnNiSnH_{0.6}$ [77–79].

4.3.3. Multi-peak Thermal Desorption of deuterium in the YFe_2-D_2 system [60]

The study of the YFe_2-H_2 system attracted much attention regarding the influence of hydrogen absorption on the magnetic properties of RFe_2 compounds (*R* = rare earth), its multi-plateau thermodynamic behaviour and the large variety of crystal structures for different hydrogen contents. The parent compound YFe_2 crystallizes in the cubic C15 Laves phase structure (S.G. $Fd\bar{3}m$). On increasing hydrogen content, different single phase-hydrides such as $YFe_2H_{1.3}$ (tetragonal $I\bar{4}$), $YFe_2H_{1.75}$, (cubic $I\bar{4}3m$), $YFe_2D_{1.9}$ (tetragonal $I\bar{4}$), $YFe_2H_{2.6}$ (cubic $Fd\bar{3}m$), $YFe_2H_{3.5}$ (rhombohedral $R\bar{3}m$), $YFe_2H_{4.2}$ (monoclinic *Pc*) and YFe_2H_5 (orthorhombic $Pmn2_1$) are formed [80–83]. In some cases, their neutron diffraction patterns display superstructure lines due to hydrogen ordering and the induced displacement of Y and Fe atoms to accommodate D-atoms [81]. The case of $YFe_2H_{4.2}$ compound has received particular attention because a large isotopic effect is observed on the magnetic properties of the $YFe_2(H,D)_{4.2}$ system [84,85]. Replacing deuterium with hydrogen leads to a sharp increase in the abrupt magnetostrictive transition, which has been attributed to the large cell volume difference between hydride and deuteride.

In situ neutron diffraction experiments in the YFe_2-H_2 system have been focused on the formation and thermal ordering of $YFe_2HD_{1.3}$, $YFe_2D_{1.75}$ and $YFe_2D_{1.9}$ [81] as well as the thermal stability of YFe_2D_x ($1.3 \le x \le 4.2$) deuterides [60]. For the latter studies, the aim was to shed new light on the multi-peak TD spectrum observed in this system and in general in AB_2 compounds [86,87]. Neutron

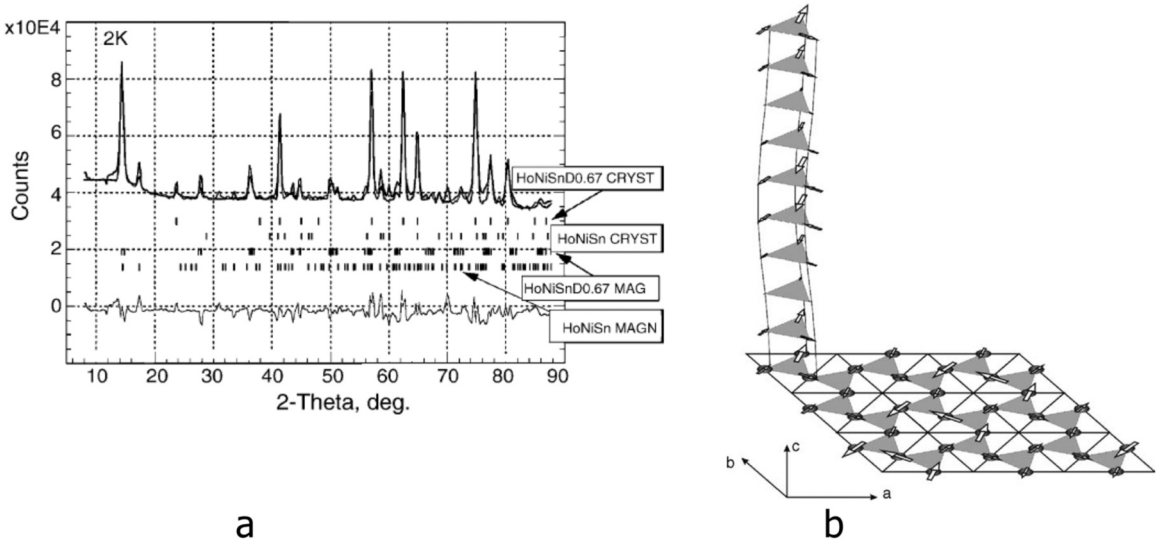

Fig. 17. (a) Observed and calculated neutron diffraction patterns of $HoNiSnD_{0.67}$ at 2 K. Circles represent the experimental data, solid lines are for the calculated profile and at the bottom the difference between the observed and calculated data is shown. Vertical bars indicate the nuclear and magnetic peaks. 2 crystallographic structures and 2 magnetic structures were accounted during the refinements: (b) Magnetic structure of $HoNiSnD_{0.67}$. Only carrying magnetic moment Ho atoms are shown with a direction of the magnetic moments indicated by arrows.
(Reprinted with permission from [75]. Copyright (2005) Elsevier).

diffraction experiments were performed at D1B@ILL beamline during thermal desorption of $YFe_2D_{4.2}$ compound. The sample was put in a stainless steel holder that was placed in a furnace with vanadium heating elements. The sample holder was heated from RT to 650 K with a ramp of 0.5 K/min and connected through a vacuum line equipped with a Pirani gauge and a rotary pump [60].

Fig. 18 shows the evolution of neutron diffraction patterns (Fig. 18c) and TD data (Fig. 18a) during thermal desorption of $YFe_2D_{4.2}$. On heating up to 360 K, the primitive monoclinic structure (S.G. *Pc*) of this compound transforms, before the onset of deuterium desorption, to the high-symmetry cubic C15 structure (S.G. $Fd\bar{3}m$) as result of an order/disorder transition (Fig. 18c). With further heating, C15 diffraction peaks shift to higher angles indicating the shrinking of C15 unit-cell volume due to deuterium desorption (Fig. 18b). The C15 structure is retained throughout the desorption process, but in the temperature range of 430–480 K, where superstructure lines belonging to $YFe_2D_{1.9}$ and $YFe_2D_{1.75}$ are observed. In addition, the line widths of the diffraction peaks undergo significant broadening from 350 to 445 K and from 495 to 560 K. Indeed, it has been shown that the temperatures at which these structural discontinuities occur are strongly correlated to the singularities of the TD spectrum (Fig. 18a). The TD spectrum could be deconvoluted in seven desorption events, each one related to deuterium release as a consequence of two-phase transformation between deuterides. This *in situ* study proved that the multi-peak TD spectra observed in YFe_2D_x deuterides are due to the many different phases that occur in this system as a function of deuterium content. In the past, multi-peak spectra in AB_2 compounds were attributed to different local H environments in the C15 lattice, a fact that is questioned by the present study.

4.3.4. Ternary hydrides of $Nd_6Fe_{13}Si$ and Mo_2FeB_2 types

NPD studies of $Nd_6Fe_{13}GaD_{12.3}$ showed that deuterium atoms nearly completely occupy four different types of interstices, comprising Nd_2Fe_4 octahedra and three types of tetrahedra, Nd_4, Nd_3Fe and Nd_2Fe_2 [88]. $Pr_6Fe_{13}AuD_{13}$ has a similar nuclear structure with deuterium atoms occupying various types of interstitial sites bounded with Pr and Fe atoms. A collinear antiferromagnetic ordering of the four Fe and the two Pr sublattices for the uncharged $Pr_6Fe_{13}Au$ compound transforms into a collinear ferromagnetic structure of the deuteride [89].

An antiferromagnet Nd_2Ni_2Mg with the Neel temperature $T_N \sim 19$ K forms a $Nd_2Ni_2MgH_8$ hydride where the T_N becomes significantly decreased, to just 1 K [90]. The Hydrogenation of Nd_2Ni_2Mg leads to a pronounced deformation of the constituting it AlB_2 and CsCl type blocks. A dynamic distribution of hydrogen atoms and no formation of covalent Ni-H complex ions are concluded for the structure of $Nd_2Ni_2MgH_8$ (the results will be published separately).

5. Hydrogen pressure-dependent transformations

5.1. Studies at pressures 1–100 bar D_2

5.1.1. AB_5-H_2 systems

5.1.1.1. $LaNi_{4.70-4.78}Sn_{0.22-0.30}$-$H_2$ system [91,92]. A specially designed cell for *in situ* studies (the studied sample is kept in a quartz glass capillary) by using synchrotron X-ray powder diffraction (SR XRD) in H_2-atmosphere has been used to monitor phase-structural transformations during hydride formation and decomposition in the advanced hydrogen storage alloy $LaNi_{4.70-4.78}Sn_{0.22-0.30}$. The cell was attached to a metal hydride hydrogen storage unit developed at IFE providing hydrogen gas at convenient constant temperature-dependent pressures. Temperature cycling between RT and 100 °C at H_2 pressures of 2–3 bar was employed to $LaNi_{4.70}Sn_{0.30}H_{\sim 6}$ which resulted in a reversible hydrogen absorption–desorption process (see Fig. 19). A large temperature-dependent homogeneity range of the β-hydride and a small hysteresis in the formation-decomposition of the β -hydride were revealed.(Fig. 20).

5.1.1.2. $La_{0.5}Ce_{0.5}Ni_4Co$-H_2 system [93]. A hexagonal $CaCu_5$-type $La_{0.5}Ce_{0.5}Ni_4Co$ intermetallic alloy was studied as H storage material in as-cast condition using PCT and *in situ* SR XRD studies performed between 263 and 353 K. A significant shrinking of the unit cells takes place on a substitution of La with Ce. SR XRD showed the formation of two hexagonal hydrides, a γ-trihydride $La_{0.5}Ce_{0.5}Ni_4CoH_3$, and a saturated β-hexahydride $La_{0.5}Ce_{0.5}Ni_4CoH_{\sim 6}$. In addition, an α-H solid solution was experimentally observed. Hysteresis of hydrogen

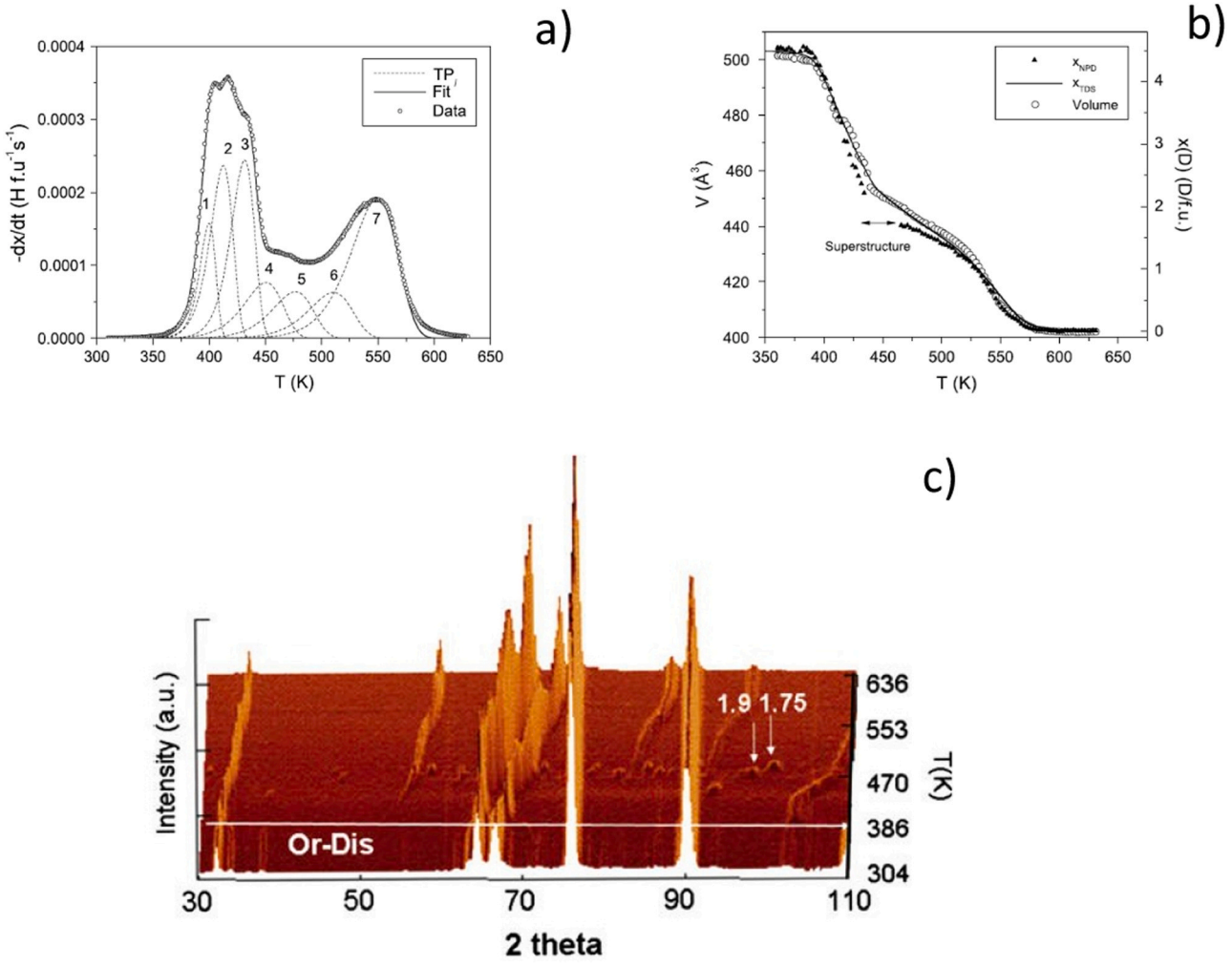

Fig. 18. Simultaneous acquisition of thermal desorption (TD) spectrum and neutron-diffraction (ND) patterns of $YFe_2D_{4.2}$. Heating rate 0.5 K/min. a) TD spectrum of $YFe_2D_{4.2}$ deconvoluted in seven desorption events assigned to seven phase transformations. b) Evolution of C15 unit cell-volume (left-axis) and deuterium content in YFe_2 (right-axis) with temperature. Deuterium contents are evaluated from Rietveld refinement of ND data and integration of TD spectrum. c) 3D representation of ND patterns with temperature. The arrows indicate superstructure lines denoting the formation of intermediate deuterides $YFe_2D_{1.9}$ and $YFe_2D_{1.75}$.
(Reprinted with permission from [60] Copyright (2008) Elsevier).

absorption and desorption between the flat single plateaux isotherms measured during the PCT measurements was rather small, with no indication of the formation of the thermodynamically stable γ-(La,Ce)$(Ni,Co)_5H_3$. The SR XRD revealed (see Fig. 20) that (a) the relative abundance of the γ-hydride is higher during the desorption compared to the absorption; its relative amount reaches 50 wt% in maximum; (b) anisotropic strains in all constituent phases during both hydrogen absorption and desorption are not developed; (c) the pressure of the formation of the γ-phase was found to be strongly temperature-dependent. The formation of large amounts of metastable γ-(La,Ce)$(Ni,Co)_5H_3$ hydride in quasiequilibrium experimental conditions applied during the SR XRD experiments and during reaching the thermodynamic equilibrium between the constituent phases can be responsible for the reduced hysteresis of the PCT isotherms and absence of noticeable anisotropic strains in the constituent phases.

5.1.2. Over-stoichiometric $LaNi_{5+x}$ - $LaNi_6$-H_2 system

In situ neutron diffraction studies were performed on highly over-stoichiometric $LaNi_{5+x}$ with x = 1.0 - $LaNi_6$ alloy - during the monitoring of desorption PCT curve from its deuteride at room temperature.

Experiments were performed at D1B@ILL at deuterium pressures between 0.01 and 10 MPa using a stainless steel sample holder and the Sieverts' apparatus shown in Fig. 6 (Section 3). Contrary to the stoichiometric composition $LaNi_5$ which crystallizes in $CaCu_5$ structure-type, the crystal structure of over-stochiometric $LaNi_{5+x}$ alloys is better described in the $TbCu_7$-type structure in which La atoms are partially substituted by *c*-axis oriented Ni-dumbbells which can by thus described by the formula $La_{1-y}Ni_{5+2y}$. A highly-overstoichiometric $La_{0.88}Ni_{5.24}$ alloy (roughly corresponding to the $LaNi_6$ composition) was synthetized by using mechanochemical treatment and exists as a metastable phase [94]. The PCT desorption curve is displayed in Fig. 21 and is compared to that of the hydride of stoichiometric $LaNi_5$ intermetallic alloy. In contrast to the $LaNi_5$-H_2 system, the highly overstoichiometric compound shows no clear plateau pressure and a maximum H storage capacity of 4.9 at.D/unit cell at 10 MPa D_2. However, as displayed in Fig. 21, a phase transition from β-deuteride to α-solid solution shows a reduced $\alpha+\beta$ coexistence region. This transition exhibits variable α- and β-lattice volumes and a minor value of a discrete lattice expansion (ΔV/V = 3.5 vol.%) as compared to the stoichiometric $LaNi_5$ (ΔV/V=21.5 vol.%).

5.1.3. Laves type AB_2 deuterides with C14, C15 and C36 structures

Hydride structures based on the Laves phases of composition $(Sc,Ti,Zr)T_2$ (*T* = transition metal of the first row) with C14 $MgZn_2$, C15 $MgCu_2$ and C36 $MgNi_2$ structure types have been studied in

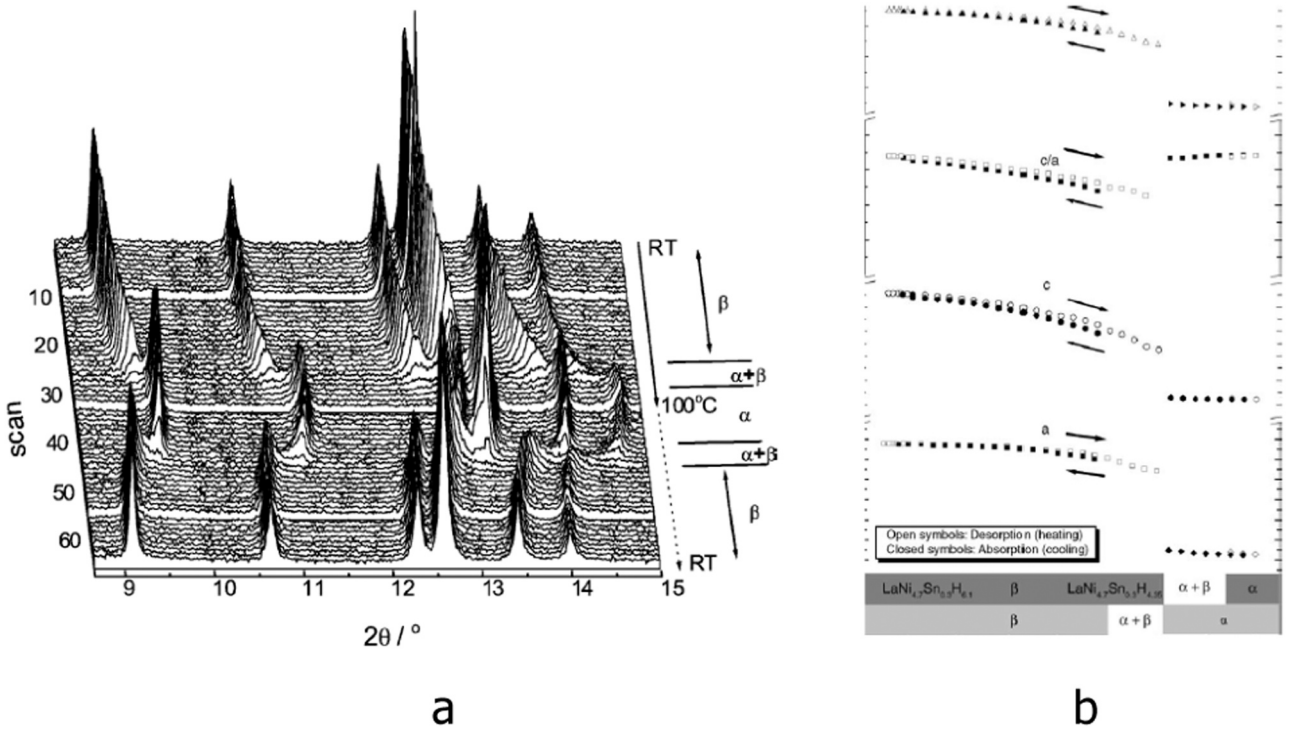

Fig. 19. (a) Powder diffraction profiles during transformation of β-phase to α-phase on heating the saturated with hydrogen sample from 25° to 100°C in H_2 gas and subsequent cooling to 25 °C to form back the β-phase.(b) Variations of the unit-cell dimensions of β-hydride and α-phase as a function of temperature.
(Reprinted with permission from [92]. Copyright (2005) Elsevier).

detail [95–102]. Laves phase structures contain three different kinds of tetrahedral interstices: R_2T_2, RT_3 and T_4. When hydrogen content in the hydrides does not exceed H/RT_2 = 2.8–3.0, the R_2T_2 sites are the only ones being filled ($TiFe_{1.16}V_{0.84}D_{2.1}$ [95], $ZrMoFeD_{2.6}$ [96], λ_1-$ScFe_2D_{2.5}$ [97], λ_1-$ScFe_{1.5}Si_{0.5}D_{2.1}$ [97], λ_3-$ScFe_2D_{2.9}$ (the only studied $MgNi_2$ C36 type hydride, D atoms fill Sc_2Fe_2 sites of 6 types [98]), $ZrV_2D_{1.5}$ [99]). When the hydrogen content increases up to about the saturation limit, the hydrogen atoms become accommodated in the RT_3 and T_4 interstices, which have less space and are less attractive in their surrounding for H atoms. Thus, in the $ZrV_2D_{2.8}$ deuteride [99], a partial filling of the ZrV_3 interstices (5% of the total number of D atoms) was observed. In the $ZrV_2D_{4.5}$ deuteride the main part of deuterium atoms in excess of D/ZrV_2 = 2.8 is located in the ZrV_3 interstices, and this raises the fraction of the filled ZrV_3 interstices to ~ 1/3. This can be related to the progressing H content expansion of the unit cells, which causes the calculated values of the radii of the

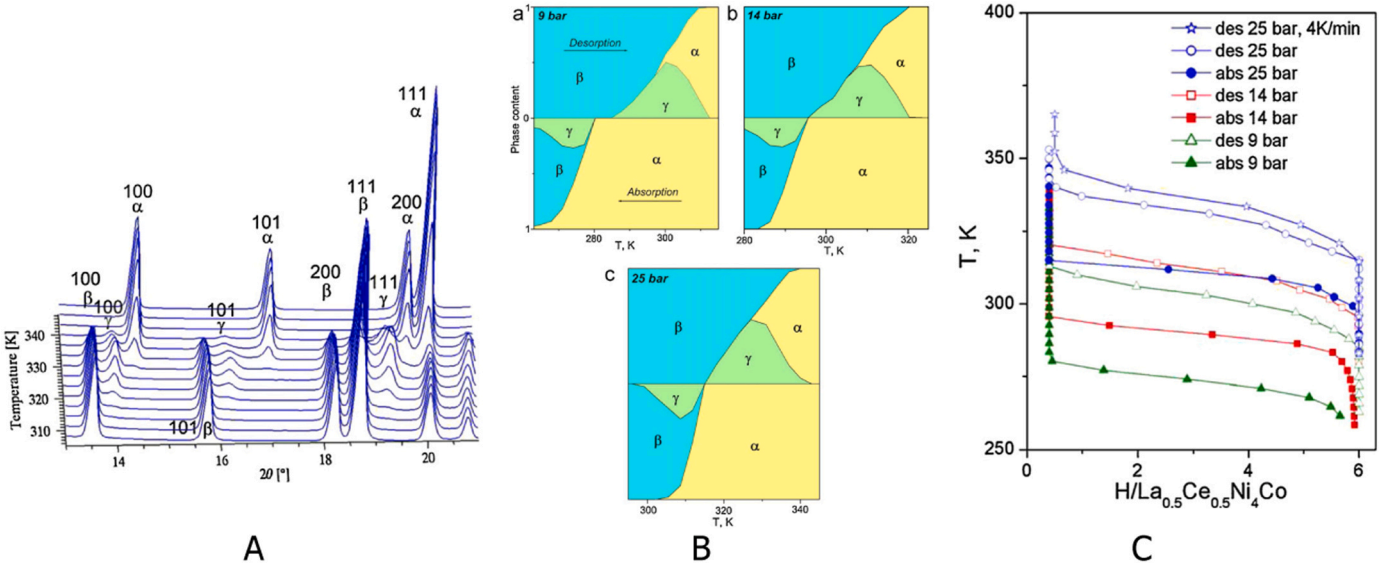

Fig. 20. (A) Temperature evolution of the *in situ* SR XRD pattern during hydrogen desorption from the β-$La_{0.5}Ce_{0.5}Ni_4Co_{H\sim6}$ hydride. Miller indices of the diffraction peaks for three constituent phases are shown. (B) Phase-structural composition of the $La_{0.5}Ce_{0.5}Ni_4Co$–H_2 system from the refinements of the SR XRD data during isobaric desorption (upper part; heating) and absorption (lower part, cooling) with a heating/cooling rate of 2 K/min under isobaric conditions, 9 bar H_2 (a), 14 bar H_2 (b) or 25 bar H_2 (c). (C) Calculated isobars of hydrogen desorption and absorption built on the basis of the refined SR XRD data.
(Reprinted with permission from [93]. Copyright (2010) Elsevier).

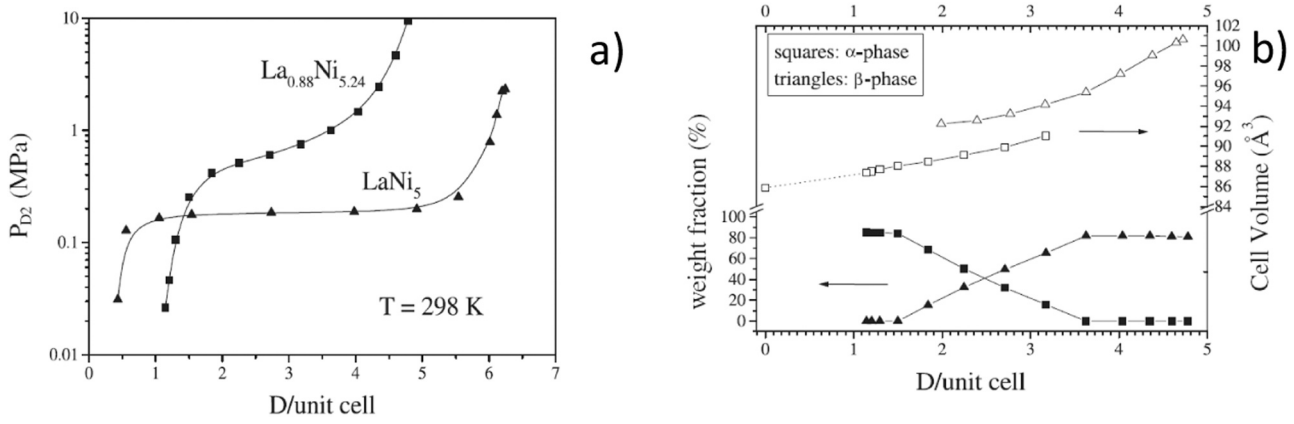

Fig. 21. a) PCT deuterium desorption isotherms for stoichiometric $LaNi_5$ and over-stoichiometric $LaNi_6$ ($La_{0.88}Ni_{5.24}$) alloys measured at 298 K. b) Evolution of weight fraction (full symbols) and unit-cell volumes (empty symbols) of α- and *β*-phases for overstoichiometric $LaNi_6$ during *in situ* monitoring by neutron diffraction when performing PCT desorption studies.
(Reprinted with permission from [35]. Copyright (2002) Elsevier).

ZrV_3 interstices to exceed 0.4 Å. This creates chemical conditions suitable for stable metal hydride formation: $d_{M-i} > r_M + 0.4$ Å [100].

In the C14 type $ZrVFeD_{3.6}$, $ZrVCuD_{4.0}$ and $ZrVNbD_{5.4}$ deuterides [101] in addition to the preferentially occupied $Zr_2(V,T)_2$ interstices, deuterium atoms also partially fill $Zr(V,T)_3$ and $(V,T)_4$ interstices: 3% and 0%, 4% and 7%, 3% and 0%, respectively, of the total number of hydrogen atoms. All filled interstices have radii exceeding 0.4 Å.

One typical example of the C15 type hydride is a multi-component $(Ti,Zr,V)(Ni,Mn,Fe,V)_2D_{3\pm x}$ which for the alloy's composition $Ti_{0.2}Zr_{0.8}La_{0-0.05}Ni_{1.2}Mn_{0.7}V_{0.12}Fe_{0.12}$ showed occupancy of the A sites not only by Ti and Zr but also by V and exclusive filling by D atoms of the A_2B_2 tetrahedral sites (see Fig. 22) [102].

A number of ordered superstructures of D atoms in the metal lattice are formed in the C15 types hydrides at low temperatures [93]. When D/AB_2 does not exceed 4 at.H/f.u., various types of ordering in the A_2B_2 tetrahedra are realised. Interestingly, for the highest H/D content reached for ZrV_2D_6, the 3 Zr_2V_2 + 3 ZrV_3 ordering is realised [103], as in the expanded crystal lattice ZrV_3 tetrahedra become equally attractive for the accommodation of D atoms as the Zr_2V_2 tetrahedral sites.

5.1.4. *Ti(Fe,Mn)-H_2 system [55]*

TiFe-based alloys have recently regained considerable interest for reversible hydrogen storage near room temperature due to their relatively high hydrogen content (1.87 wt% and 105 kg_H/m^3 for $TiFeH_2$) and their low cost as compared to other intermetallics [104]. The equilibrium hydrogen pressure can be finely tuned by a partial chemical substitution to adapt the operating conditions to the specific applications [105]. The crystal structure of $TiFe_{0.90-x}Mn_x$ alloys (x = 0, 0.05 and 0.10) and their deuterides has been determined by *in situ* neutron diffraction, while recording Pressure-Composition Isotherms at room temperature [55]. Experiments were performed at D1B@ILL at deuterium pressures from 0.02 to 9 MPa with the help of a Sieverts' apparatus (see Fig. 6). Fig. 23a shows the evolution of 2D diffraction patterns for x = 0.05 during a whole desorption/absorption PCI measurement. Three phases were detected, and their amount determined (Fig. 23b): α-cubic solid solution (S.G. $Pm\bar{3}m$), *β*-orthorhombic mono-deuteride (S.G. $P222_1$) and γ- orthorhombic dideuteride (S.G. *Cmmm*). Mn substitution does not significantly change the volumetric expansion during the phase transitions, affecting only the deuterium content for the γ phase and the variation of cell volume for the β phase. Volume expansions are 11–15% for the β phase and 17% for the γ phase, with respect to the dehydrogenated α phase (Fig. 23c). This parameter is of high industrial relevance and should be properly considered for the integration of TiFe-type alloys in hydrogen tanks.

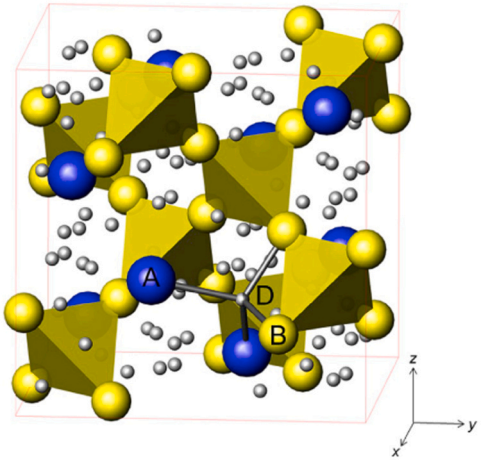

Fig. 22. The crystal structure of the cubic $AB_2D_{2.9}$ deuteride [102]. D atoms partially, 24%, fill 96 *g* sites shown as small spheres. A, B and D represent Zr/Ti/V (8a), Ni/Mn/Fe/V (16d), and D atoms, respectively. Spatial framework of B_4 tetrahedra is shown.
(Reprinted with permission from [102]. Copyright (2019) Elsevier).

5.2. Studies of metal-H systems at high pressures up to 1000 bar D_2

5.2.1. *$CeNi_5$-D_2 [39,40]*

The initial deuteration of a single phase $CeNi_5$ intermetallic with $CaCu_5$ type structure (a = 4.88415(7); c = 4.00016(7) Å) was performed on D1B at ILL without a preliminary activation of the alloy by applying high deuterium pressures. A solid solution of deuterium in $CeNi_5$, α-$CeNi_5D_{\sim 0.5}$, was formed first which extended until 600 bar D_2. At higher deuterium pressures the α-$CeNi_5D_{\sim 0.5}$→*β*-$CeNi_5D_{\sim 6.3}$ transformation took place. During the first deuteration, the midpoint of the α→*β* plateau at 20 °C was observed at 632 bar D_2; maximum D content in the saturated beta deuteride, according to the volumetric measurements, equals 6.5 at.D/f.u. at ~800 bar D_2. During the deuterium desorption, the midpoint of the plateau pressure for the *β*→α transformation was observed at a significantly lower pressure, 117 bar D_2 at 60 °C (see Fig. 24a). Variation of the NPD pattern as related to the pressure of D_2 desorption is shown in Fig. 24b. During the second deuteration, a mid-plateau pressure for the α→*β* transformation at 30 °C was significantly decreased, to just 237 bar D_2. (Fig. 25).

A small difference between the data of the volumetric measurements and the results of the crystal structure refinements can be

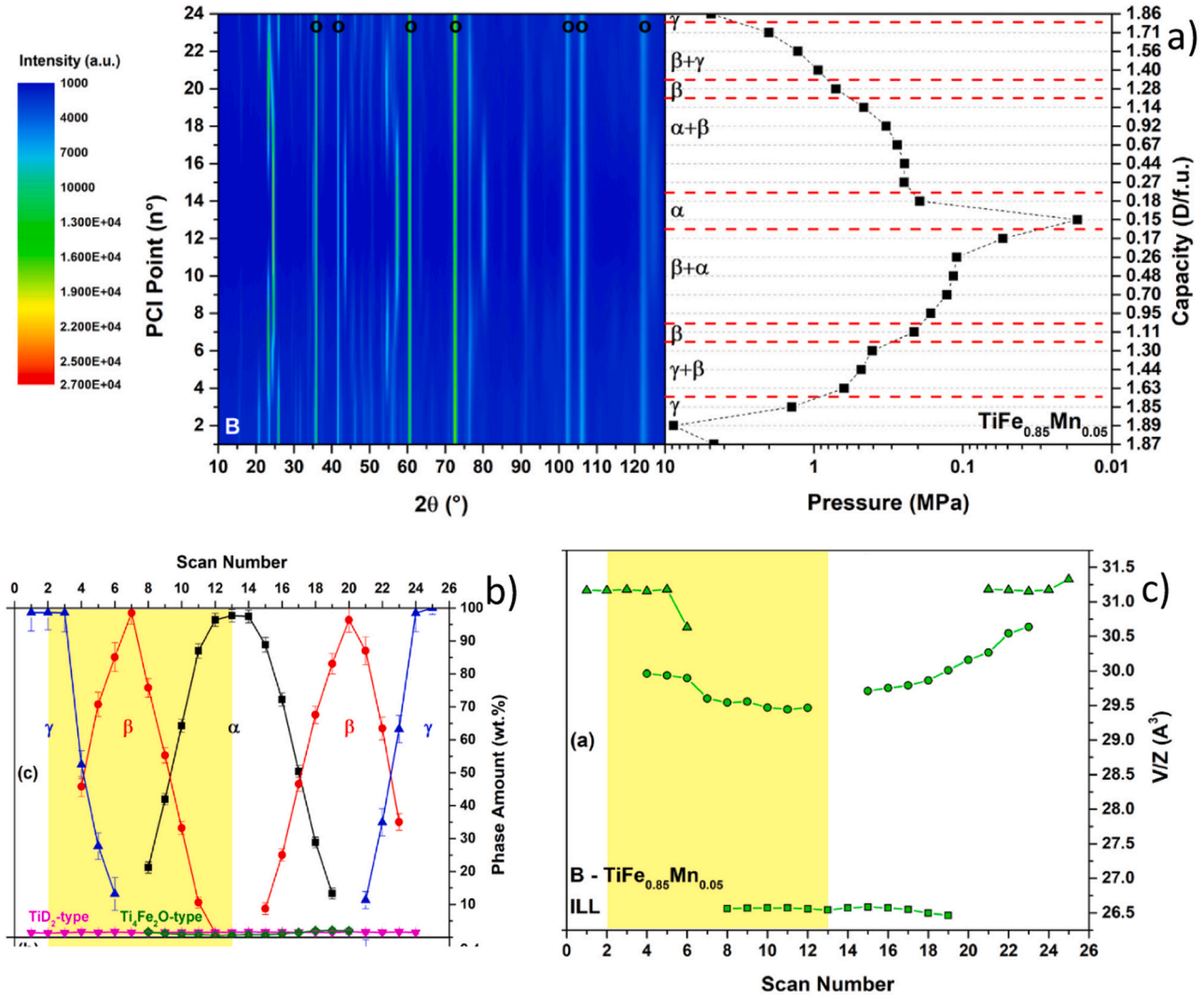

Fig. 23. a) *In situ* neutron diffraction 2D patterns (counter plot, λ = 1.286 Å) and PCI curve at RT during deuterium desorption /absorption at D1B@ILL between 0.02 and 9 MPa for $TiFe_{0.85}Mn_{0.05}$ alloy. Diffraction lines from the stainless steel sample holder are marked by a circle (o). b) amount of α, β and γ phases, c) Normalized cell volume for phases α (□),*β*-(O) and γ(Δ).
(Reprinted with permission from [55]. Copyright (2023) Elsevier).

caused by the presence of undistinguishable (by neutron diffraction) amounts of the *β*-deuteride (*ca.* 5%) in the sample already at 613 bar D_2. Such small quantities are difficult to confidently identify using the NPD data with a lower resolution, as at the D1B instrument. However, the high flux beam allowed fast collection of a single data set, on a time scale of approximately 2 min, allowing kinetic measurements of the processes of phase-structural transformations caused by absorption or desorption of deuterium gas.

NPD data showed a complete transformation into the *β*-deuteride at D_2 pressure of 776 bar. During the deuteration, the unit cell expands by 30.1%, with Δa/a = 10.0% and Δc/c = 7.5%. Volume expansion during the formation of the *β*-$CeNi_5D_{6.3}$ is significantly larger as compared to $LaNi_5D_{6.5}$ (~24%) [106]. No superstructure peaks were observed in the NPD pattern; thus, the structure of the $CeNi_5D_{6.3}$ deuteride was described in the space group *P*6/*mmm*. However, a possible hydrogen ordering in the structure resulting in the doubling of the unit cell and lowering of the symmetry cannot be excluded, similar as in the *β*-$LaNi_5D_{6+x}$ [107].

Three different interstitial sites were found to be partially filled by D atoms, including Ce_2Ni2_2 tetrahedra; Ce_2Ni1_2Ni2 sites (half of the octahedron $Ce_2Ni1_2Ni_2$) and tetrahedra Ni_4. Refined deuterium content of 6.3(2) at.D/f.u. agrees well with the volumetric measurements, 6.5 D/f.u. The values of the unit cell parameters for the saturated $CeNi_5D_{6.3}$ deuteride, a = 5.374(2); c = 4.3012(7) Å, are very close to the corresponding values for $LaNi_5D_6$. This is in contrast to a significant difference between the sizes of the unit cells for $LaNi_5$ and $CeNi_5$, where a significant contraction of the unit cells takes place on a replacement of La by Ce. Thus, a decrease of the Ce valence from a partial 4^+ state in $CeNi_5$ to a trivalent state in $CeNi_5D_{6.3}$ is likely to take place during the hydrogenation process.

Finally, a pronounced anisotropic diffraction peak broadening upon the first hydrogenation of the $CeNi_5$ was observed, during the α-$CeNi_5D_{\sim 0.5}$→*β*-$CeNi_5D_{\sim 6}$ transformation. The anisotropic strain broadening is not observed in the initial period of the hydrogenation, until the *β*-deuteride appears and, after that, remains a component of the metal–hydrogen system during further desorption–absorption cycling. Such an anisotropic broadening is attributed to the misfit dislocations created during the first hydrogenation. During the refinements, the anisotropic peak broadening was modelled using the function developed by Latroche et al. [108], where it is described as originating from the local variations of the unit cell parameters *a* and *c* of the hexagonal cells, using three microstrain coefficients. The strain coefficients obtained for the $CeNi_5D_{6.3}$ are comparable to those reported for the $LaNi_5D_{6.5}$ deuteride [109]. As suggested in

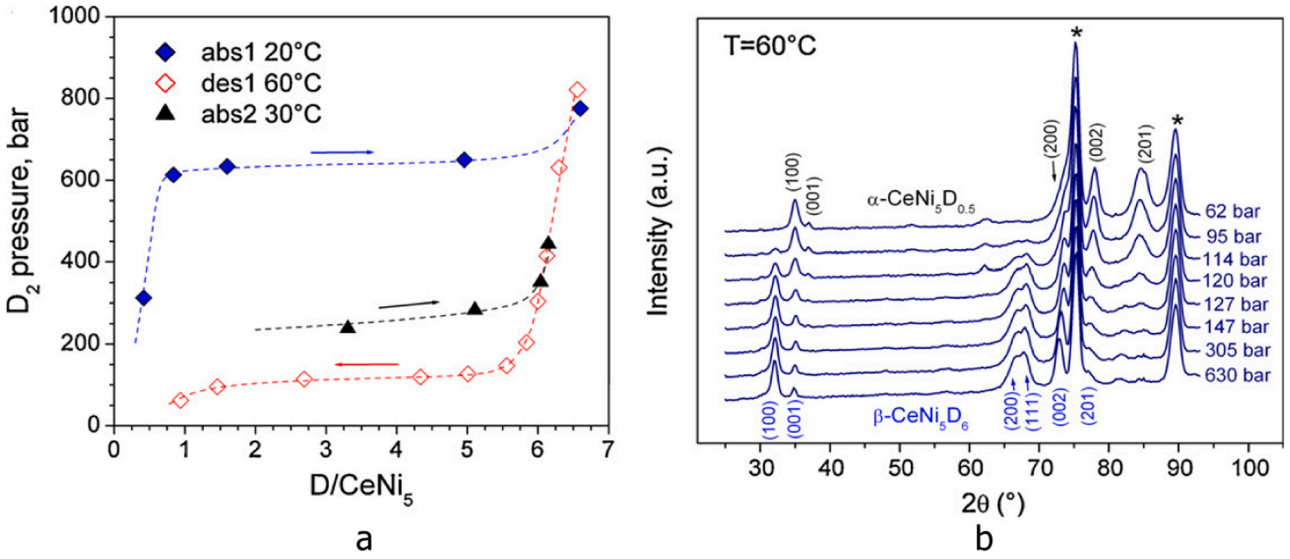

Fig. 24. (a) P–C diagrams for $CeNi_5$–D_2 system obtained by volumetric measurements during *in situ* NPD experiments; (b) evolution of NPD pattern during deuterium desorption (des1 60 ∘C) in $CeNi_5$–D_2 system. The asterisks show reflections from a stainless steel liner of the high-pressure sample cell.
(Reprinted with permission from [39]. Copyright (2010) Elsevier).

[108], a decrease in the discrete unit cell volume expansion values during the $\alpha \rightarrow \beta$ transition in the substituted $LaNi_{5-x}M_x$ (M = Co, Mn, Al, Fe, Cu, Sn) or overstochiometric $LaNi_{5+x}$ (x = 0–0.5) compounds leads to a reduction of the strain parameters. Thus, it is natural to propose a similar explanation for the $CeNi_5 \rightarrow CeNi_5D_{6.3}$ transformation; here the larger, as compared to the $LaNi_5D_{6.5}$ [108], values of the microstrain parameters developed during the deuteration of the Ce-based intermetallic are caused by significantly larger volume expansion during the deuterium absorption in $CeNi_5$.

5.2.2. $ZrFe_{1.98}Al_{0.02}$-D_2 [39]

$ZrFe_2$ intermetallic compound crystallizes with C15 ($MgCu_2$) Laves-type structure. SR XRD studies of the $ZrFe_{2-x}Al_x$ alloys with x = 0.02 and 0.04 showed that Fe substitution by Al increases the unit cell parameters from a = 7.072 Å for $ZrFe_2$ [39] to a = 7.08492(8) Å for $ZrFe_{1.98}Al_{0.02}$, a = 7.08658(7) Å for $ZrFe_{1.96}Al_{0.04}$, while the FCC crystal structure remains unchanged.

In situ hydrogenation-dehydrogenation studies demonstrated a very fast kinetics of H/D exchange in the $ZrFe_{2-x}Al_x$ hydrides caused by the introduction of aluminium instead of iron, in contrast with the $ZrFe_2$ binary Laves phase compound. This allowed a quick synthesis of the hydrogenated samples. For $ZrFe_{1.98}Al_{0.02}$ after activation by several hydrogen absorption–desorption cycles, at 1600 bar its maximum hydrogenation capacity reached 3.4 at.D/f.u. (see Fig. 26a), close to the capacity of the $ZrFe_2$ intermetallic alloy of 3.5 at.H/f.u. at 1800 bar H_2 [39]. For the NPD studies (see Fig. 26b), the absorption was performed at room temperature without preliminary activation of the as-cast samples (crushed into the particles 0.5–1 mm in size). Because of the absence of activation and cycling, and as a result of lower synthesis pressure applied, maximum reached D storage capacity was slightly lower than in the Sieverts

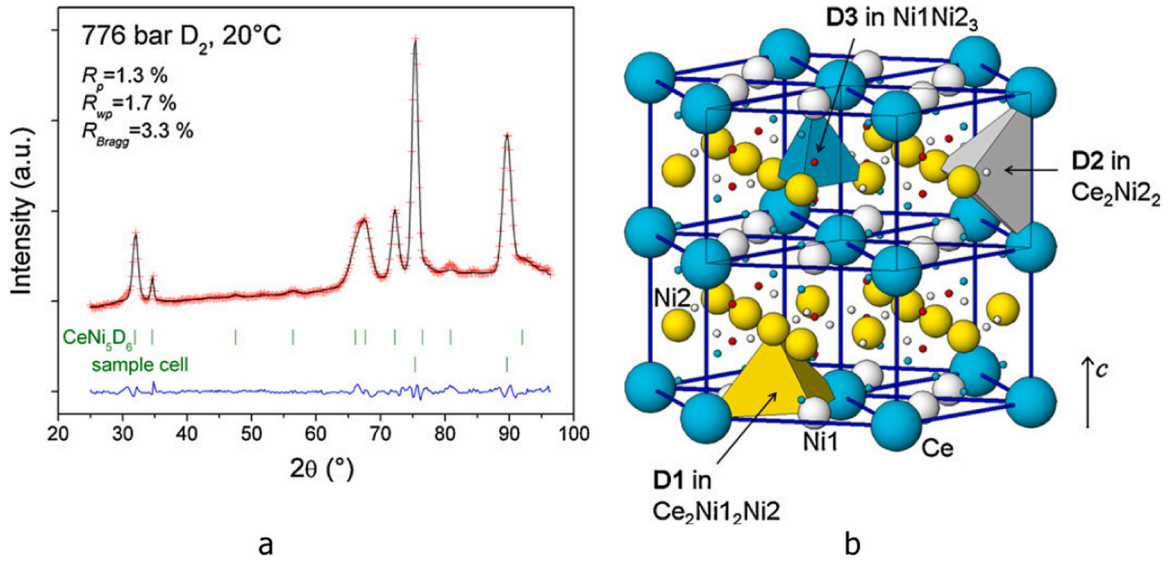

Fig. 25. (a) Refined neutron diffraction pattern for $CeNi_5D_{6.3}$ (observed (+), calculated (—) and difference (bottom line) profiles). (b) Crystal structure of the $CeNi_5D_{6.3}$ deuteride. Three types of interstices occupied by D atoms including tetrahedron Ce_2Ni_2, trigonal bipyramid Ce_2Ni_3 and tetrahedron Ni_4 are shown.
(Reprinted with permission from [39]. Copyright (2010) Elsevier).

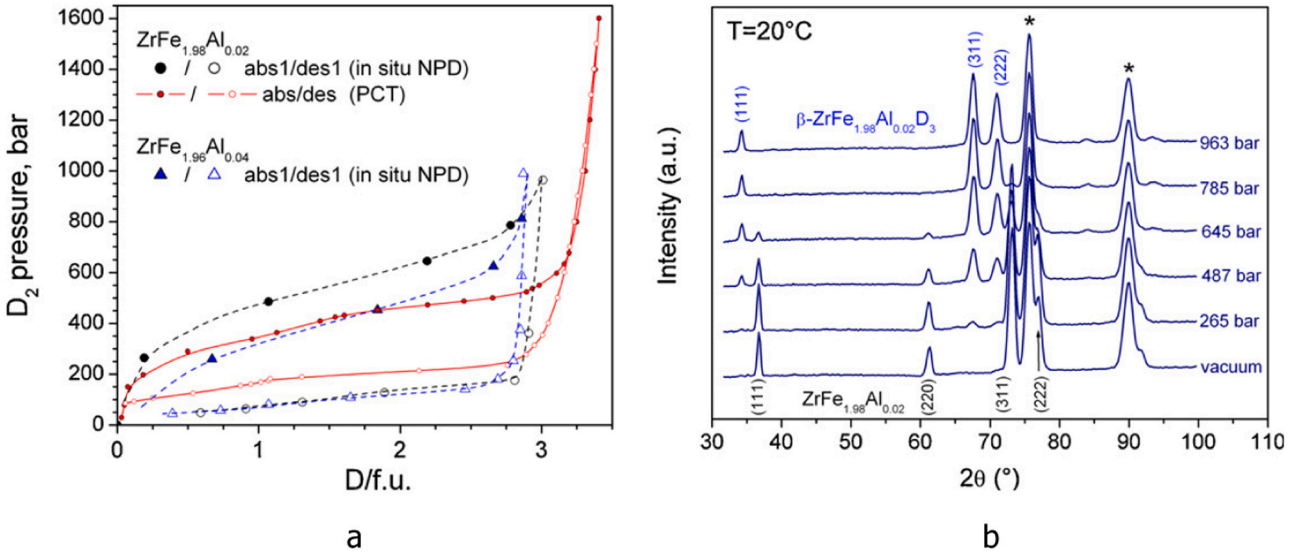

Fig. 26. (a) P–C diagrams measured at room temperature for the first D_2 absorption–desorption cycle in the $ZrFe_{2-x}Al_x$–D_2 (x = 0.02 and 0.04) systems. The data are collected by the volumetric measurements during *in situ* NPD experiments. Absorption–desorption isotherms for the activated $ZrFe_{1.98}Al_{0.02}$ were obtained during the conventional PCT measurements and are given for comparison. (b) Evolution of the NPD pattern during deuterium absorption by $ZrFe_{1.98}Al_{0.02}$. The asterisks show the peaks from the high-pressure sample cell.
(Reprinted with permission from [39]. Copyright (2010) Elsevier).

1600 bar D_2 experiment, reaching 3.0 at.D/f.u. for $ZrFe_{1.98}Al_{0.02}$ and 2.9 at.D/f.u. for $ZrFe_{1.96}Al_{0.04}$.

5.2.3. $La_{1.09}Mg_{1.91}Ni_9D_{9.5}$ and $La_{0.91}Mg_{2.09}Ni_9D_{9.4}$ [110]

Magnesium can replace 2/3 of La in $LaNi_3$ intermetallic compound to reach a limiting composition $LaMg_2Ni_9$. Two deuterated $La_{3-x}Mg_xNi_9$ samples with slightly different La/Mg ratios both only marginally deviating in a composition from $LaMg_2Ni_9$, $La_{1.09}Mg_{1.91}Ni_9$ (sample 1) and $La_{0.91}Mg_{2.09}Ni_9$ (sample 2), were studied using *in situ* neutron powder diffraction.

NPD characterisation of the $La_{1.09}Mg_{1.91}Ni_9D_{9.5}$ (1) and $La_{0.91}Mg_{2.09}Ni_9D_{9.4}$ (2) deuterides was performed at 25 bar D_2 (1) and 918 bar D_2 (2) using the setup shown in Fig. 27a. The hydrogenation properties of the (1) and (2) are dramatically different from those for $LaNi_3$. The Mg-containing intermetallics reversibly form hydrides with ΔH_{des} = 24.0 kJ/molH_2 (Fig. 27c) and an equilibrium pressure of H_2 desorption of 18 bar at 20 °C ($La_{1.09}Mg_{1.91}Ni_9$). A pronounced hysteresis of H_2 absorption and desorption, ~100 bar, is observed (Fig. 27b).

$LaNi_5$-assisted hydrogenation of $MgNi_2$ in the $LaMg_2Ni_9$ hybrid structure takes place. In the $La_{1.09}Mg_{1.91}Ni_9D_{9.5}$ (1) and $La_{0.91}Mg_{2.09}Ni_9D_{9.4}$ (2) (a = 5.263/5.212; c = 25.803/25.71 Å) D atoms are accommodated in both Laves and $CaCu_5$-type slabs (see Fig. 28a). In the $LaNi_5$ $CaCu_5$-type layer, D atoms fill three types of interstices;

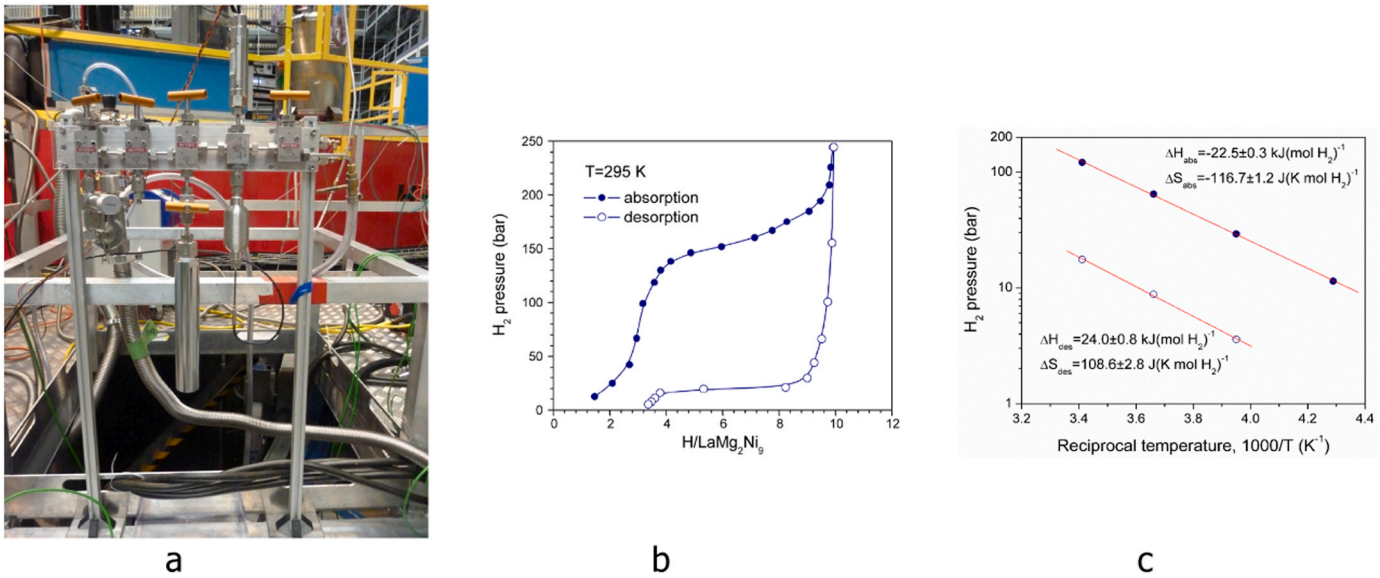

Fig. 27. (a) High pressure synthesis setup for the *in situ* NPD measurements at pressures up to 1000 bar D_2; (b) Room temperature isotherms of hydrogen absorption and desorption; van't Hoff plots (c) for $La_{1.09}Mg_{1.91}Ni_9$-based hydride. At room temperature equilibrium pressure of hydrogen absorption is ~120 bar D_2, while for the desorption $P_{eq.}$ equals to ~20 bar D_2.
(Reprinted from an open access article [110] distributed under the Creative Commons Attribution license (http://creativecommons.org/licenses/by/4.0/)).

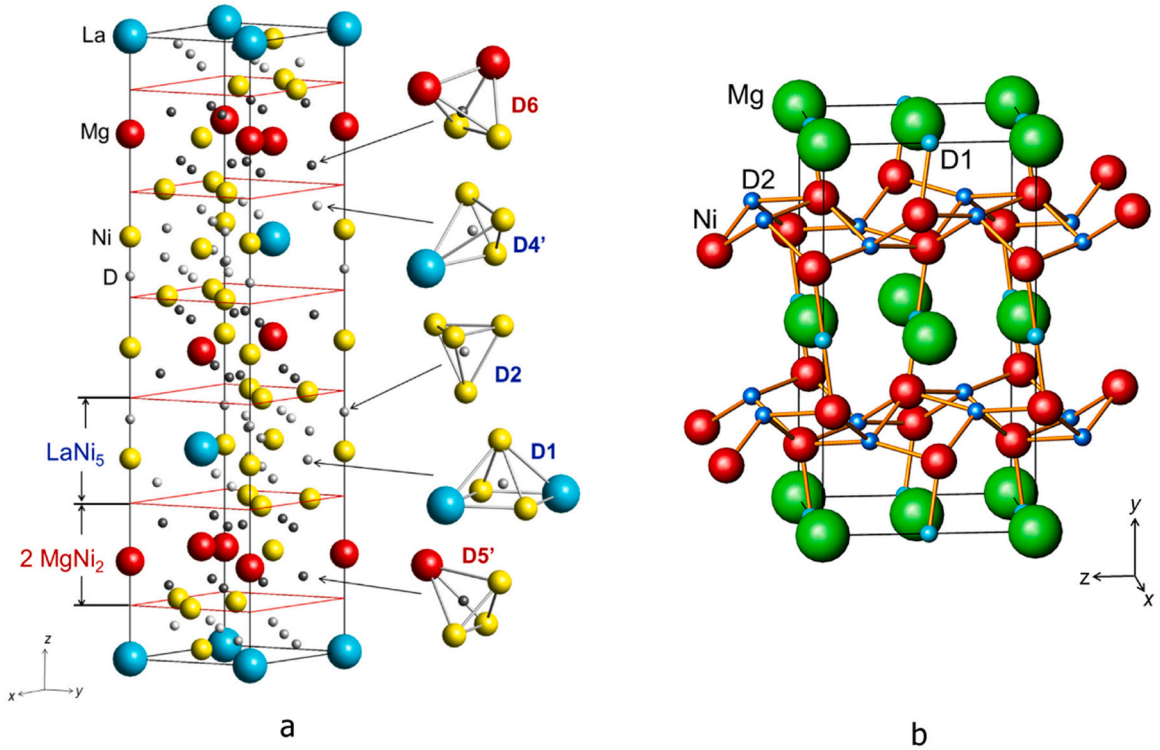

Fig. 28. (a) Crystal structure of $La_{1\pm0.1}Mg_{2\pm0.1}Ni_9D_{9.4-9.5}$ and types of the filled interstices [110]; (b) The orthorhombic *Cmca* crystal structure of $MgNi_2D_3$ [111]. Two types of sites occupied by deuterium include a Mg_4Ni_2 octahedron for H1(D1) and a chair Ni_4 configuration for H2(D2) located within the buckled Ni–H nets containing bended spirals –Ni–H2–Ni–H2–.(Reprinted from an open access article [110] distributed under the Creative Commons Attribution license (http://creativecommons.org/licenses/by/4.0/)). (Reprinted with permission from [111]. Copyright (2015) Elsevier).

a deformed octahedron $[La_2Ni_4]$, $[(La,Mg)_2Ni_2]$ and $[Ni_4]$ tetrahedra. The overall chemical compositions can be presented as $LaNi_5H_{5.6/5.0} + 2\ ^*MgNi_2H_{1.95/2.2}$ showing that the hydrogenation of the $MgNi_2$ slab proceeds at mild H_2/D_2 pressure of just 20 bar. In the $MgNi_2$ slab a partial filling by D atoms of four types of the tetrahedral interstices takes place, which include $[MgNi_3]$ and $[Mg_2Ni_2]$ tetrahedra.

$LaNi_5$-assisted hydrogenation of $MgNi_2$ is observed in the $LaMg_2Ni_9$ hybrid structure. Formation of $LaMg_2Ni_9D_{9.5}$ proceeds *via* an *isotropic* expansion of the trigonal unit cell. D atoms are accommodated in both Laves and $CaCu_5$-type slabs H atoms filling interstitial sites in both $LaNi_5$ and $MgNi_2$ structural fragments. Limits of Mg solubility in $LaNi_3$ are not confined to $LaMg_2Ni_9$ and extend to the composition $La_{0.91}Mg_{2.09}Ni_9$ with a refined composition of the $CaCu_5$-type block of $La_{0.95}Mg_{0.05}Ni_5$. Within the $LaNi_5$ $CaCu_5$-type layer, D atoms fill three types of interstices; a deformed octahedron $[La_2Ni_4]$, and two types of tetrahedra, $[LaNi_3]$ and $[Ni_4]$, to yield $LaNi_5D_{5-5.6}$ composition. D distribution is very similar to that in the individual β-$LaNi_5D_7$ deuteride.

In the $MgNi_2$ slab hydrogen atoms fill two types of tetrahedra, $[Mg_2Ni_2]$ and $[MgNi_3]$. The hydrogen sublattice formed is unique and was not observed earlier in the studied structures of the Laves-type intermetallic hydrides. These include the crystal structure of $MgNi_2D_3$ [111], [112], [113] featuring accommodation of hydrogen atoms into the Mg_2Ni_4 octahedra and nickel nets, see Fig. 28b, during the formation of which metal sublattice become rebuilt.

A significant mutual influence of the $LaNi_5$ and $MgNi_2$ slabs causes a dramatic altering of their hydrogenation behaviours leading to:

(a) significant decrease of the stability of the $LaNi_5$-type hydride;.

(b) much easier hydrogenation of the $MgNi_2$ slabs compared to the parent intermetallic compound;.

(c) increased hysteresis.

6. Dynamic transformations in the Laves type metal-hydrogen systems

6.1. AB_2-D_2 system studied at 5/10 bar D_2 in the temperature window

6.1.1. 300–473 K during the heating and cooling

AB_2 Laves type intermetallics form the most abundant group of the hydride-forming alloys which contains more than 900 binary and ternary compounds. The chemistry of these compounds is very rich as they are composed from a variety of the very different in chemical behaviours elements at the A (Mg, Ca, Ti, Zr, Rare Earth Metals) and B (V, Cr, Mn, Fe, Co, Ni, Al) sites. Recently hydrides of the Laves type intermetallics as hydrogen storage materials were reviewed in [16,114].

When the ratio between the atomic radii of the A and B components has an ideal value of $r_A/r_B = 1.225$, there structures can be presented as a close packing of different in size spheres A and B, while the structures contain A_2B_2, AB_3 and B_4 interstices present in stoichiometric ratio 12:4:1.

Broad solid solubility ranges on both A and B sites allow to optimize the performance of the hydrides – reversible storage capacity, thermodynamics and kinetics of their interaction with hydrogen and thermal stability.

One family which has been recently in focus of the research efforts can be described by a general formula $(Zr_{1-x}Ti_x)(Ni, Mn, V, Fe)_{2\pm y}$.

When the content of the components at the B site is fixed as $Ni_{1.2}Mn_{0.7}V_{0.12}Fe_{0.12}$, this allows to utilise a modification of the ratio between Zr and Ti (in a range from 88:12–78:12) and, furthermore, a ratio between B and A (between 1.90 and 2.07) to optimize thermodynamic properties of the hydrides – equilibrium pressures of hydrogen desorption and absorption. One attractive feature of the

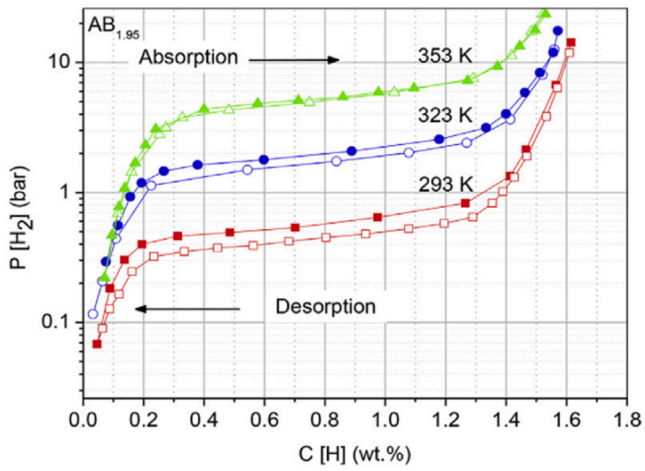

Fig. 29. Isotherms of hydrogen absorption and desorption in the $Zr_{0.80}Ti_{0.20}Ni_{1.2}Mn_{0.7}V_{0.12}Fe_{0.12}$-$H_2$ system measured at 293, 323 and 353 K.
Reprinted from an open access article [115] distributed under the Creative Commons Attribution license (http://creativecommons.org/licenses/by/4.0/).

formed hydrides with H storage capacity close to 3 at.H/f.u.$AB_{2\pm y}$ (2.9–3.2) is in a very small hysteresis between the equilibrium pressures of hydrogen absorption and desorption and presence of the flat plateaux at the isotherms of H_2 absorption and desorption, see Fig. 29. Please, note that with increasing temperature from 293 K to 353 K, the difference between the absorption and desorption branches of the isotherms decreases because the measured T become close to the critical temperature in the studied system (the differences with disappear at $T = T_{critical}$).

The high rates of hydrogen absorption and desorption steps (See Fig. 30, a and b) are jointly governed by hydrogen diffusion and grain boundary nucleation of alpha-solid solution and beta-hydride identified as a rate limiting steps by fitting the kinetic equation $X = 1\text{-}\exp(-Kt^n)$ with the values of n = 1–1.25.

In situ neutron powder diffraction patterns were measured for the deuteride sample placed into a 6 mm SS autoclave and equilibrated at 5 bar D_2 and at 10 bar D_2 in separate experiments. Then the samples were slowly heated and, later, cooled down while keeping a slow linear heating and cooling rate, so a heating experiment from 300 to 473 K lasted 4 h and 20 min. The data collection has been performed by recording individual data sets recorded every 7 min. These individual data sets were all successfully fitted by Rietveld profile refinements and gave nice fits of the data. A typical example is presented in the Figure Fig. 31a, while the Fig. 31b shows a 2-D plot of the development of the temperature-dependent development NPD pattern manifesting a reversible decomposition of the deuteride to form the initial alloy and of the rehydrogenation process.

The fitting of the NPD data allowed to reach the following conclusions. The maximum hydrogen storage capacity reached was 3.22 at.D/f.u. $AB_{1.95}$. H/D capacity is pressure-dependent and grows up when the pressure increases from 5 to 10 bar D_2. β-deuteride has a broad homogeneity range, extending between 2.45 and 3.22 at.D/$AB_{1.95}$. D content in α-solid solution within a two-phase region is appr. 0.40–0.45 at.D/f.u. $AB_{1.95}$.

The collected data allowed to build the isobar diagrams of the dependence between the deuterium content $D/AB_{1.95}$ and temperature for the system $AB_{1.95}$-D_2 studied at two setpoint pressures of deuterium, 5 and 10 bar D_2 and showed an excellent agreement (see Fig. 32) between the experimental data (red spheres – 10 bar H_2; black rectangles – 5 bar H_2) and modelled dependences when using thermodynamic constants for the $Zr_{0.80}Ti_{0.20}Ni_{1.2}Mn_{0.7}V_{0.12}Fe_{0.12}H_3$ hydride, ΔH_{des} = 35.25 kJ/mol H_2; ΔS_{des} = 113.33 J/mol H_2 K.

6.2. *Reversible deuterium loading and kinetics in MgD_2-TiD_2 nanocomposites [36]*

MgD_2 –TiD_2 nanocomposites are outstanding materials for hydrogen storage because of their high reversible capacity (> 4 wt%), fast reaction kinetics and good cycle life at atmospheric pressure and moderate temperature, typically 573 K [118,119]. They can be efficiently prepared by mechanochemistry of Mg and Ti powders under deuterium pressure [120]. For a better understanding of these properties, *in situ* neutron diffraction experiments were carried out at D1B@ILL on two representative $(1-x)MgD_2 - xTiD_2$ samples with $x = 0$ and 0.3 [36]. Simultaneous to the acquisition of neutron diffraction data, first thermodesorption (TD) from RT to 600 K and then PCI measurements at 548 K were performed. For the former, the deuterium outlet of the stainless steel sample holder was connected to a Baratron device and rotatory pump, while for the latter, a

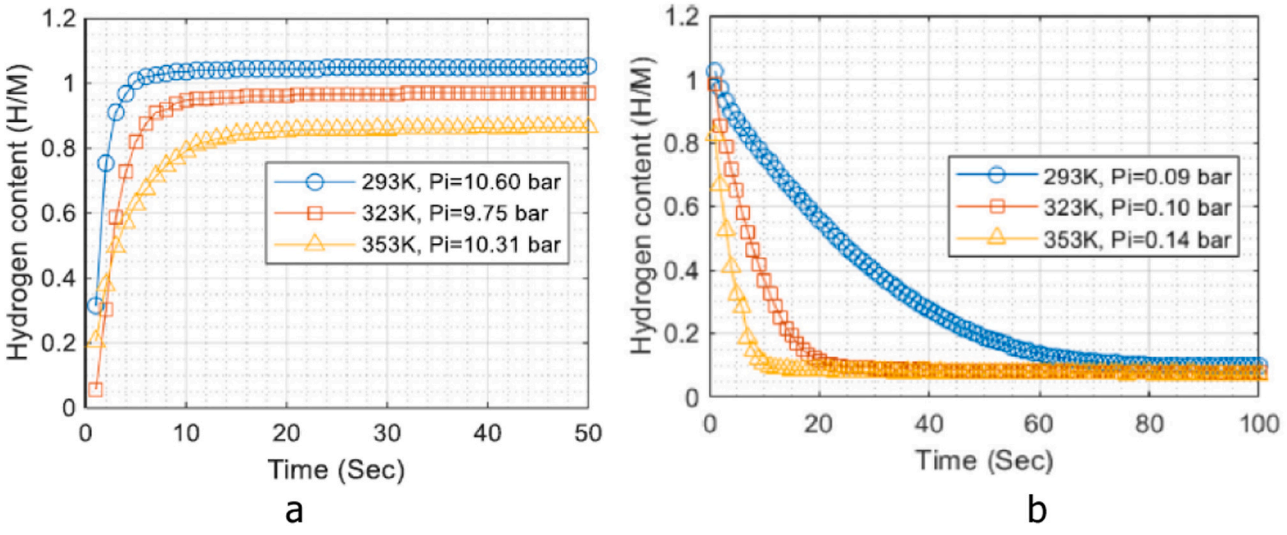

Fig. 30. Hydrogen absorption (a) and desorption (b) kinetic curves showing that at specified P/T conditions the absorption process is very fast and can be completed in just 9 s, while the desorption process is clearly slower.
Reprinted from an open access article [116] distributed under the Creative Commons Attribution license (http://creativecommons.org/licenses/by/4.0/).

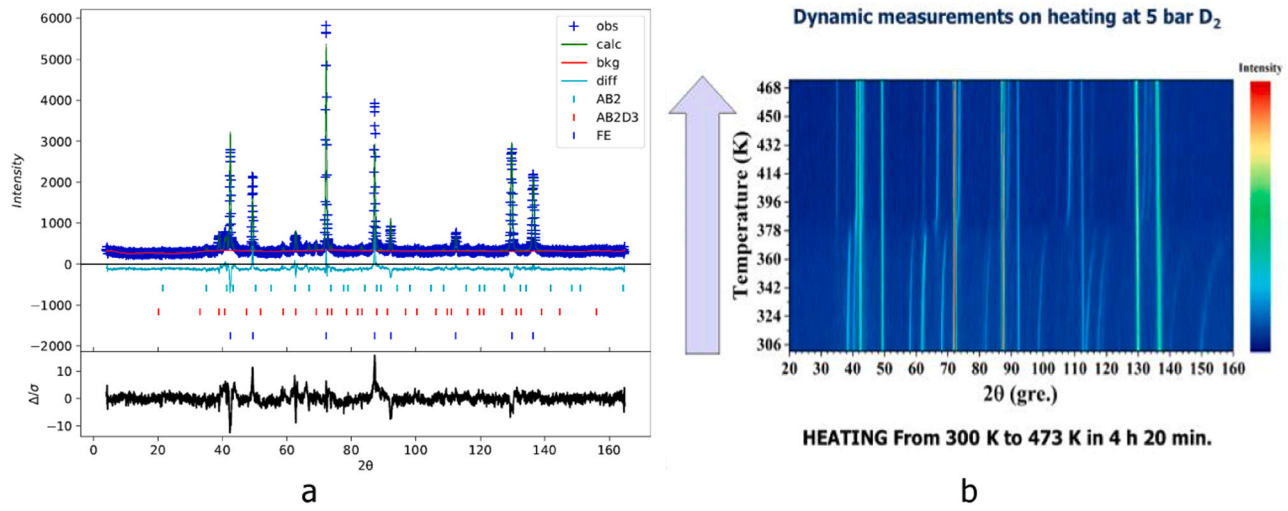

Fig. 31. (a) Refinements of an individual data set measured after equilibrating the sample at 323 K / 10 bar D_2 during the cooling experiment. Collection time of the data pattern was 7 min [117]. (b) 2-D plot of the temperature-dependent variation of the diffraction pattern measured in the T range between 300 and 473 K for the sample accommodated in a SS autoclave at 5 bar D_2 showing a transformation from the deuteride to the alloy.

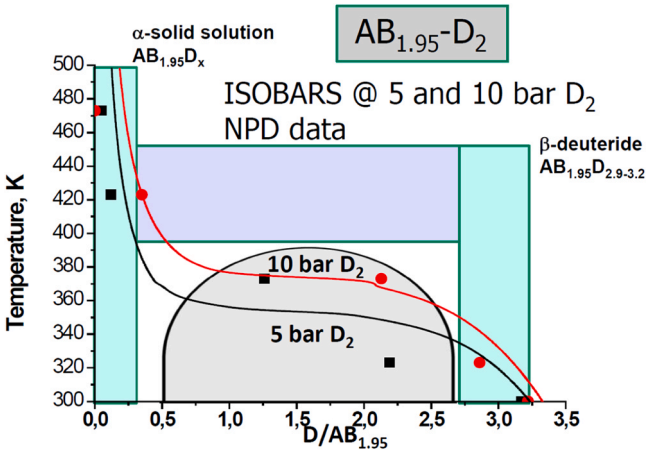

Fig. 32. Experimental data from the NPD studies of the phase-structural equilibria in the $Zr_{0.80}Ti_{0.20}Ni_{1.2}Mn_{0.7}V_{0.12}Fe_{0.12}$ – H_2 system forming a saturated hydride $AB_{1.95}H(D)_{3.2}$ [117].

Sieverts' apparatus (see Fig. 6) was connected allowing controlled deuterium uptake/release within the pressure range 0.01–1 MPa.

Fig. 33a shows the evolution the crystallite size of tetragonal β-MgD_2 (S.G. $P4_2/mnm$) and hexagonal Mg (S.G. $P6_3/mmc$) phases during TD experiments on $x = 0$ and 0.3 samples. For the Ti-free sample ($x = 0$), the Mg phase exhibits severe grain coarsening with a crystal size of 90 ± 20 nm after desorption of MgD_2 above 550 K. In contrast, in the presence of TiD_2 phase, grain coarsening of Mg crystallites is limited to 30 ± 5 nm at the same temperature. It is concluded that, following the Zener effect, TiD_2 inclusions limit the grain growth of Mg and MgD_2 phases allowing for short D-diffusion paths and, therefore, fast reaction kinetics associated to the MgD_2/Mg phase transformation and long cycle-life.

Fig. 33b shows the evolution the TiD_2 cell volume during the TD and PCI experiments for $0.7MgD_2$-$0.3TiD_2$ sample ($x = 0.3$). During TD, the TiD_2 cell volume first decreases from 88.6 to 88.2 Å^3 due to segregation of Mg out of the TiD_2 structure and then to 87.1 Å^3 due to the formation of sub-stoichiometric $TiD_{2-\eta}$. Next, during PCI experiments, variations in the range 88.1 – 88.3 Å^3 are concomitant to the Mg/MgD_2 transformation and are therefore attributed to the coherent coupling between the TiD_2 phase and Mg/MgD_2 interfaces.

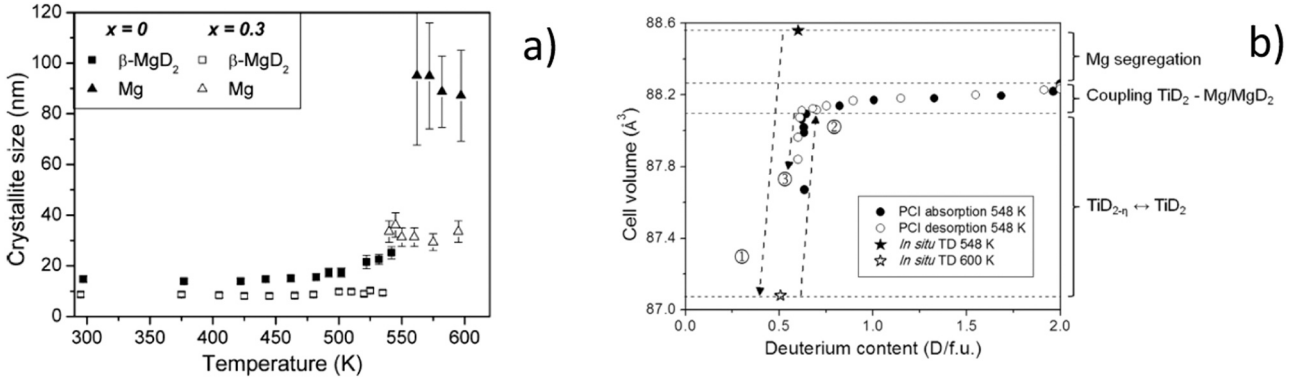

Fig. 33. (a) Evolution of the crystallite size of β-MgD_2 and Mg phases during thermal desorption (TD) of $(1-x)$ MgD_2 – $xTiD_2$ samples with $x = 0$ and 0.3. (b) Variation of TiD_2 cell volume during *in situ* TD and PCI measurements. Event ① corresponds to cell volume decrease during *in situ* TD. Events ② and ③ correspond to the cell volume variations during partial absorption and desorption of deuterium in TiD_2 phase at 548 K.
(Reprinted with permission from [36]. Copyright (2013) American Chemical Society).

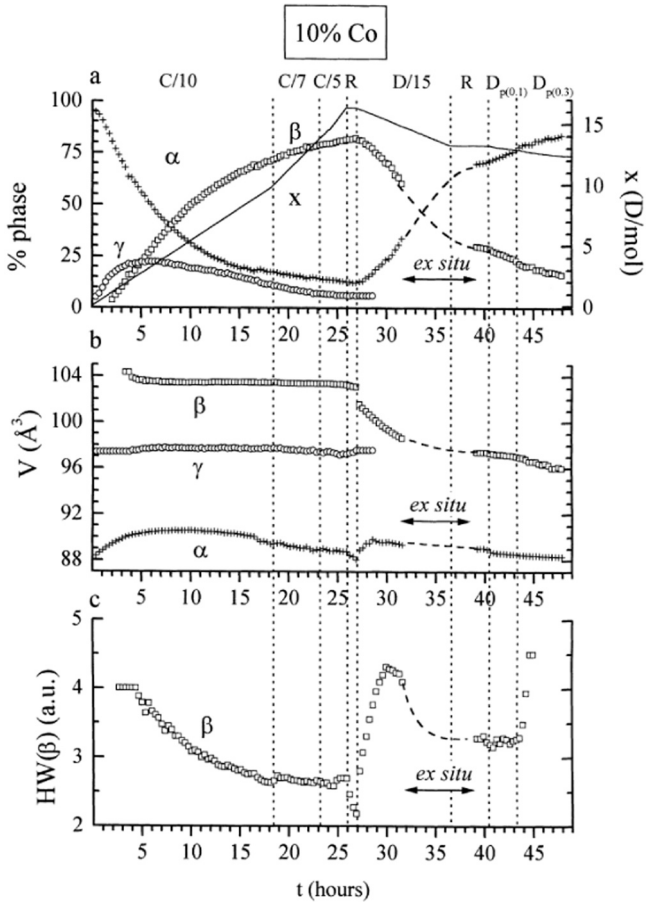

Fig. 34. (a) Electrochemical cycling of the 10 wt% Co electrode from a discharged initial state: (a) intensities of the α (+), γ (O) and *β* (□) phases (left axis) and expected capacity x (full line) determined from coulometric measurements (right axis). (b) Cell volume V of the α (+), γ (O) and *β* (□) phases. (c) Evolution of the half width of the *β* (□) phase.
(Reprinted with permission from [63]. Copyright (1999) Elsevier).

These results suggest that the TiD_2 phase facilitates H-mobility through coherent coupling between TiD_2 and Mg/MgD_2 phases and the presence of sub-stoichiometric TiD_2-η.

Hydrogen storage properties of Mg-based alloys and Mg-based composites depend upon the chemical nature of the additives. Various mechanisms of the favourable catalytic influence of the additives, structure and metallurgical state of the alloys have been uncovered during their phase-structural characterisation [66,113,121].

7. Electrochemical transformations in battery electrode materials

7.1. Metal hydride anodes

The use of metal hydrides as anode electrode materials of the Nickel-Metal Hydride batteries is the most developed application of the metal hydrides with the huge worldwide market of commercial Ni–MH batteries. Typical example is seen nowadays with the use of this technology as energy storage unit for a significant share of the hybrid electric vehicles (HEV) produced so far. Cheaper, safer and simpler than their competitor (Li ion batteries), the alkaline Ni–MH can be used to store electricity produced by renewable energies, intermittent in space and time. Several recent review papers present state-of-the-art status of the development of the electrode materials for the metal hydride anodes [122–124].

Layered intermetallics of AB_3 and A_2B_7 stoichiometries which structures can be formed *via* the stacking of the AB_5 ($CaCu_5$ type) and AB_2 (Laves type) layers when A=La and Ce; B=Ni, show a very unusual, strongly anisotropic expansion of the hexagonal/trigonal unit cells exclusively limited to the Laves type slabs associated with the formation of the special networks of Ni-H covalent bonds [74, 125–129]. Anisotropic expansion of the unit cells was also observed for the RENiIn-based hydrides (RE=La,Ce,Nd) and has been associated with a different reason – formation of strong Ni-H bonds and very short H…H separations, as short as 1.56 Å for Nd compound, where the "rule of 2 Å" is violated [76, 130–133].

Unfortunately, hydrides of layered RE-Ni intermetallics are thermodynamically unstable and are prone to the disproprtionation during their cycling in hydrogen gas. Among the materials with the highest electrochemical storage capacities are intermetallic alloys of the AB_3 and A_2B_7 types where Mg partially substituted lanthanum forming a solid solution without a change of the type of crystal structure. It appears that a partial replacement of RE metals by magnesium causes stabilisation of the metal sublattice. These materials offer 30% improvement of the electrochemical performance as compared to the initially developed AB_5 type metal hydride anodes and have been extensively studied in the recent years [52, 134–140]. At the same time, Co-containing AB_5 alloys still hold a significant share of the market.

7.1.1. $LaNi_5$-derived electrodes

$LaNi_5$-type alloys ($CaCu_5$-structure type, *P*6/*mmm* space group) are the most common active material used in the negative electrode of commercial Ni-MH batteries. The proof-of-concept of Ni-MH batteries dates back to the early 1970′s [141,142] but their commercialization was only possible from the 1990′s through the adjustment of $LaNi_5$ chemistry to the requirements of battery operation. Through suitable chemical substitutions, multi-elementary $LaNi_5$-derived alloys were developed with the aim of increasing the thermodynamic stability of hydride $LaNi_5H_6$ while mitigating alloy decrepitation and corrosion during electrochemical cycling [143].

In situ neutron diffraction experiments played a major role to characterize the electrochemical properties of the $LaNi_5$-type alloys [47,48,63]. Latroche et al. showed that single-substitution of Ni by Al, Mn or Co decreases the equilibrium plateau pressure and, moreover, that the cycle-life improves when the width of the *β*-hydride solution branch increases at the expense of the α + *β* plateau region [47]. The latter effect was assigned to a reduction of decrepitation phenomena, which was greatly observed in multi-substituted compounds such as $LaNi_{3.55}Mn_{0.4}Al_{0.3}Co_{0.75}$ alloy.

This concept was latter better understood in a subsequent manuscript devoted to the influence of cobalt content in $MmNi_{4.3-x}Mn_{0.3}Al_{0.4}Co_x$ alloy. Two alloys with cobalt content of 5 and 10 wt% (x = 0.36 and 0.69, respectively) were analyzed [63]. Alloy pulverization significantly decreased with cobalt content. *In situ* neutron diffraction patterns were monitored for the 10 wt% Co sample $La_{0.51}Ce_{0.24}Nd_{0.23}Pr_{0.02}Ni_{3.61}Mn_{0.30}Al_{0.39}Co_{0.69}$ during a charging /discharging cycle with different regimes (Fig. 34a). The refinement of diffraction patterns required to consider a novel intermediate phase, denoted as γ, in addition to classical α-intermetallic and *β*-hydride. This phase has a cell volume between that of α and β phases while keeping same space group (Fig. 34b), while the halfwidth parameters of the β phase changed (Fig. 34c). The γ phase is metastable and is only observed during the charge step, as shown in Fig. 35. The occurrence of this intermediate deuteride implies a two-step process in the α to β transformation and it allows the system to reduce the strains induced by the large volume expansion during phase transition. As a consequence, the decrepitation process and subsequent corrosion effects were mitigated.

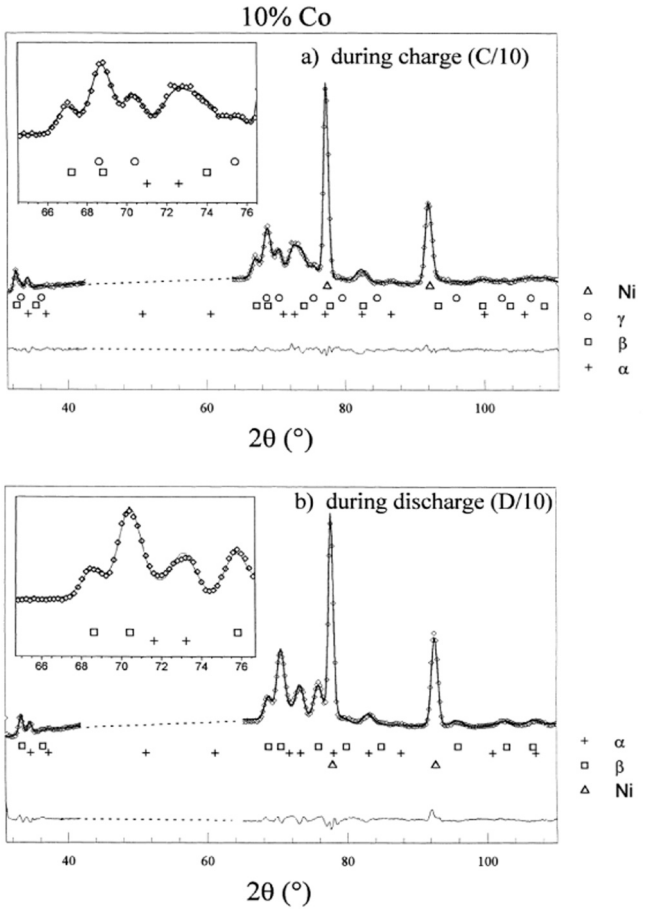

Fig. 35. Refined neutron diffraction pattern of MmNi$_{3.61}$Mn$_{0.3}$Al$_{0.4}$Co$_{0.69}$ (10 wt% Co) alloy. (a) After 9 h of charge at *C*/ 10, (b) after 5 h of discharge at *D*/15, showing the experimental, calculated and difference curves. The inset shows the detailed contribution between 64 < 2θ < 78 involving three phases during the charge and only two phases for the discharge. Ni lines come from both the collector grid and the counter electrode.
(Reprinted with permission from [63]. Copyright (1999) Elsevier).

Further studies by *in situ* neutron diffraction demonstrated that the occurrence of the intermediate γ phase depends not only on the Co content but also on the mischmetal composition and the alloy stoichiometry, *i.e.* the atomic ratio between the transition metals *B* and the rare earths *A* [49]. Thus, the probability of the appearance of the γ phase decreases with cobalt content but increases with AB$_{5+y}$ over-stoichiometry (*y*). Owing to the high cost of cobalt as compared to other transition metals, intensive research was conducted to reduce its content without impacting the cycle-life. This was achieved by optimizing the alloy stoichiometry, which results in the shrinking of the α + β plateau region [35]. Moreover, by replacing Co by Fe, the formation of intermediate γ- phase is favoured and long cycle-life achieved. Indeed, the cycle-life of the Co-free and overstoichiometric AB$_{5.3}$ compound La$_{0.70}$Ce$_{0.22}$Nd$_{0.06}$Pr$_{0.01}$Ni$_{4.07}$Mn$_{0.64}$Al$_{0.19}$Fe$_{0.42}$ is reported to be comparable to that of equivalent Co-containing compound [50].

In situ neutron diffraction studies have been conducted in LaNi$_5$-type electrodes for determining also kinetic mechanisms. Reaction kinetics of an AB$_5$-type electrode of composition La$_{0.50}$Ce$_{0.35}$Nd$_{0.12}$Pr$_{0.03}$Ni$_{3.60}$Al$_{0.30}$Mn$_{0.40}$Co$_{0.70}$ at high charge / discharge rates (regime over 2 C, 700 mA/g) have been analysed by Latroche et al. [45]. The active material was pulverised by solid-gas hydrogenation cycling and was afterwards surface-treated by hot-alkali etching to ensure high catalytic activity. By using high neutron flux at D20/ILL beamline and the large position sensitive detector, they succeeded to analyse its reaction kinetics during full absorption/desorption in 1 h (Fig. 36). At such high reaction rates, out of equilibrium states were observed simultaneously in the α-intermetallic and β-hydride phases showing that the rate limiting factor of electrode charging/discharging is the α/β phase transformation not the deuterium diffusion coefficient within any of these phases.

7.1.2. Mg-containing $RE_{3-x}Mg_xNi_9$ – D_2 systems

LaNi$_5$-type anode materials are effective, but their intrinsic capacity is restricted to 300 mAh*g^{-1}. To improve the energy density, it is necessary to introduce new materials with larger H storage and electrochemical capacity. One approach is to use layered structure phases. These structures are built by stacking along the *c*-axis different subunits with compositions AB$_5$ and AB$_2$ (A: rare earths and B: transition metals). By adding different slabs as mAB$_5$ + 2AB$_2$, various stoichiometries of the general A-B phase diagram can be described such as AB$_3$ (m=1), A$_2$B$_7$ (m=2), and A$_5$B$_{19}$ (m=3). Costly rare-earths can be partially replaced by additions of magnesium leading to pseudo-binary or ternary systems A-Mg-B. Mg substitution has been demonstrated to be effective as it enables a lower molar mass, enhances the structural stability, and stabilizes the equilibrium pressure as well as reducing the overall cost.

7.1.2.1. La_2MgNi_9 anode. The electrochemical behaviour of a composite electrode made of La$_2$MgNi$_9$ has been thoroughly investigated by *in situ* neutron powder diffraction using deuterated samples at different charge/discharge rates. From the data analysis, combining diffraction and PCT measurements (see Fig. 37, a, b, c), the mechanisms and the kinetic of the electrode performance have been determined. A fairly good agreement is observed between the solid-gas and electrochemical capacities (see Fig. 37a). The electrode material works by following a hydride to intermetallic transformation through a *beta* solid solution domain and a *beta* to *alpha* transformation with low capacity attributed to the *alpha* solid solution domain. During charge, heavy line broadening is however observed and might be related to the formation of an intermediate *gamma* phase as previously observed in the LaNi$_5$ systems. The electrochemical reaction easily follows the current variations at all rates indicating absence of kinetic limitations for the hydrogen exchange in the materials when the charge-discharge rates C/10 and C/5 are applied.

However, for the studied bulky electrode, part of the reversible capacity is lost because of (a) formation of electrochemically stable α H solid solution which contains up to 1 at. H/f.u. and (b) incompleteness of the conversion of the metal hydride anode electrode alloy into the *beta* hydride phase during the charging process. Thus, care should be taken to achieve efficient performance of the metal hydride electrodes on their scaling up [52].

7.1.2.2. $LaNdMgNi_9$ anode. LaNdMgNi$_9$ intermetallic alloy crystallizes with a rhombohedral PuNi$_3$ type structure and has slightly smaller unit cell parameters as compared to La$_2$MgNi$_9$. The partial replacement of La by Nd induces a volume contraction of 1.2% for the metallic lattice. LaNdMgNi$_9$ displays a single pressure plateau in the PCT isotherm measured at 293 K, with a desorption pressure around 0.03 MPa H$_2$ and a maximum storage capacity close to 12.9 at. H/f.u. (see Fig. 38a).(Fig. 39).

The presence of Nd in the La$_{2-y}$Nd$_y$MgNi$_9$ alloys results in the appearance of more flat and longer plateaux, both in the case of hydrogen absorption-desorption and under electrochemical charge-discharge processes. Furthermore, increased Nd substitution for La in La$_2$MgNi$_9$ promotes the formation of a more homogeneous alloy and increases the high rate dischargeability (HRD) of the electrode. The electrochemically charged alloy showed a hydrogen storage capacity of 9.8 D/f.u, 23% lower as compared to the deuteride obtained by solid-gas route at 1.6 MPa of deuterium pressure (12.9 D/f.u.). NPD studies of the saturated deuteride revealed a nonuniform

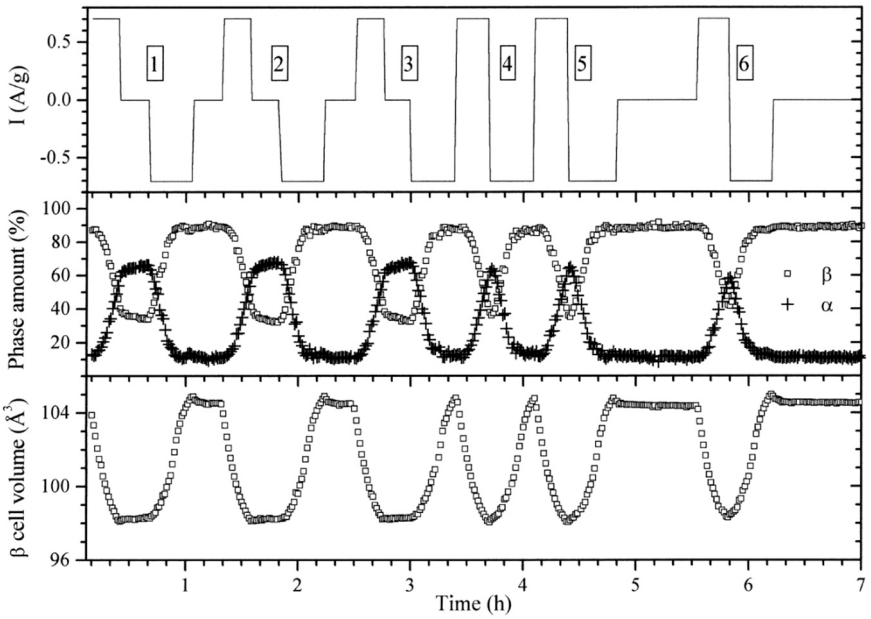

Fig. 36. Current density (top), phase amount (middle) and β-phase cell volume during galvanostatic cycling at high rate (700 mA/g) of surface-treated $La_{0.50}Ce_{0.35}Nd_{0.12}Pr_{0.03}Ni_{3.60}Al_{0.30}Mn_{0.40}Co_{0.70}$ electrode.
(Reprinted with permission from [45]. Copyright (2002) Elsevier).

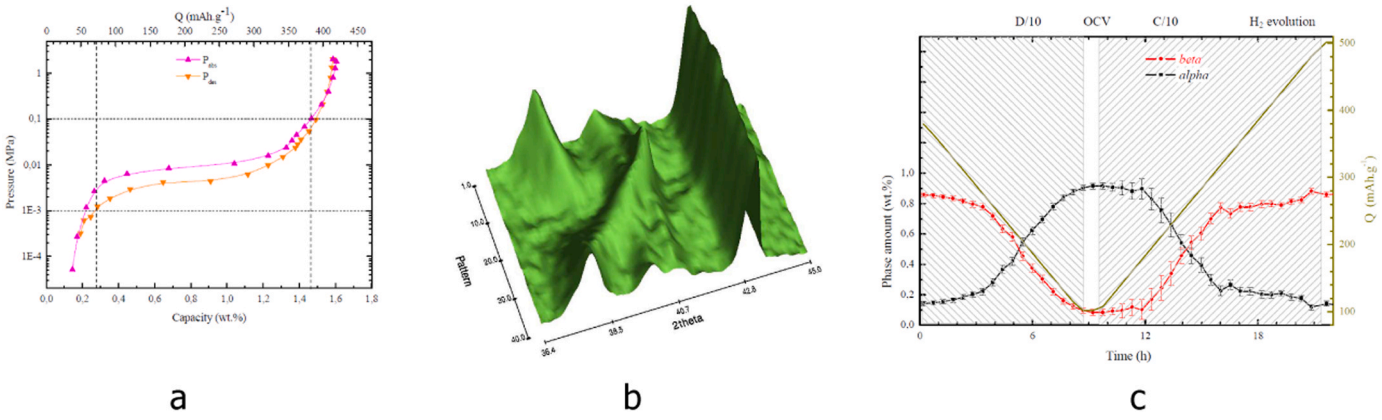

Fig. 37. (a) Pressure-Composition-Temperature (PCT) isotherm curve for La_2MgNi_9 during a full absorption/desorption cycle at 20 °C. The dotted lines stand for the electrochemical window (between 0.001 and 0.1 MPa) and define about 310 mAh·g^{-1} of reversible capacity (data from [52]) whereas the total capacity at 0.1 MPa reaches 380 mAh g^{-1}; (b) 3D view of the NPD pattern evolution as function of time during the first cycle (D/10 +C/10) of the working electrode at a current rate of 33 mA.g^{-1}; (c) Comparison between the *alpha* and *beta* phase amounts and the capacity Q during the in-beam charge/discharge cycle at D/10 +C/10 for the working electrode. The initial charge state Q at t = 0 is set at 380 mAh.g^{-1}, a value determined from the PCT curve (Fig. 39a) at a pressure of 0.1 MPa.
(Reprinted with permission from [52]. Copyright (2014) American Chemical Society).

distribution of D atoms within the *RE*$MgNi_4$ and *RE*Ni_5 layers and filling by D atoms of 7 types of interstitial sites (Fig. 38b,c). During the electrochemical cycling (Fig. 39a), formation of an extended α-solid solution spanning from $LaNdMgNi_9D_{0.8}$ to $LaNdMgNi_9D_{1.6}$ was observed, whereas the homogeneity range for the *β*-deuteride occurred between $LaNdMgNi_9D_{8.2}$ and $LaNdMgNi_9D_{9.8}$. The reversible cycling was accompanied by the discrete transformation between α and *β* phases (Fig. 39b). The same reaction pathway was observed during the charge and discharge yielding a completely reversible cycling of the metal hydride electrode. A fully discharged state (*i.e.*, 100% of the hydrogen-free intermetallic alloy) was not reached and the amount of electrochemically released hydrogen was significantly smaller than for the metal-gas PCT measurement.

Comparison of the properties of the hydride materials containing a variable amount of Nd and increasing in a raw La_2MgNi_9-$La_{1.5}Nd_{0.5}MgNi_9$-$LaNdMgNi_9$-Nd_2MgNi_9, showed that presence of Nd is important to improve the anode electrodes of the RE_2MgNi_9 type and shows their clear advantages (broader and flatter plateaus, faster H exchange rates, better cycle stability and high-rate discharge performance) over the Nd-free compositions. Optimization of the Nd content in the $La_{2-y}Nd_yMgNi_9$ alloys will help in achieving the most efficient performance of the electrodes working in a high power regime [144].

7.1.3. *TiNi-D_2 based systems*

As rare earths are critical raw materials [145], their replacement in the negative electrodes of the commercial Ni-MH batteries would be a great success. Among all rare-earth free hydride forming alloys, *AB*-type compounds are of particular interest as they can be formed by light and relatively cheap metals. TiFe, one of the most popular hydrogen stores, forms $TiFeH_2$ with a hydrogen capacity of 1.87 wt% near standard conditions of pressure and temperature [104]. It would be a good candidate as negative electrode. But, unfortunately, it exhibits no electrochemical activity due to passivation issues. In

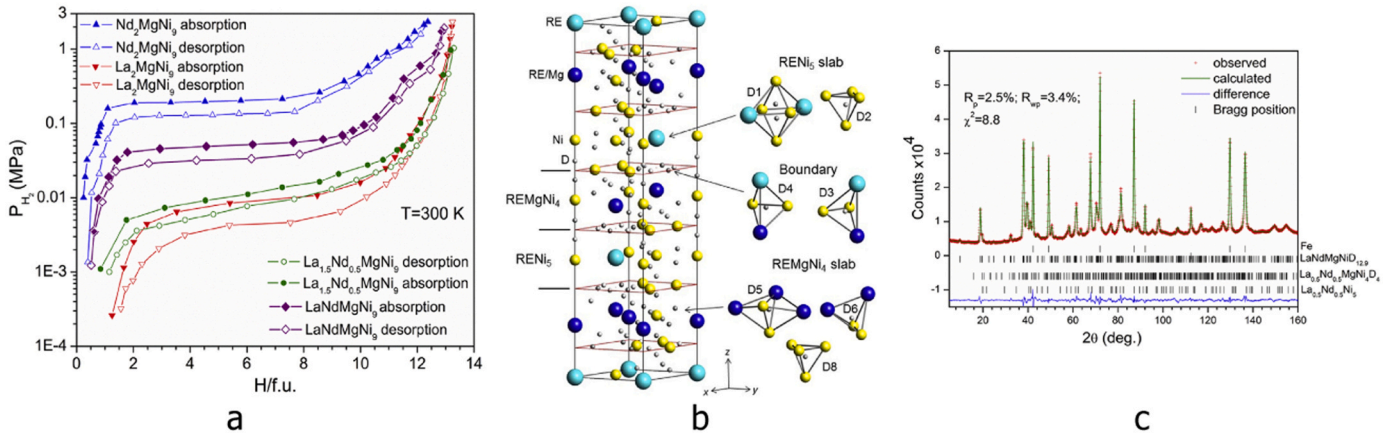

Fig. 38. (a) PCT isotherms measured for the $LaNdMgNi_9$-H_2 system at 300 K [144] as compared to the reference data for La_2MgNi_9-H_2 [134], Nd_2MgNi_9-H_2 [135] and $La_{1.5}Nd_{0.5}MgNi_9$-H_2 [138] systems; (b) Crystal structure of $LaNdMgNi_9D_{12.9}$ showing the stacking of the (La,Nd)Ni_5 and (La,Nd,Mg)Ni_4 slabs. La and Nd are labelled as RE (rare earth metals). From 7 sites filled by D, two are located inside the (La/Nd)Ni_5 layer (D1, D2), three inside the (La/Nd)$MgNi_4$ layer (D5, D6, D8), and two at the boundary between the two slabs (D3, D4). The vacant D7 site is not shown. (c) Rietveld refinements of the NPD pattern of $LaNdMgNi_9$ alloy saturated with deuterium. Wavelength used for NPD - λ = 1.494 Å. The pattern show presence of three identified phase constituents, including $LaNdMgNi_9D_{12.9}$ - 91.3(2) wt%, $La_{0.5}Nd_{0.5}MgNi_4D_4$ - 6.0(2) wt%, $La_{0.5}Nd_{0.5}Ni_5$ - 2.7(2) wt% and a stainless steel sample holder (Fe).
(Reprinted with permission from [144]. Copyright (2017) Elsevier).

contrast, TiNi has an excellent electrocatalytic activity and limited corrosion in KOH-concentrated alkali media [146]. Indeed, TiNi-based electrodes were first proposed as active materials for Ni-MH batteries. The major handicap of TiNi is however its low reversible capacity, 150 mAh/g, which corresponds to an exchange of 0.6 H atoms per TiNi formula unit [147]. This amount is much lower than for the fully hydrogenated hydride $TiNiH_{1.4}$, which suggests that some hydrogen is irreversibly trapped in the alloy during electrochemical cycling.

To improve the properties of TiNi electrodes, different chemical substitutions have been studied: Zr for Ti as well as Pd, Co and Cu for Ni [51, 147–149]. The best electrochemical properties have been obtained so far with Cu substitution for which the reversible capacity is doubled for $TiNi_{0.8}Cu_{0.2}$ alloy compared to binary TiNi [51]. As now detailed, *in situ* neutron diffraction studies coupled to galvanostatic electrochemical cycling for TiNi and $TiNi_{0.8}Cu_{0.2}$ shed light on the origin of this remarkable result [51].

For binary TiNi, the electrode was charged at C/10 rate for 12 h, relaxed for 1.5 h in open circuit, and discharged at D/10 rate up to the cut-off potential of 0.5 V *versus* $Cd/Cd(OH)_2$. The 2D diffraction patterns displayed in Fig. 40a show that the diffraction peaks referring to the pristine α-B19′ martensitic phase of TiNi (S.G. $P2_1/m$) gradually disappear on charge while those belonging to *β*-hydride (S.G. $I4/mmm$) emerge and steadily shift to lower angles. Thus, diffraction patterns reflect first the α to β phase transformation followed by a solid solution of hydrogen from β_{min} ($TiNiH_{1.0\pm0.1}$) to β_{max} ($TiNiH_{1.3\pm0.1}$) in the hydride phase. On discharge, diffraction peaks from β-hydride shift back to higher angles evidencing hydrogen release within the hydride phase. In addition, approaching to the cut-off potential, a novel diffraction peak starts appearing attributed to

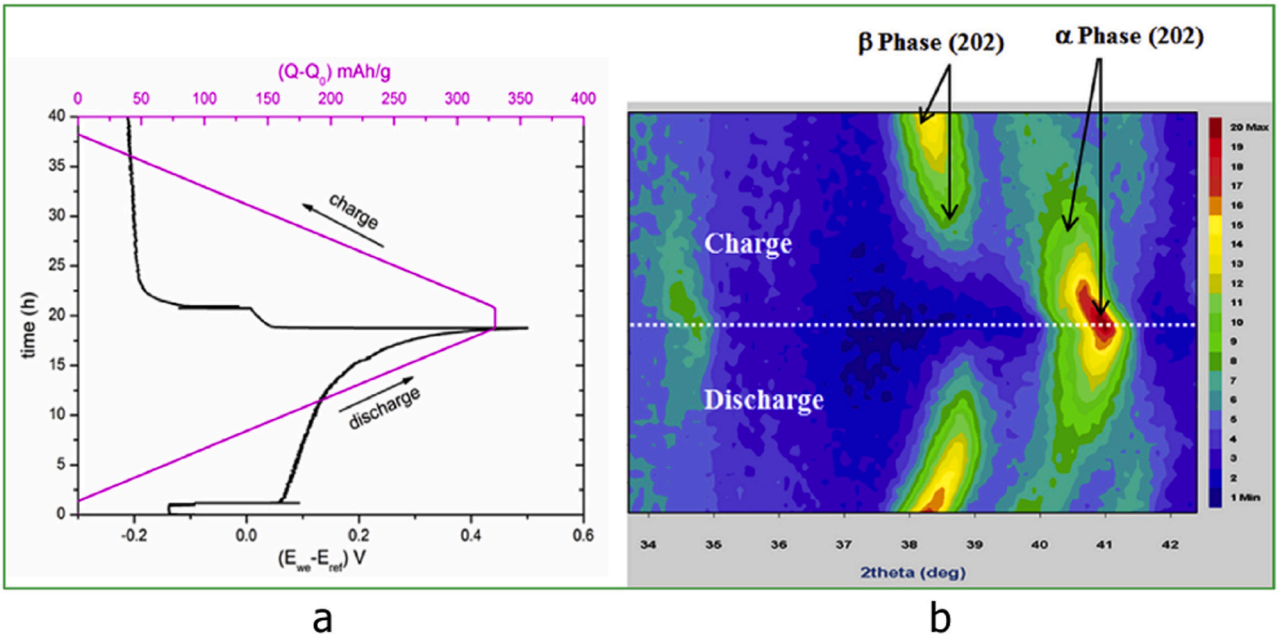

Fig. 39. (a) Discharge/charge potential profile and electrochemical capacity for the $LaNdMgNi_9$ electrode. (b) 2D contour plot of NPD patterns within the angular domain 34° < 2θ < 42° showing the evolution of (202) diffraction lines of α-metal and *β*-deuteride phases during the galvanostatic cycling.
(Reprinted with permission from [144]. Copyright (2017) Elsevier).

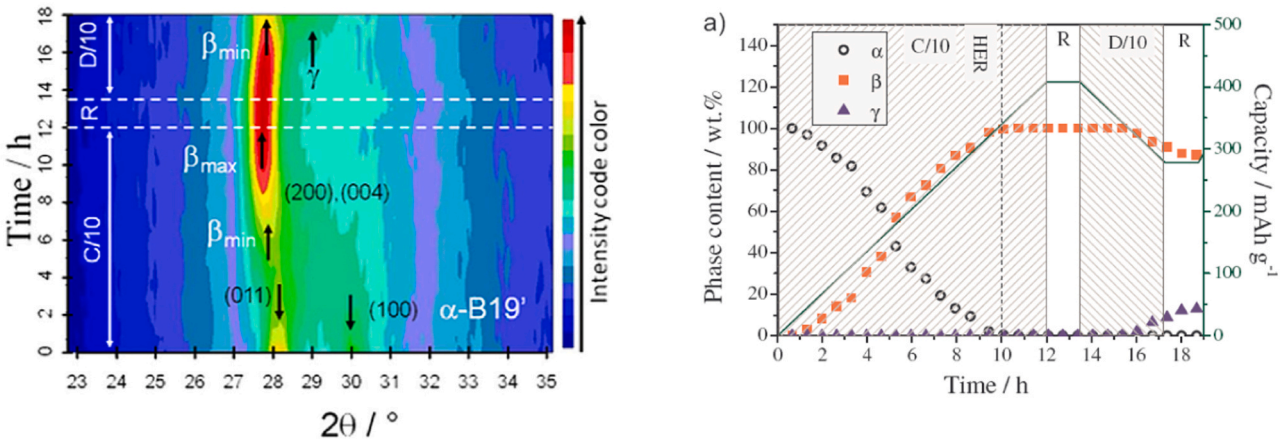

Fig. 40. (a) First charge/discharge cycle of TiNi electrode 3D. 2D view of the neutron diffraction pattern evolution as function of time; (b) phase amount as a function of time . (Reprinted with permission from [51]. Copyright (2014) Elsevier).

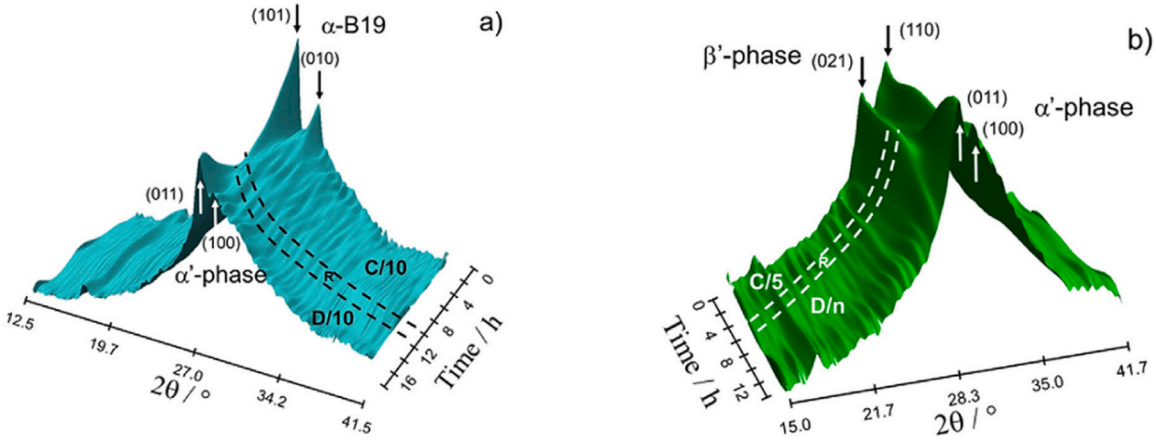

Fig. 41. 3D *in situ* neutron diffraction patterns of $TiNi_{0.8}Cu_{0.2}$ electrode. (a) First charge/discharge cycle; (b) Fourth galvanostatic cycle. Phase identification and indexation of main peaks are given.
(Reprinted with permission from [51]. Copyright (2014) Elsevier).

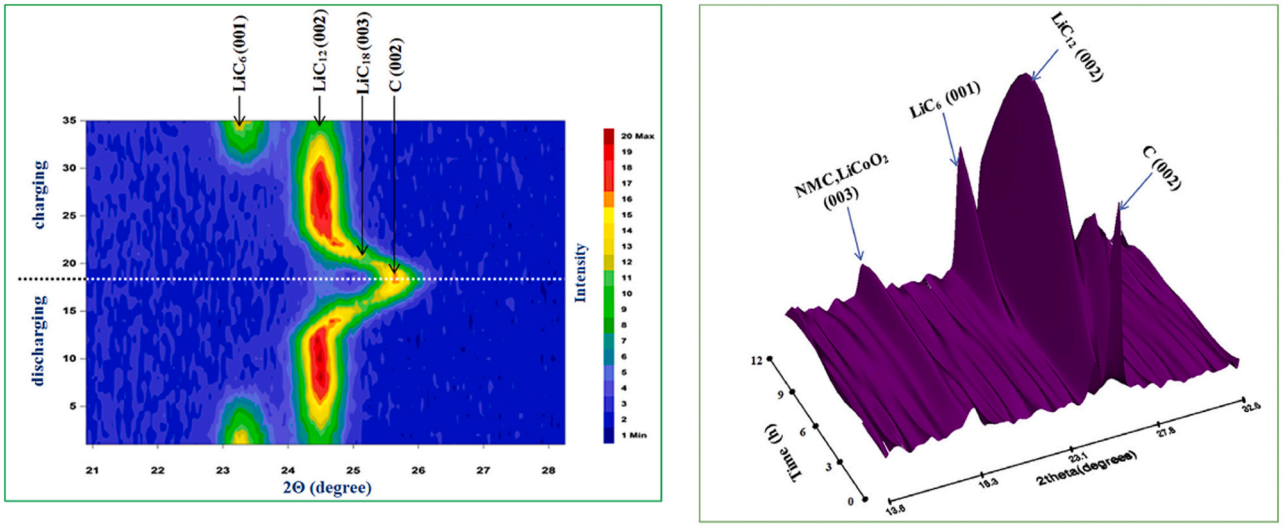

Fig. 42. (a) 2D-plot of a selected area of the *in situ* ND pattern of anode during a discharge-charge cycle. The color scale (right axis) represents the diffraction peaks intensities (red: the highest intensity; blue - the lowest intensity). (b) 3D plot of the *in situ* NPD pattern during the charging of the battery. A parallel development of the (003) Bragg peak of the $LiCoO_2$ and $Li(Ni,Mn,Co)O_2$, together with graphite (002), LiC_{12} (002) and LiC_6 (001) peaks is shown.
(Reprinted with permission from [150]. Copyright (2016) Elsevier).

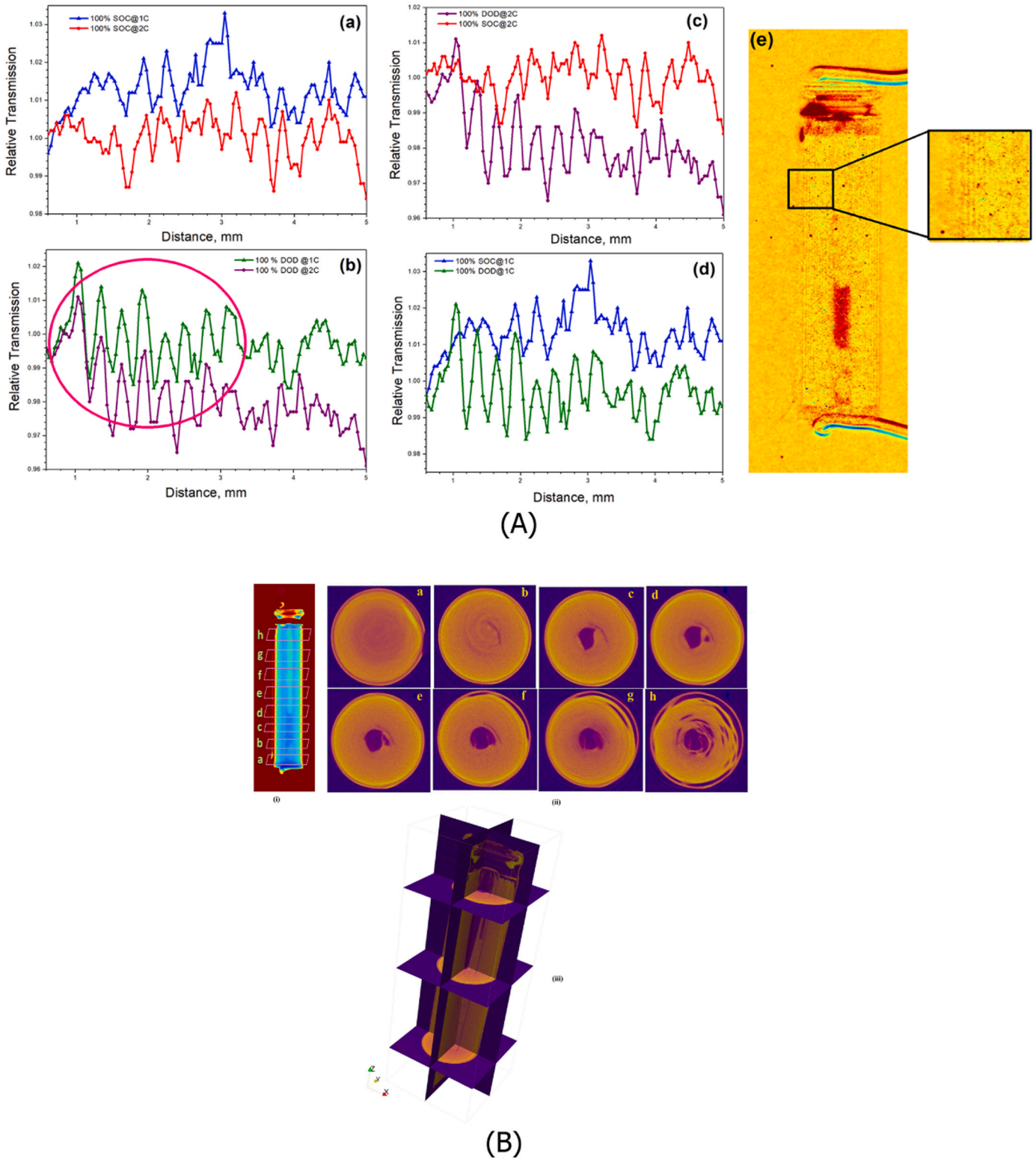

Fig. 43. (a) Comparison of fully charged states at 1 C and 2 C; (b) Comparison of fully discharged states at 1 C and 2 C; (c) Comparison of fully charged and fully discharged states at 2 C; (d) Comparison of fully charged and fully discharged states at 1 C; (e) Radiographic image of the discharged battery normalized to fully charged state and details of the area vertically averaged and depicted in (a–d). (b) Tomography slices from 3D reconstructions (ii) at different heights of the battery marked in the radiograph (i) and (iii) 3D visualization of the commercial ICR 10440 Li-ion cell (fully charged), reconstructed from the tomographic slices acquired with a total of 300 projections with 90 s exposure time. Reprinted from an open access article [151]. Distributed under the Creative Commons Attribution license (http://creativecommons.org/licenses/by/4.0/).

the formation of a minor amount of a novel γ-phase, the structure of which could not be determined. The evolution of phase contents during the whole cycle is shown in Fig. 40b. The reversible capacity for this cycle attains 130 mAh/g, being most of it provided by the hydrogen solid solution in β-hydride and, to a much lower extent, by incomplete transformation (~ 10%) between β and γ-phases.

For $TiNi_{0.8}Cu_{0.2}$ electrode, structural transformations were observed to change on cycling (Fig. 41a,b). On the first charge at C/10

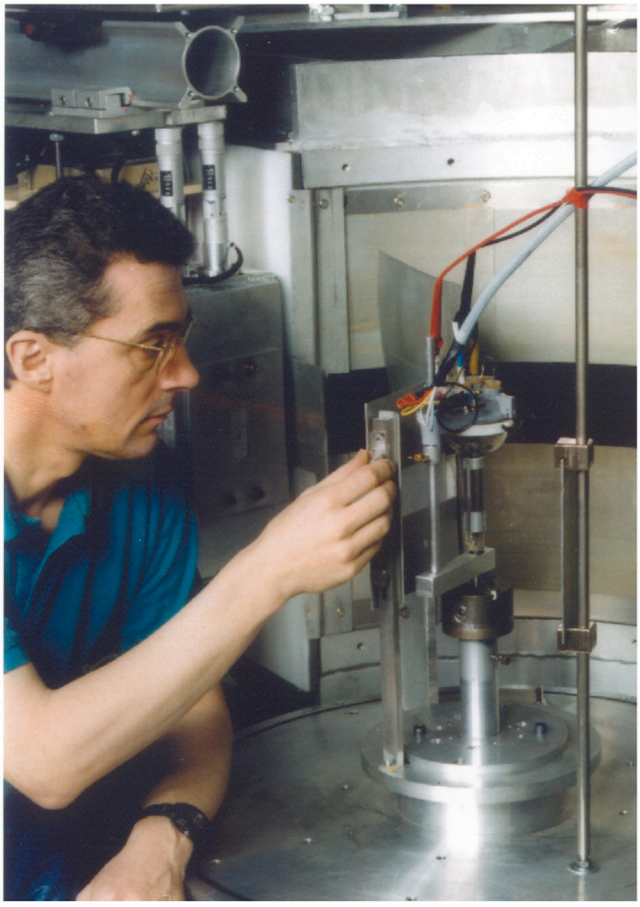

Fig. 44. Michel Latroche during the experiments with metal hydride anodes performed at D20, ILL in 1998.

regime, α-B19 martensitic phase (S.G. *Pmmb*) undergoes a phase transformation to a poorly crystallized phase. Then, on discharge at 10 D regime, a novel intermetallic phase α' (S.G. $P2_1/m$) with structure similar to B19′ martensitic phase is formed. The reversible capacity for this first cycle attained 235 mAh/g. Later, the capacity of the electrode increased up to the fourth cycle due to an activation process. A 3D-diffraction plot of neutron diffraction pattern for the four cycle is shown in Fig. 41b. At this cycle, a reversible two-phase transformation occurs between the intermetallic phase α' (S.G. $P2_1/m$) and a hydride phase β' which structure could not be fully resolved. The reversible capacity for this two-phase transformation attained as much as 330 mAh/g.

To summarize, *in situ* neutron diffraction studies demonstrated that the low reversible electrochemical capacity in TiNi mainly originates from hydrogen stored in β-hydride solid-solution. In contrast, the high electrochemical capacity of $TiNi_{0.8}Cu_{0.2}$ originates from a two-phase transformation between intermetallic and hydride phases. Complementary PCT thermodynamic studies on pseudobinary $TiNi_{1-x}Cu_x$ ($0 \le x \le 0.5$) alloys showed that the change of the reaction mechanism with Cu substitution results from Cu-induced destabilization of β-hydride [51].

7.2. Lithium ion batteries studied in situ by neutron diffraction, neutron radiography and tomography [150,151]

The structural evolution of the electrode materials in an ICR 10440 commercial cylindrical lithium-ion battery, which has a discharge capacity of 360 mAh and a nominal voltage of 3.7 V has been studied using *in situ* neutron diffraction. A three-phase mixture of Li(Ni,Mn,Co)O_2, $LiCoO_2$ and $LiMn_2O_4$ was identified as the active material of the cathode, with graphite acting as the anode material. The study revealed that the graphite anode underwent structural changes to form a series of insertion-type lithiated derivatives, with up to 12.7% volume expansion for the Li-saturated compound LiC_6 (see Fig. 42a). The charge-discharge behaviour was more complex for the cathode. Here, the charge process was associated with partial lithium depletion from the initially Li-saturated compounds, leading to volume shrinkage for Li(Ni,Mn,Co)O_2, in contrast to (Ni,Mn)-free $LiCoO_2$ (see Fig. 42b). Electrochemical discharge experiments performed under a fast regime (2 C) at 5, 25 and 45 °C revealed that the discharge capacity followed the trend of an increased diffusion rate of Li^+ ions in the electrolyte and Li atoms in both electrodes, being highest for 45 °C. At the lowest tested temperature (5 °C), a rapid drop in the discharge capacity took place using the same kinetic regime.

An *operando* neutron imaging study of a commercial ICR 10440 Li ion battery during charge and discharge showed (Fig. 43a,b) that the cylindrical battery has a spiral configuration which is composed of a multiphase layered oxide cathode and graphite anode. In spite of a two-dimensional nature of the projection data of this time-resolved study, structural and functional details of the neutron radiography study were successfully uncovered and visualized. The spatially resolved measurements with a resolution of 40 μm enabled to observe Li redistribution between the electrodes as well as a circulation of the electrolyte between the central column and the electrode layers at different states of charge (SoC) and at different current rates. Furthermore, *ex-situ* tomographic studies of the battery revealed the fine details of the structural inhomogeneity within the cell.

8. Concluding remarks

This review presents numerous examples of the studies of hydrogen and energy storage materials, where neutron diffraction, and particularly when combined with Synchrotron X-ray diffraction, becomes a valuable tool in *in situ* probing of hydrogen storage properties. Even when using small, 100–500 mg, samples, these studies allow establishing the mechanism of phase-structural transformations and their kinetics based on rapid data collection at various charge-discharge conditions. These conditions include a broad range of applied deuterium pressures, from vacuum to high pressures reaching 1000 bar H_2/D_2, and temperatures, from cryo-cooling (2 K) to as high as 1273 K (1000 °C), while various state-of-charge and discharge setpoints have been achieved by measuring the PCT diagrams of H_2/D_2 absorption-desorption during the collection of the diffraction data or by applying variable current densities during the testing of the battery electrodes.

Collection of high quality *in situ* diffraction data benefits from a high flux beam and its combination with high resolution measurements, while the use of dedicated sample cells allows the application of appropriate testing conditions to reproduce the conditions of use of energy storage materials in the lab and in real applications. This is because the profile intensities of the diffraction pattern are utilized in the most efficient way as the data fitting covers a large *d*-spacing range and ensures improvements in the peak-to-background and signal-to-noise ratios thus mitigating the challenges caused by the small size of some studied samples, their low crystallinity, incoherent scattering of hydrogen atoms and diffraction signals from complex sample environments such as electrolytes. Most importantly, complex structures with large unit cells and low symmetry can be successfully determined, which is of particular importance in the studies of the phase-structural composition of single phase and multiphase hydride materials, even when in small amounts.

In situ experiments, performed under hydrogen/deuterium pressure at a range of temperatures, make demands on the type of sample cell used. It is necessary to simultaneously satisfy the

requirements of a material whose yield strength can support the experimental pressures used to the temperatures reached, does not deteriorate or embrittle with hydrogen and does not otherwise hinder the acquisition of quality diffraction data. A number of cells for specific solid-gas applications has been discussed. Moreover, for structural studies of metal hydride electrodes, amorphous silica cells which do not produce diffraction peaks have been used. Ancillary devices such as Sieverts' apparatuses, pressure gauges and galvanostats are used to control and monitor hydrogen/deuterium uptake and release during *in situ* neutron diffraction measurements. They are used in solid-gas and electrochemical studies.

The ability of neutrons to penetrate deeply into the matter makes neutron diffraction especially valuable for the study of bulk materials. The use of non-isotopically enriched samples makes many experiments far more accessible, and this has been established during *in situ* studies of protium-containing materials.

The use of multiple experimental diffraction data sets has become increasingly important. SR XRD data provide accurate information about the positions of heavy atoms (metal components) in the structure, which can then be fixed in the subsequent refinements of hydrogen positions using NPD data. Simultaneous refinement of the SR XRD and NPD data is the most preferable option which results in excellent resolution of hydrogen positions.

Major neutron instruments are open to scientists around the world. However, access to these instruments is competitive, based on the evaluation of the competing proposals, and is not normally straightforward even for accepted proposals as there is a time gap between the submission of the proposals and the scheduled experiments. The High Flux Isotope Reactor at ORNL, high-flux reactor at Institut Laue-Langevin (Grenoble, France), Neutron-Beam Split Core Reactor at NIST, FRM II (Munich, Germany), and OPAL reactor at the Australian Centre for Neutron Scattering (Lucas Heights, Australia) are on the list of the available nuclear research reactor institutions for the international community. This list is complemented by the neutron spallation sources which include the Spallation Neutron Source at ORNL, ISIS Neutron and Muon Source at Rutherford Appleton Laboratory (Chilton, UK), J-PARC (Japan), and the Swiss Spallation Neutron Source (SINQ), a continuous source at Paul Scherrer Institute (Villigen, Switzerland). Finally, the European Spallation Source is under construction in Lund, Sweden, and will be operating soon.

This paper is dedicated to the memory of Michel Latroche. In the context of this manuscript on *in situ* scattering analyses of structural determination and phase transformation in energy storage materials, the contribution of Michel Latroche is remarkable. Latroche's work has been mainly focused on the fundamental understanding of the relationships between structures, thermodynamic properties and physical properties of materials, without neglecting their applications in the field of chemical and electrochemical energy storage. In this perspective, his major achievements concern the fundamentals of metal hydrides and their application either as hydrogen gas storage for fuel cells or as negative electrodes for Ni-MH and Li-ion batteries [123, 143, 152–157].

After joining the Percherons-Guégan laboratory of CNRS France in 1989, Michel Latroche carried out pioneering work on *in situ* neutron diffraction studies of $LaNi_5$ based electrodes [45, 47–50, 63, 158]. In the 1990s, in collaboration with his colleague Yves Chabre, he developed the *in situ* neutron diffraction cell shown in Fig. 5 [45], which has been used during the experiments ar D20, ILL in 1998 (see Fig. 44), and is still used today. In the present century, electrochemical, structural and mechanistic studies using *in situ* neutron diffraction have expanded from AB_5-type electrodes to AB_3 [52,144,154], AB [51] and Mg-based electrodes [159]. In parallel with the structural studies concerning electrochemical storage, Latroche's work on *in situ* neutron diffraction has also provided a broad overview of materials for solid state hydrogen storage. In addition to the classical AB_5 compounds, over-stochiometric ones [35,109,160], AB_2 [60,81,161] and AB [55] intermetallics were considered. Last but not least, many other classes of materials have attracted his attention beyond intermetallics, such as Pd@C hybrids [162], Mg-based composites [36] and imide/amide systems [37]. Structural analysis of both battery and hydrogen gas storage materials has provided an in-depth understanding of the mechanisms underlying reversible hydrogen uptake, as well as their kinetic behaviour and cycle-life properties.

The recent progress in the development of advanced materials for hydrogen-based energy storage have been presented in recently published review papers [90,114,124,163]. We anticipate that *in situ* diffraction studies of hydrogen and energy storage materials, providing insights into understanding of their performance and allowing optimisation of the materials, will be growing further based on the use of advanced large-scale research facilities accessible to a broad international research community. This will facilitate progress in the socially important field of energy storage and conversion.

CRediT authorship contribution statement

V.A. Yartys: Conceptualization, Writing – review & editing, Funding acquisition. **F. Cuevas:** Conceptualization, Writing – review & editing, Funding acquisition. **C.J. Webb:** Conceptualization, Writing – review & editing, Funding acquisition.

Data Availability

Data will be made available on request.

Declaration of Competing Interest

The authors declare that they have no known competing financial interests or personal relationships that could have appeared to influence the work reported in this paper.

Acknowledgements

VAY acknowledges support from EU Horizon 2020 programme in the frame of the H2020-MSCARISE-2017 action, HYDRIDE4MOBILITY project, with Grant Agreement 778307 and from the Institute for Energy Technology. VAY is grateful to the colleagues from IFE, R.V. Denys and Chubin Wan and Denis Scheptyakov (PSI), for the fruitful collaboration in the *in situ* studies. FC acknowledges support from the French-Australian IRN-FACES network and the French National Research Agency (ANR) under France 2030 program and reference ANR-22-PEHY-0007. He also thanks his colleagues of ICMPE, France, for many fruitful discussions on neutron diffraction studies.

References

[1] A. Kumar, P. Muthukumar, P. Sharma, E.A. Kumar, Absorption based solid state hydrogen storage system: a review, Sustain. Energy Technol. Assess. 52 (2022) 102204.
[2] T.Y. Wei, K.L. Lim, Y.S. Tseng, S.L.I. Chan, A review on the characterization of hydrogen in hydrogen storage materials, Renew. Sustain. Energy Rev. 79 (2017) 1122–1133.
[3] M. Hosseini, M. Arif, A. Keshavarz, S. Iglauer, Neutron scattering: a subsurface application review, Earth-Sci. Rev. 221 (2021) 103755.
[4] R.A. Klein, H.A. Evans, B.A. Trump, T.J. Udovic, C.M. Brown, Neutron scattering studies of materials for hydrogen storage, Reference Module in Chemistry, Molecular Sciences and Chemical Engineering, Elsevier Ltd, Amsterdam, 2021.
[5] X. Zhang, Y. Sun, G. Xia, X. Yu, Light-weight solid-state hydrogen storage materials characterized by neutron scattering, J. Alloy. Compd. 899 (2022) 163254.
[6] E.M. Gray, C.J. Webb, In-situ diffraction techniques for studying hydrogen storage materials under high hydrogen pressure, Int. J. Hydrog. Energy 37 (2012) 10182–10195.
[7] H.-J. Lin, H.-W. Li, H. Shao, Y. Lu, K. Asano, In situ measurement technologies on solid-state hydrogen storage materials: a review, Mater. Today Energy 17 (2020) 100463.

[8] B.R.S. Hansen, K.T. Møller, M. Paskevicius, A.-C. Dippel, P. Walter, C.J. Webb, C. Pistidda, N. Bergemann, M. Dornheim, T. Klassen, J.-E. Jørgensen, T.R. Jensen, In situX-ray diffraction environments for high-pressure reactions, J. Appl. Crystallogr. 48 (2015) 1234–1241.

[9] H. Cheng, C. Lu, J. Liu, Y. Yan, X. Han, H. Jin, Y. Wang, Y. Liu, C. Wu, Synchrotron radiation X-ray powder diffraction techniques applied in hydrogen storage materials - a review, Prog. Nat. Sci.: Mater. Int. 27 (2017) 66–73.

[10] V.E. Antonov, V.K. Fedotov, A.S. Ivanov, A.I. Kolesnikov, M.A. Kuzovnikov, M. Tkacz, V.A. Yartys, Lattice dynamics of high-pressure hydrides studied by inelastic neutron scattering, J. Alloy. Compd. 905 (2022) 164208.

[11] D. Liu, K. Song, W. Chen, J. Chen, G. Sun, L. Li, Review: Current progresses of small-angle neutron scattering on soft-matters investigation, Nuclear, Analysis 1 (2022) 100011.

[12] D.L. Jacobson, D.S. Hussey, E. Baltic, T.J. Udovic, J.J. Rush, R.C. Bowman Jr, Neutron imaging studies of metal-hydride storage beds, Int. J. Hydrog. Energy 35 (2010) 12837–12845.

[13] A. Griesche, E. Solórzano, K. Beyer, T. Kannengiesser, The advantage of using in-situ methods for studying hydrogen mass transport: neutron radiography vs. carrier gas hot extraction, Int. J. Hydrog. Energy 38 (2013) 14725–14729.

[14] S. Börries, O. Metz, P.K. Pranzas, J.M. Bellosta von Colbe, T. Bücherl, M. Dornheim, T. Klassen, A. Schreyer, Optimization and comprehensive characterization of metal hydride based hydrogen storage systems using in-situ Neutron Radiography, J. Power Sources 328 (2016) 567–577.

[15] V.A. Yartys, V.V. Burnasheva, K.N. Semenenko, Structural chemistry of hydrides of intermetallic compounds, Sov. Adv. Chem. 52 (1983) 529–562.

[16] V.A. Yartys, M.V. Lototskyy, Laves type intermetallic compounds as hydrogen storage materials: a review, J. Alloy. Compd. 916 (2022) 165219.

[17] M. Bououdina, D. Grant, G. Walker, Review on hydrogen absorbing materials—structure, microstructure, and thermodynamic properties, Int. J. Hydrog. Energy 31 (2006) 177–182.

[18] E. Callini, K.-F. Aguey-Zinsou, R. Ahuja, J.R. Ares, S. Bals, N. Biliškov, S. Chakraborty, G. Charalambopoulou, A.-L. Chaudhary, F. Cuevas, B. Dam, P. de Jongh, M. Dornheim, Y. Filinchuk, J. Grbović Novaković, M. Hirscher, T.R. Jensen, P.B. Jensen, N. Novaković, Q. Lai, F. Leardini, D.M. Gattia, L. Pasquini, T. Steriotis, S. Turner, T. Vegge, A. Züttel, A. Montone, Nanostructured materials for solid-state hydrogen storage: a review of the achievement of COST Action MP1103, Int. J. Hydrog. Energy 41 (2016) 14404–14428.

[19] C. Li, P. Peng, D.W. Zhou, L. Wan, Research progress in $LiBH_4$ for hydrogen storage: a review, Int. J. Hydrog. Energy 36 (2011) 14512–14526.

[20] Y. Lv, Y. Wu, Current research progress in magnesium borohydride for hydrogen storage (a review), Prog. Nat. Sci.: Mater. Int. 31 (2021) 809–820.

[21] L. Ouyang, K. Chen, J. Jiang, X.-S. Yang, M. Zhu, Hydrogen storage in light-metal based systems: a review, J. Alloy. Compd. 829 (2020) 154597.

[22] K.K. Gangu, S. Maddila, S.B. Mukkamala, S.B. Jonnalagadda, Characteristics of MOF, MWCNT and graphene containing materials for hydrogen storage: a review, J. Energy Chem. 30 (2019) 132–144.

[23] T.C. Hansen, P.F. Henry, H.E. Fischer, J. Torregrossa, P. Convert, The D20 instrument at the ILL: a versatile high-intensity two-axis neutron diffractometer, Meas. Sci. Technol. 19 (2008) 034001.

[24] S.F. Nowicki, S.A. Wender, M. Mocko, The Los Alamos neutron science center spallation neutron sources, Phys. Procedia 90 (2017) 374–380.

[25] S. Torii, M. Yonemura, T. Yulius Surya Panca Putra, J. Zhang, P. Miao, T. Muroya, R. Tomiyasu, T. Morishima, S. Sato, H. Sagehashi, Y. Noda, T. Kamiyama, Super high resolution powder diffractometer at J-PARC, J. Phys. Soc. Jpn. 80 (2011) SB020.

[26] K. Nakajima, Y. Kawakita, S. Itoh, J. Abe, K. Aizawa, H. Aoki, H. Endo, M. Fujita, K. Funakoshi, W. Gong, M. Harada, S. Harjo, T. Hattori, M. Hino, T. Honda, A. Hoshikawa, K. Ikeda, T. Ino, T. Ishigaki, Y. Ishikawa, H. Iwase, T. Kai, R. Kajimoto, T. Kamiyama, N. Kaneko, D. Kawana, S. Ohira-Kawamura, T. Kawasaki, A. Kimura, R. Kiyanagi, K. Kojima, K. Kusaka, S. Lee, S. Machida, T. Masuda, K. Mishima, K. Mitamura, M. Nakamura, S. Nakamura, A. Nakao, T. Oda, T. Ohhara, K. Ohishi, H. Ohshita, K. Oikawa, T. Otomo, A. Sano-Furukawa, K. Shibata, T. Shinohara, K. Soyama, J.-i Suzuki, K. Suzuya, A. Takahara, S.-i Takata, M. Takeda, Y. Toh, S. Torii, N. Torikai, N. Yamada, T. Yamada, D. Yamazaki, T. Yokoo, M. Yonemura, H. Yoshizawa, Materials and Life Science Experimental Facility (MLF) at the Japan Proton Accelerator Research Complex II: Neutron Scattering Instruments, Quantum Beam, Science 1 (3) (2017) 9.

[27] R.P. Ganglof, B.P. Somerday, Gaseous Hydrogen Embrittlement of Materials in Energy Technologies, Woodhead: Cambridge, 2012.

[28] M. Hatem, S. Agamy, M.Y. Khalil, In-situ hydrogen in metal determination using a minimum neutron source strength and exposure time, Appl. Radiat. Isot. 78 (2013) 132–138.

[29] D.A. Sheppard, M. Paskevicius, P. Javadian, I.J. Davies, C.E. Buckley, Methods for accurate high-temperature Sieverts-type hydrogen measurements of metal hydrides, J. Alloy. Compd. 787 (2019) 1225–1237.

[30] Y. Murakami, T. Kanezaki, Y. Mine, S. Matsuoka, Hydrogen embrittlement mechanism in fatigue of austenitic stainless steels, Metall. Mater. Trans. A 39A (2008) 1327–1339.

[31] T.D. Humphries, D.A. Sheppard, M.R. Rowles, M.V. Sofianos, C.E. Buckley, Fluoride substitution in sodium hydride for thermal energy storage applications, J. Mater. Chem. A 4 (2016) 12170–12178.

[32] R.V. Denys, V.A. Yartys, C.J. Webb, Hydrogen in $La_2MgNi_9D_{13}$: the role of magnesium, Inorg. Chem. 51 (2012) 4231–4238.

[33] T.A. Webb, C.J. Webb, A.K. Dahle, E.M. Gray, In-situ neutron powder diffraction study of Mg–Zn alloys during hydrogen cycling, Int. J. Hydrog. Energy 40 (2015) 8106–8109.

[34] J.-M. Joubert, Crystal structure, hydrogen absorption properties and crystal structure of the deuterides of some Nb–Ni derived μ phase compounds, J. Solid State Chem. 178 (2005) 1620–1629.

[35] F. Cuevas, J.-M. Joubert, M. Latroche, O. Isnard, A. Percheron-Guégan, In situ neutron-diffraction study of deuterium desorption from $LaNi_{5+x}$(x~1) alloy, Appl. Phys. A 74 (2002) s1175–s1177.

[36] M. Ponthieu, F. Cuevas, J.F. Fernández, L. Laversenne, F. Porcher, M. Latroche, Structural properties and reversible deuterium loading of MgD_2–TiD_2 nanocomposites, J. Phys. Chem. C. 117 (2013) 18851–18862.

[37] Z. Li, J. Zhang, M. Latroche, S. Wang, L. Jiang, J. Du, F. Cuevas, Mechanochemical synthesis in the Li–Mg–N–D system under deuterium gas: a neutron diffraction study, Phys. Chem. Chem. Phys. 18 (2016) 23944–23953.

[38] M.P. Pitt, C.J. Webb, M. Paskevicius, D. Sheptyakov, C.E. Buckley, E.M. Gray, In situ neutron diffraction study of the deuteration of isotopic $Mg^{11}B_2$, J. Phys. Chem. C. 115 (2011) 22669–22679.

[39] V.A. Yartys, R.V. Denys, C.J. Webb, J.P. Mæhlen, E.M. Gray, T. Blach, O. Isnard, L.C. Barnsley, High pressure in situ diffraction studies of metal–hydrogen systems, J. Alloy. Compd. 509 (Supplement 2) (2011) S817–S822.

[40] V. Yartys, R. Denys, J.P. Maehlen, C.J. Webb, E.M. Gray, T. Blach, A.A. Poletaev, J.K. Solberg, O. Isnard, Nanostructured metal hydrides for hydrogen storage studied by in situ synchrotron and neutron diffraction, Mater. Res. Soc. Symp. Proc. (2010) 69–79.

[41] M. Bianchini, J.B. Leriche, J.-L. Laborier, L. Gendrin, E. Suard, L. Croguennec, C. Masquelier, A. New, Null matrix electrochemical cell for rietveld refinements of in-situ or operando neutron powder diffraction data, J. Electrochem. Soc. 160 (2013) A2176.

[42] S.S. Mohammadshahi, T.A. Webb, E.M. Gray, C.J. Webb, Experimental and theoretical study of compositional inhomogeneities in $LaNi_5D_x$ owing to temperature gradients and pressure hysteresis, investigated using spatially resolved in-situ neutron diffraction, Int. J. Hydrog. Energy 42 (2017) 6793–6800.

[43] T.R. Jensen, T.K. Nielsen, Y. Filinchuk, J.-E. Jorgensen, Y. Cerenius, E.M. Gray, C.J. Webb, Versatile in situ powder X-ray diffraction cells for solid-gas investigations, J. Appl. Crystallogr. 43 (2010) 1456–1463.

[44] K. Ikeda, H. Ohshita, T. Otomo, K. Sakaki, H. Kim, Y. Nakamura, A. Machida, R.B. Von Dreele, Pressure cells for in situ neutron total scattering: time and real-space resolution during deuterium absorption, J. Appl. Crystallogr. 55 (2022) 1631–1639.

[45] M. Latroche, Y. Chabre, B. Decamps, A. Percheron-Guégan, D. Noreus, In situ neutron diffraction study of the kinetics of metallic hydride electrodes, J. Alloy. Compd. 334 (2002) 267–276.

[46] M. Ripert, J. Pannetier, Y. Chabre, C. Poinsignon, Manganese dioxides: structural model and in-situ neutron powder diffraction investigation of thermal annealing and electrochemical reduction, MRS Online Proc. Libr. OPL 210 (1990) 359.

[47] M. Latroche, A. Percheron-Guegan, Y. Chabre, C. Poinsignon, J. Pannetier, In situ neutron diffraction study of the behaviour of $LaNi_{4.5}Al_{0.5}D_x$ electrode during deuterium charge-discharge, J. Alloy. Compd. 189 (1992) 59–65.

[48] M. Latroche, A. Percheron-Guégan, Y. Chabre, J. Bouet, J. Pannetier, E. Ressouche, Intrinsic behaviour analysis of substituted $LaNi_5$-type electrodes by means of in-situ neutron diffraction, J. Alloy. Compd. 231 (1995) 537–545.

[49] M. Latroche, Y. Chabre, A. Percheron-Guégan, O. Isnard, B. Knosp, Influence of stoichiometry and composition on the structural and electrochemical properties of AB_{5+y}-based alloys used as negative electrode materials in Ni–MH batteries, J. Alloy. Compd., 330- 332 (2002) 787–791.

[50] S. Vivet, M. Latroche, Y. Chabre, J.-M. Joubert, B. Knosp, A. Percheron-Guégan, Influence of composition on phase occurrence during charge process of AB_{5+x} Ni-MH negative electrode materials, Phys. B: Condens 362 (2005) 199–207.

[51] H. Emami, F. Cuevas, M. Latroche, Ti(Ni,Cu) pseudobinary compounds as efficient negative electrodes for Ni–MH batteries, J. Power Sources 265 (2014) 182–191.

[52] M. Latroche, F. Cuevas, W.-K. Hu, D. Sheptyakov, R.V. Denys, V.A. Yartys, Mechanistic and kinetic study of the electrochemical charge and discharge of La_2MgNi_9 by in situ powder neutron diffraction, J. Phys. Chem. C. 118 (2014) 12162–12169.

[53] F. Bardé, M.R. Palacin, Y. Chabre, O. Isnard, J.-M. Tarascon, In situ neutron powder diffraction of a nickel hydroxide electrode, Chem. Mater. 16 (2004) 3936–3948.

[54] J.J. Biendicho, M. Roberts, C. Offer, D. Noréus, E. Widenkvist, R.I. Smith, G. Svensson, K. Edström, S.T. Norberg, S.G. Eriksson, S. Hull, New in-situ neutron diffraction cell for electrode materials, J. Power Sources 248 (2014) 900–904.

[55] E.M. Dematteis, J. Barale, G. Capurso, S. Deledda, M.H. Sørby, F. Cuevas, M. Latroche, M. Baricco, In-situ neutron diffraction during reversible deuterium loading in Ti-rich and Mn-substituted $Ti(Fe,Mn)_{0.90}$ alloys, J. Alloy. Compd. 935 (2023) 168150-116161.

[56] M. Dottor, J.-C. Crivello, L. Laversenne, J.-M. Joubert, Experimental determination of the H–Hf phase diagram using in situ neutron diffraction, J. Alloy. Compd. 937 (2023) 168353–168360.

[57] D.P. Broom, C.J. Webb, Pitfalls in the characterisation of the hydrogen sorption properties of materials, Int. J. Hydrog. Energy 42 (2017) 29320–29343.

[58] H. Hemmes, A. Driessen, R. Griessen, Thermodynamic properties of hydrogen at pressures up to 1 Mbar and temperatures between 100 and 1000 K, J. Phys. C: Solid State Phys. 19 (1986) 3571.

[59] N. Pineda-Romero, M. Witman, V. Stavila, C. Zlotea, The effect of 10 at% Al addition on the hydrogen storage properties of the $Ti_{0.33}V_{0.33}Nb_{0.33}$ multi-principal element alloy, Intermetallics 146 (2022) 107590.

[60] T. Leblond, V. Paul-Boncour, F. Cuevas, O. Isnard, J.F. Fernández, Study of the multipeak deuterium thermodesorption in YFe_2D_x ($1.3 \le x \le 4.2$) by DSC, TD and in situ neutron diffraction, Int. J. Hydrog. Energy 34 (2009) 2278–2287.

[61] F. Cuevas, M. Latroche, F. Bourée-Vigneron, A. Percheron-Guégan, A conjoint XRD–ND analysis of the crystal structures of austenitic and martensitic $Ti_{0.64}Zr_{0.36}Ni$ hydrides, J. Solid State Chem. 179 (2006) 3295–3307.

[62] P.A. Redhead, Thermal desorption of gases, Vacuum 12 (1962) 203–211.

[63] M. Latroche, A. Percheron-Guégan, Y. Chabre, Influence of cobalt content in $MmNi_{4.3-x}Mn_{0.3}Al_{0.4}Co_x$ alloy (x=0.36 and 0.69) on its electrochemical behaviour studied by in situ neutron diffraction, J. Alloy. Compd. 293–295 (1999) 637–642.

[64] A. Lasia, D. Grégoire, General model of electrochemical hydrogen absorption into metals, J. Electrochem. Soc. 142 (1995) 3393.

[65] C. Wan, R.V. Denys, V.A. Yartys, In situ neutron powder diffraction study of phase-structural transformations in the La–Mg–Ni battery anode alloy, J. Alloy. Compd. 670 (2016) 210–216.

[66] M.V. Lototsky, R.V. Denys, V.A. Yartys, Combustion-type hydrogenation of nanostructured Mg-based composites for hydrogen storage, Int. J. Energy Res. 33 (2009) 1114–1125.

[67] C. Wan, V.E. Antonov, R.V. Denys, V.I. Kulakov, V.A. Yartys, $MgCo_2$-D_2 and MgCoNi-D_2 systems synthesized at high pressures and interaction mechanism during the HDDR processing, Prog. Nat. Sci.: Mater. Int. 27 (2017) 74–80.

[68] H. Figiel, A. Budziak, P. Zachariasz, J. Żukrowski, G. Fischer, E. Dormann, Hydrogen induced structural and magnetic transformations in the hexagonal Laves phase $ErMn_2$, J. Alloy. Compd. 368 (2004) 260–268.

[69] J.P. Maehlen, V.A. Yartys, A.B. Riabov, A. Budziak, H. Figiel, J. Żukrowski, Synchrotron X-ray diffraction study of $ErMn_2D_2$, J. Alloy. Compd. 437 (2007) 140–145.

[70] H.W. Brinks, V.A. Yartys, B.C. Hauback, Crystal structure of $TbNiSiD_{1.78}$, J. Alloy. Compd. 322 (2001) 160–165.

[71] V.A. Yartys, R.V. Denys, O. Isnard, R.G. Delaplane, P. Svedlindh, K.H.J. Buschow, Crystal and magnetic structure of TbNiSnD studied by neutron powder diffraction, J. Magn. Magn. Mater. 311 (2007) 639–643.

[72] H.W. Brinks, V.A. Yartys, B.C. Hauback, H. Fjellvåg, B. Ouladdiaf, The magnetic structure of $TbNiSiD_{1.78}$, J. Alloy. Compd. 340 (2002) 62–66.

[73] V.A. Yartys, B. Ouladdiaf, O. Isnard, O.Y. Khyzhun, K.H.J. Buschow, Hydrogen induced antiferromagnetism in the Kondo semimetal CeNiSn, J. Alloy. Compd. 359 (2003) 62–65.

[74] V.A. Yartys, O. Isnard, A.B. Riabov, L.G. Akselrud, Unusual effects on hydrogenation: anomalous expansion and volume contraction, J. Alloy. Compd., 356-357 (2003) 109–113.

[75] A. Szytuła, O. Isnard, V.A. Yartys, A.B. Riabov, Crystal and magnetic structure of $HoNiSnD_{0.67}$, J. Alloy. Compd. 404–406 (2005) 200–203.

[76] V.A. Yartys, R.V. Denys, B.C. Hauback, H. Fjellvåg, I.I. Bulyk, A.B. Riabov, Y.M. Kalychak, Short hydrogen–hydrogen separations in novel intermetallic hydrides, $RE_3Ni_3In_3D_4$ (RE=La, Ce and Nd), J. Alloy. Compd. 330-332 (2002) 132–140.

[77] T. Spataru, G. Principi, V. Kuncser, W. Keune, V.A. Yartys, Mössbauer study of the RENiSnD (RE: Pr, Nd) monodeuterides, J. Alloy. Compd. 366 (2004) 81–85.

[78] T. Spataru, P. Palade, G. Principi, P. Blaha, K. Schwarz, V. Kuncser, S. Lo Russo, S. Dal Toe, V.A. Yartys, The nature of the hydrogen bond in the $LaNiSnH_2$ and NdNiSnH hydrides, J. Chem. Phys. 122 (2005) 124703.

[79] V.A. Yartys, V.V. Berezovets, P. Vajeeston, L.G. Akselrud, V. Antonov, V. Fedotov, S. Klenner, R. Pöttgen, D. Chernyshov, M. Heere, A. Senyshyn, R.V. Denys, L. Havela, Hydrogen induced structural phase transformation in ScNiSn-based intermetallic hydride characterized by experimental and computational studies, Acta Mater. 244 (2023) 118549.

[80] M. Latroche, V. Paul-Boncour, A. Percheron-Guégan, F. Bourée-Vigneron, Crystallographic study of $YFe_2D_{3.5}$ by X-ray and neutron powder diffraction, J. Solid State Chem. 133 (1997) 568–571.

[81] V. Paul-Boncour, L. Guénée, M. Latroche, A. Percheron-Guégan, B. Ouladdiaf, F. Bourée-Vigneron, Elaboration, structures, and phase transitions for YFe_2D_xcompounds (x=1.3, 1.75, 1.9, 2.6) studied by neutron diffraction, J. Solid State Chem. 142 (1999) 120–129.

[82] G. Wiesinger, V. Paul-Boncour, S.M. Filipek, C. Reichl, I. Marchuk, A. Percheron-Guégan, Structural and magnetic properties of RFe_2D_x deuterides (R = Zr, Y and $x \ge 3.5$) studied by means of neutron diffraction and ^{57}Fe Mössbauer, Spectrosc., J. Phys.: Condens. Matter 17 (2005) 893.

[83] J. Ropka, R. Černý, V. Paul-Boncour, T. Proffen, Deuterium ordering in Laves-phase deuteride $YFe_2D_{4.2}$, J. Solid State Chem. 182 (2009) 1907–1912.

[84] V. Paul-Boncour, G. André, F. Bourée, M. Guillot, G. Wiesinger, A. Percheron-Guégan, Influence of H/D isotopic substitution on the first-order magnetic transition in $YFe_2(D_{1-x}H_x)_{4.2}$ compounds (x=0, 0.64, 1), Phys. B: Condens 350 (2004) E27–E30.

[85] V. Paul-Boncour, M. Guillot, G. Wiesinger, G. André, Giant isotope effect on the itinerant-electron metamagnetism in $YFe_2(H_yD_{1-y})_{4.2}$, Phys. Rev. B 72 (2005) 174430.

[86] J.-M. Park, J.-Y. Lee, An investigation of the hydrogen site occupancy in the $ErFe_2$-H system by a hydrogen thermal desorption study, Scr. Metall. 23 (1989) 1525–1530.

[87] A. Stern, A. Resnik, D. Shaltiel, Thermal desorption spectra of hydrogen in HfV_2H_x and ZrV_2H_x, J. less-Common Met. 88 (1982) 431–440.

[88] V.A. Yartys, F.R. de Boer, K.H.J. Buschow, B. Ouladdiaf, H.W. Brinks, B.C. Hauback, Crystallographic and magnetic structure of $Pr_6Fe_{13}AuD_{13}$, J. Alloy. Compd., 356-357 (2003) 142–146.

[89] S. Mašková, J.-N. Chotard, R.V. Denys, K. Miliyanchuk, V. Yartys, M. Giovannini, L. Akselrud, I. Halevy, J. Prokleška, L. Havela, $Nd_2Ni_2MgH_8$ hydride: synthesis, structure and magnetic properties, Intermetallics 87 (2017) 13–20.

[90] V.A. Yartys, M.V. Lototskyy, E. Akiba, R. Albert, V.E. Antonov, J.R. Ares, M. Baricco, N. Bourgeois, C.E. Buckley, J.M. Bellosta von Colbe, J.C. Crivello, F. Cuevas, R.V. Denys, M. Dornheim, M. Felderhoff, D.M. Grant, B.C. Hauback, T.D. Humphries, I. Jacob, T.R. Jensen, P.E. de Jongh, J.M. Joubert, M.A. Kuzovnikov, M. Latroche, M. Paskevicius, L. Pasquini, L. Popilevsky, V.M. Skripnyuk, E. Rabkin, M.V. Sofianos, A. Stuart, G. Walker, H. Wang, C.J. Webb, M. Zhu, Magnesium based materials for hydrogen based energy storage: past, present and future, Int. J. Hydrog. Energy 44 (2019) 7809–7859.

[91] M. Sato, M. Stange, V.A. Yartys, Desorption behaviour of hydrogen in the $LaNi_{4.7}Sn_{0.3}$-H system, J. Alloy. Compd. 396 (2005) 197–201.

[92] M. Stange, J.P. Maehlen, V.A. Yartys, P. Norby, W. van Beek, H. Emerich, In situ SR-XRD studies of hydrogen absorption–desorption in $LaNi_{4.7}Sn_{0.3}$, J. Alloy. Compd. 404-406 (2005) 604–608.

[93] A.B. Riabov, R.V. Denys, J.P. Maehlen, V.A. Yartys, Synchrotron diffraction studies and thermodynamics of hydrogen absorption–desorption processes in $La_{0.5}Ce_{0.5}Ni_4Co$, J. Alloy. Compd. 509 (2011) S844–S848.

[94] F. Cuevas, M. Latroche, M. Hirscher, A. Percheron-Guégan, Formation and structure of highly over-stoichiometric $LaNi_{5+x}$ (x~1) alloys obtained by manifold non-equilibrium methods, J. Alloy. Compd. 323-324 (2001) 4–7.

[95] V.A. Yartys, S.V. Mitrokhin, V.N. Verbetzky, K.N. Semenenko, Crystal structure of $TiFe_{1.16}V_{0.84}D_{1.9}$, Zh. Neorg. Khim. 37 (1992) 32–37.

[96] V.V. Burnasheva, V.A. Yartys, N.V. Fadeeva, S.P. Solov'ev, K.N. Semenenko, The crystal structure of $ZrMoFeD_{2.6}$ deuteride, Sov. Crystallogr (1982) 900–904.

[97] V.A. Yartys, V.V. Burnasheva, N.V. Fadeeva, V.A. Sarin, L.E. Fykin, K.N. Semenenko, Neutron diffraction investigation of the crystal and magnetic structure of λ_1-$ScFe_2D_{2.5}$, Zh. Neorgan. Chim. Russ. J. Inorg. Chem. 31 (1986) 2500–2503.

[98] V.A. Yartys, V.V. Burnasheva, N.V. Fadeeva, V.A. Sarin, L.E. Fykin, K.N. Semenenko, The crystal and magnetic structure of $ScFe_2D_{2.9}$, Zh. Neorgan. Chim. Russ. J. Inorg. Chem. 31 (1986) 311–317.

[99] J.-J. Didisheim, K. Yvon, F.P.D. Shaltiel, The deuterium site occupation in ZrV_2D_x as a function of the deuterium concentration, J. Less-Common Met 73 (1980) 355.

[100] V.A. Yartys, V.V. Burnasheva, K.N. Semenenko, N.V. Fadeeva, S.P. Solov'ev, Crystal chemistry of $RT_5H(D)_x$, $RT_2H(D)_x$ and $RT_3H(D)_x$ hydrides based on intermetallic compounds of $CaCu_5$, $MgCu_2$, $MgZn_2$ and $PuNi_3$ structure types, Int. J. Hydrog. Energy 7 (1982) 957–965.

[101] V.A. Yartys, V.V. Burnasheva, S.E. Tzyrkunova, E.N. Kozlov, K.N. Semenenko, Neutron diffraction investigation of the $ZrVFeD_{3.6}$, $ZrVCuD_{4.0}$ and $ZrVNbD_{5.4}$ deuterides, Izv.AN Latv.SSR, Ser. Phys. Technol. Sci. 5 (1983) 14–20.

[102] C. Wan, R.V. Denys, M. Lelis, D. Milčius, V.A. Yartys, Electrochemical studies and phase-structural characterization of a high-capacity La-doped AB_2 laves type alloy and its hydride, J. Power Sources 418 (2019) 193–201.

[103] A.N. Bogdanova, A.V. Irodova, G. Andre, F. Bouree, The ZrV_2D_6 crystal structure, J. Alloy. Compd. 356-357 (2003) 50–53.

[104] E.M. Dematteis, N. Berti, F. Cuevas, M. Latroche, M. Baricco, Substitutional effects in TiFe for hydrogen storage: a comprehensive review, Mater. Adv. 2 (2021) 2524–2560.

[105] E.M. Dematteis, D.M. Dreistadt, G. Capurso, J. Jepsen, F. Cuevas, M. Latroche, Fundamental hydrogen storage properties of TiFe-alloy with partial substitution of Fe by Ti and Mn, J. Alloy. Compd. 874 (2021) 159925.

[106] P. Fischer, Neutron scattering investigations of the $LaNi_5$ hydrogen storage system, Helv. Phys. Acta 50 (1977) 421–430.

[107] C. Lartigue, A. Percheron-Guegan, J.C. Achard, J.L. Soubeyroux, Hydrogen (deuterium) ordering in the β-$LaNi_5D_{x>5}$ phases: a neutron diffraction study, J. Less-Common Met. 113 (1985) 127–148.

[108] M. Latroche, J. Rodríguez-Carvajal, A. Percheron-Guégan, F. Bourée-Vigneron, Structural studies of $LaNi_4CoD_{6.11}$ and $LaNi_{3.55}Mn_{0.4}Al_{0.3}Co_{0.75}D_{5.57}$ by means of neutron powder diffraction, J. Alloy. Compd. 218 (1995) 64–72.

[109] M. Latroche, J.M. Joubert, A. Percheron-Guégan, F. Bourée-Vigneron, Neutron diffraction study of the deuterides of the over-stoichiometric compounds $LaNi_{5+x}$, J. Solid State Chem. 177 (2004) 1219–1229.

[110] R. Denys, V. Yartys, E. Gray, C. Webb, $LaNi_5$-assisted hydrogenation of $MgNi_2$ in the hybrid structures of $La_{1.09}Mg_{1.91}Ni_9D_{9.5}$ and $La_{0.91}Mg_{2.09}Ni_9D_{9.4}$, Energies 8 (2015) 3198–3211.

[111] V.A. Yartys, V.E. Antonov, D. Chernyshov, J.C. Crivello, R.V. Denys, V.K. Fedotov, M. Gupta, V.I. Kulakov, M. Latroche, D. Sheptyakov, Structure and chemical bonding in $MgNi_2H_3$ from combined high resolution synchrotron and neutron diffraction studies and ab initio electronic structure calculations, Acta Mater. 98 (2015) 416–422.

[112] V.A. Yartys, V.E. Antonov, A.I. Beskrovnyy, J.C. Crivello, R.V. Denys, V.K. Fedotov, M. Gupta, V.I. Kulakov, M.A. Kuzovnikov, M. Latroche, Y.G. Morozov, S.G. Sheverev, B.P. Tarasov, Hydrogen-assisted phase transition in a trihydride $MgNi_2H_3$ synthesized at high H_2 pressures: thermodynamics, crystallographic and electronic structures, Acta Mater. 82 (2015) 316–327.

[113] R.V. Denys, A.B. Riabov, J.P. Maehlen, M.V. Lototsky, J.K. Solberg, V.A. Yartys, In situ synchrotron X-ray diffraction studies of hydrogen desorption and absorption properties of Mg and Mg–Mm–Ni after reactive ball milling in hydrogen, Acta Mater. 57 (2009) 3989–4000.

[114] L. Pasquini, K. Sakaki, E. Akiba, M.D. Allendorf, E. Alvares, J.R. Ares, D. Babai, M. Baricco, J. Bellosta von Colbe, M. Bereznitsky, C.E. Buckley, Y.W. Cho, F. Cuevas, P. de Rango, E.M. Dematteis, R.V. Denys, M. Dornheim, J.F. Fernández, A. Hariyadi, B.C. Hauback, T.W. Heo, M. Hirscher, T.D. Humphries, J. Huot,

I. Jacob, T.R. Jensen, P. Jerabek, S.Y. Kang, N. Keilbart, H. Kim, M. Latroche, F. Leardini, H. Li, S. Ling, M.V. Lototskyy, R. Mullen, M. S.-i. Orimo, C. Paskevicius, M. Pistidda, J. Polanski, E. Puszkiel, M. Rabkin, S. Sahlberg, A. Sartori, T. Santhosh, R.Z. Sato, M.H. Shneck, Y. Sørby, V. Shang, J.-Y. Stavila, S. Suh, L. Suwarno, L.F. Thi Thu, C.J. Wan, M. Webb, C. Witman, B.C. Wan, V.A. Wood, Yartys, Magnesium- and intermetallic alloys-based hydrides for energy storage: modelling, synthesis and properties, Prog. Energy 4 (2022) 032007.

[115] I.D. Wijayanti, R. Denys, A.A. Suwarno, M.V. Volodin, M.N. Lototskyy, J. Guzik, K. Nei, H.J. Young, V. Roven, Yartys, Hydrides of Laves type Ti–Zr alloys with enhanced H storage capacity as advanced metal hydride battery anodes, J. Alloy. Compd. 828 (2020) 154354.

[116] A. Hariyadi, S. Suwarno, R.V. Denys, J.B. von Colbe, T.O. Sætre, V. Yartys, Modeling of the hydrogen sorption kinetics in an AB_2 laves type metal hydride alloy, J. Alloy. Compd. 893 (2022) 162135.

[117] Chubin Wan, R.V. Denys, V.A. Yartys, D. Scheptyakov, B. Guilherme F. Eggert, D. Wragg, Phase-Structural Transformations In Ti-Zr-Based $AB_{1.95}$ Alloys During Deuterium Absorption and Desorption Studied at Pressures 5 and 10 bar D_2 at 300 – 473 K, (In preparation).

[118] M. Ponthieu, M. Calizzi, L. Pasquini, J.F. Fernández, F. Cuevas, Synthesis by reactive ball milling and cycling properties of MgH_2–TiH_2 nanocomposites: kinetics and isotopic effects, Int. J. Hydrog. Energy 39 (2014) 9918–9923.

[119] P. Rizo-Acosta, F. Cuevas, M. Latroche, Hydrides of early transition metals as catalysts and grain growth inhibitors for enhanced reversible hydrogen storage in nanostructured magnesium, J. Mater. Chem. A 7 (2019) 23064–23075.

[120] F. Cuevas, D. Korablov, M. Latroche, Synthesis, structural and hydrogenation properties of Mg-rich MgH_2-TiH_2 nanocomposites prepared by reactive ball milling under hydrogen gas, Phys. Chem. Chem. Phys. 14 (2012) 1200–1211.

[121] R.V. Denys, A.A. Poletaev, J.P. Maehlen, J.K. Solberg, B.P. Tarasov, V.A. Yartys, Nanostructured rapidly solidified $LaMg_{11}Ni$ alloy. II. In situ synchrotron X-ray diffraction studies of hydrogen absorption–desorption behaviours, Int. J. Hydrog. Energy 37 (2012) 5710–5722.

[122] V. Yartys, D. Noreus, M. Latroche, Metal hydrides as negative electrode materials for Ni–MH batteries, Appl. Phys. A 122 (2016) 43.

[123] A. El Kharbachi, O. Zavorotynska, M. Latroche, F. Cuevas, V. Yartys, M. Fichtner, Exploits, advances and challenges benefiting beyond Li-ion battery technologies, J. Alloy. Compd. 817 (2020) 153261.

[124] F. Cuevas, M.B. Amdisen, M. Baricco, C.E. Buckley, Y.W. Cho, P. de Jongh, L.M. de Kort, J.B. Grinderslev, V. Gulino, B.C. Hauback, M. Heere, T. Humphries, T.R. Jensen, S. Kim, K. Kisu, Y.-S. Lee, H.-W. Li, R. Mohtadi, K.T. Møller, P. Ngene, D. Noréus, M. S.-i. Orimo, M. Paskevicius, S. Polanski, L.N. Sartori, M.H. Skov, B.C. Sørby, V.A. Wood, M. Yartys, M. Zhu, Latroche, Metallic and complex hydride-based electrochemical storage of energy, Prog. Energy 4 (2022) 032001.

[125] V.A. Yartys, New aspects of the structural chemistry of hydrides of intermetallic compounds: "isotropic" and "anisotropic" structures, Koordinatz.Khim, Soviet J. Coord. Chem. 18 (1992) 401–408.

[126] V.A. Yartys, A.B. Riabov, R.V. Denys, M. Sato, R.G. Delaplane, Novel intermetallic hydrides, J. Alloy. Compd., 408- 412 (2006) 273–279.

[127] R.V. Denys, V.A. Yartys, M. Sato, A.B. Riabov, R.G. Delaplane, Crystal chemistry and thermodynamic properties of anisotropic $Ce_2Ni_7H_{4.7}$ hydride, J. Solid State Chem. 180 (2007) 2566–2576.

[128] R.V. Denys, A.B. Riabov, V.A. Yartys, M. Sato, R.G. Delaplane, Mg substitution effect on the hydrogenation behaviour, thermodynamic and structural properties of the La_2Ni_7–$H(D)_2$ system, J. Solid State Chem. 181 (2008) 812–821.

[129] V.A. Yartys, P. Vajeeston, A.B. Riabov, P. Ravindran, R.V. Denys, J.P. Maehlen, R.G. Delaplane, H. Fjellvåg, Crystal chemistry and metal-hydrogen bonding in anisotropic and interstitial hydrides of intermetallics of rare earth (R) and transition metals (T), RT_3 and R_2T_7, Z. Krist. 223 (2008) 674–689.

[130] M. Stange, V.A. Yartys, J.P. Mæhlen, M. Hanfland, High pressure synchrotron XRD study of the pressure induced structural changes in $LaNiInD_{1.63-x}$, –x, J. Alloy. Compd. 356-357 (2003) 395–399.

[131] P. Vajeeston, P. Ravindran, R. Vidya, A. Kjekshus, H. Fjellvåg, V.A. Yartys, Short hydrogen-hydrogen separation in $RNiInH_{1.333}$ (R=La,Ce, Nd), Phys. Rev. B 67 (2003) 014101-014101-014111.

[132] R.A. Klein, R. Balderas-Xicohténcatl, J.P. Maehlen, T.J. Udovic, C.M. Brown, R. Delaplane, Y. Cheng, R.V. Denys, A.J. Ramirez-Cuesta, V.A. Yartys, Neutron vibrational spectroscopic evidence for short H···H contacts in the $RNiInH_{1.4;\ 1.6}$ (R = Ce, La) metal hydride, J. Alloy. Compd. 894 (2022) 162381.

[133] R.A. Klein, R. Balderas-Xicohténcatl, J.P. Maehlen, T.J. Udovic, C.M. Brown, R. Delaplane, Y. Cheng, R.V. Denys, A.J. Ramirez-Cuesta, V.A. Yartys, Neutron vibrational spectroscopic evidence for short H···H contacts in the $RNiInH_{1.4;1.6}$ (R = Ce, La) metal hydride, Neutron News 33 (2022) 7–9.

[134] R.V. Denys, V.A. Yartys, Effect of magnesium on the crystal structure and thermodynamics of the $La_{3-x}MgxNi_9$ hydrides, J. Alloy. Compd. 509 (2011) S540–S548.

[135] V. Yartys, R.V. Denys, Thermodynamics and crystal chemistry of the $RE_2MgNi_9H_{12-13}$ (RE=La and Nd) hydrides, Chem. Met. Alloy. 7 (2014) 1–8.

[136] I.E. Gabis, E.A. Evard, A.P. Voyt, V.G. Kuznetsov, B.P. Tarasov, J.C. Crivello, M. Latroche, R.V. Denys, W. Hu, V.A. Yartys, Modeling of metal hydride battery anodes at high discharge current densities and constant discharge currents, Electrochim. Acta 147 (2014) 73–81.

[137] V. Yartys, R. Denys, Structure–properties relationship in $RE_{3-x}Mg_xNi_9H_{10-13}$ (RE = La,Pr,Nd) hydrides for energy storage, J. Alloy. Compd. 645 (2015) S412–S418.

[138] A.A. Volodin, C. Wan, R.V. Denys, G.A. Tsirlina, B.P. Tarasov, M. Fichtner, U. Ulmer, Y. Yu, C.C. Nwakwuo, V.A. Yartys, Phase-structural transformations in a metal hydride battery anode $La_{1.5}Nd_{0.5}MgNi_9$ alloy and its electrochemical performance, Int. J. Hydrog. Energy 41 (2016) 9954–9967.

[139] C. Wan, W. Hu, R.V. Denys, C.C. Nwakwuo, J.K. Solberg, V.A. Yartys, Effect of Mg content in the $La_{3-x}Mg_xNi_9$ battery anode alloys on the structural, hydrogen storage and electrochemical properties, J. Alloy. Compd. 856 (2021) 157443.

[140] C. Wan, R.V. Denys, V.A. Yartys, Effect of yttrium content in the $La_{2-x}Y_xMgNi_9$ battery anode alloys on the structural, hydrogen storage and electrochemical properties, Dalton Trans. 51 (2022) 12986–12995.

[141] J.H.N. van Vucht, F.A. Kuijpers, H.C.a.M. Bruning, Reversible room-temperature absorption of large quantities of hydrogen by intermetallic compounds, Philips Res. Rep. 25 (1970) 133–140.

[142] A. Percheron-Guégan, J.C. Achard, J. Loriers, M. Bonnemay, G. Bronoel, J. Sarradin, L. Schlapbach, Electrode materials based on lanthanum and nickel, and electrochemical uses of such materials, in, Agence National de Valorisation de la Recherche ANVAR, 1978.

[143] F. Cuevas, J.-M. Joubert, M. Latroche, A. Percheron-Guégan, Intermetallic compounds as negative electrodes of Ni/MH batteries, Appl. Phys. A: Mater. Sci. Process. 72 (2001) 225–238.

[144] N.S. Nazer, R.V. Denys, V.A. Yartys, W.-K. Hu, M. Latroche, F. Cuevas, B.C. Hauback, P.F. Henry, L. Arnberg, In operando neutron diffraction study of $LaNdMgNi_9H_{13}$ as a metal hydride battery anode, J. Power Sources 343 (2017) 502–512.

[145] Critical Raw Materials Resilience: Charting a Path towards greater Security and Sustainability, in: Communication from the Commission to the European Parliament, the Council, the European Economic and Social Committee and the Committee of the Regions, European Commision, https://eur-lex.europa.eu/legal-content/EN/TXT/?uri=CELEX:52020DC0474, 2020.

[146] E.W. Justi, H.H. Ewe, A.W. Kalberlah, N.M. Saridakis, M.H. Schaefer, Electrocatalysis in the nickel-titanium system, Energy Convers. 10 (1970) 183–187.

[147] B. Guiose, F. Cuevas, B. Décamps, E. Leroy, A. Percheron-Guégan, Microstructural analysis of the ageing of pseudo-binary (Ti,Zr)Ni intermetallic compounds as negative electrodes of Ni-MH batteries, Electrochim. Acta 54 (2009) 2781–2789.

[148] H. Emami, F. Cuevas, Hydrogenation properties of shape memory Ti(Ni,Pd) compounds, Intermetallics 19 (2011) 876–886.

[149] H. Emami, F. Cuevas, Cobalt induced multi-plateau behavior in TiNi-based Ni-MH electrodes, Energy Stor. Mater 8 (2017) 189–193.

[150] N.S. Nazer, V.A. Yartys, T. Azib, M. Latroche, F. Cuevas, S. Forseth, P.J.S. Vie, R.V. Denys, M.H. Sørby, B.C. Hauback, L. Arnberg, P.F. Henry, In operando neutron diffraction study of a commercial graphite/(Ni, Mn, Co) oxide-based multi-component lithium ion battery, J. Power Sources 326 (2016) 93–103.

[151] N.S. Nazer, M. Strobl, A. Kaestner, P.J.S. Vie, V.A. Yartys, In operando neutron imaging study of a commercial Li-ion battery at variable charge-discharge current densities, Electrochim. Acta 427 (2022) 140793.

[152] M. Latroche, A. Percheron-Guégan, Structural and thermodynamic studies of some hydride forming RM_3-type compounds (R=lanthanide, M=transition metal), J. Alloy. Compd. 356-357 (2003) 461–468.

[153] M. Latroche, J.-M. Joubert, A.P. Guégan, O. Isnard, In situ neutron diffraction study of deuterium gas absorption by AB_{5+y} alloys used as negative electrode materials for Ni-MH batteries, Phys. B: Condens 350 (2004) E427–E430.

[154] M. Latroche, O. Isnard, In situ study of LaY_2Ni_9 compound as Ni–MH negative-electrode material, J. Phys.: Condens. Matter 20 (2008) 104243.

[155] S. Sartori, F. Cuevas, M. Latroche, Metal hydrides used as negative electrode materials for Li-ion batteries, Appl. Phys. A 122 (2016) 135.

[156] M. Latroche, D. Blanchard, F. Cuevas, A. El Kharbachi, B.C. Hauback, T.R. Jensen, P.E. de Jongh, S. Kim, N.S. Nazer, P. Ngene, Full-cell hydride-based solid-state Li batteries for energy storage, Int. J. Hydrogen Energy 44 (2019) 7875–7887.

[157] J. Monnier, J. Zhang, F. Cuevas, M. Latroche, Hydrides compounds for electrochemical applications, Curr. Opin. Electrochem. 32 (2022) 100921.

[158] J.-M. Joubert, V. Paul-Boncour, F. Cuevas, J. Zhang, M. Latroche, $LaNi_5$ related AB_5 compounds: structure, properties and applications, J. Alloy. Compd. 862 (2021) 158163.

[159] W.P. Kalisvaart, M. Latroche, F. Cuevas, P.H.L. Notten, In situ neutron diffraction study on Pd-doped $Mg_{0.65}Sc_{0.35}$ electrode material, J. Solid State Chem. 181 (2008) 1141–1148.

[160] M. Latroche, P.H.L. Notten, A. Percheron-Guégan, In situ neutron diffraction study of solid gas desorption of non-stoichiometric AB_5 type hydrides, J. Alloy. Compd., 253- 254 (1997) 295–297.

[161] M. Latroche, V. Paul-Boncour, A. Percheron-Guégan, F. Bourée-Vigneron, Temperature dependence study of $YMn_2D_{4.5}$ by means of neutron powder diffraction, J. Alloy. Compd. 274 (1998) 59–64.

[162] C. Zlotea, F. Cuevas, V. Paul-Boncour, E. Leroy, P. Dibandjo, R. Gadiou, C. Vix-Guterl, M. Latroche, Size-dependent hydrogen sorption in ultrasmall Pd clusters embedded in a mesoporous carbon template, J. Am. Chem. Soc. 132 (2010) 7720–7729.

[163] M. Hirscher, V.A. Yartys, M. Baricco, J. Bellosta von Colbe, D. Blanchard, R.C. Bowman, D.P. Broom, C.E. Buckley, F. Chang, P. Chen, Y.W. Cho, J.-C. Crivello, F. Cuevas, W.I.F. David, P.E. de Jongh, R.V. Denys, M. Dornheim, M. Felderhoff, Y. Filinchuk, G.E. Froudakis, D.M. Grant, E.M. Gray, B.C. Hauback, T. He, T.D. Humphries, T.R. Jensen, S. Kim, Y. Kojima, M. Latroche, H.-W. Li, M.V. Lototskyy, J.W. Makepeace, K.T. Møller, L. Naheed, P. Ngene, D. Noréus, M.M. Nygård, M. S.-i. Orimo, L. Paskevicius, D.B. Pasquini, M. Ravnsbæk, T.J. Veronica Sofianos, T. Udovic, G.S. Vegge, C.J. Walker, C. Webb, C. Weidenthaler, Zlotea, Materials for hydrogen-based energy storage – past, recent progress and future outlook, J. Alloy. Compd. 827 (2020) 153548.